Master's Thesis

The Common Vole (*Microtus arvalis*): A Possible New Model Organism for Growth Hormone Neuroendocrinological and Neuroanatomical Studies

Sean Goldfarb
Department of Anatomy and Cell Biology
Research conducted at the Montreal Neurological Institute (The Neuro)
McGill University, Montreal
July 2023

A thesis submitted to McGill University in partial fulfillment of the requirements of the degree of Master of Science in Cell Biology

Supervised by Thomas Stroh, Ph.D.

“You will find in the lower animals mechanisms and adaptations of exquisite beauty and the most surprising character”

Dr. August Krogh, 1929.

Dedicated to my mother, brother, late father – Janice Goldfarb, Joshua Goldfarb, Usher Joffre Goldfarb – to all researchers in pursuit of exquisite beauty, and as a memorial for those who will live through the next pandemic

Abstract

Growth hormone (GH) is a neuropeptide produced by the anterior pituitary gland, just ventral to the hypothalamus, that has effects throughout the body, but most notably on growth of the organism. The hypothalamus produces growth hormone-releasing hormone (GHRH), specifically in the arcuate nucleus (ARC), and somatostatin (SOM) in the anterior periventricular nucleus, to stimulate and inhibit, respectively, GH secretion in the anterior pituitary gland. GH is released in a pulsatile manner, with peaks (high hormone levels) and troughs (low hormone levels) throughout the day in mice. To better understand the mechanisms governing this pulsatile release, previous studies in our lab focused on comparing the numbers of synaptic inputs onto GHRH-positive neurons in the ARC during varying levels of GH secretion. This required acquisition of mouse brain tissue that consistently corresponded to either a peak or a trough in GH secretion; since the hormonal status in such experiments is not known before obtaining the brain tissue, this proved to be difficult as the hormone status could not be accurately predicted due to its asynchronous release between animals. As such, to obtain meaningful data, large numbers of mice and a lot of labour were required. Here, I propose the Common Vole (*Microtus arvalis*) as a potentially better model organism for the study of GH release patterns, with the hope of reducing the required labour and the number of animals needed for a statistically sound study, in line with the "3 Rs" principle in animal experimentation: Replacement, Reduction, and Refinement. Common voles live in communities and interestingly, to avoid predators and to mate, they are well synchronised behaviourally and endocrinologically. However, voles have not been used for such a study thus far. Therefore, we focused on breaking new ground by verifying that they are indeed suitable for our research purposes. Firstly, because the primary antibodies we currently use are known to be reactive against mouse and rats without corresponding data for the vole, we tested various primary antibodies in vole tissue. Secondly, we chose to characterise the vole in relation to mouse in terms of its brain volume, ARC volume, and ARC GHRH and SOM receptor subtype 2 (sst2) cell number, using unbiased stereology. Finally, we and our collaborators aimed to confirm that the individuals in a colony of common voles are indeed more endocrinologically synchronised than mice using a tail-clip blood collection and sandwich ELISA hormone detection method (this data is not shown). Despite some differences, we found promise in the use of *Microtus arvalis*: our antibodies that work in mouse tissue were also efficacious in vole tissue; the volume of the ARC was not significantly different between vole and mouse ($0.21 \pm 0.03 mm^3$ and $0.22 \pm 0.01 mm^3$,

respectively); vole total brain weight was significantly less than that of mouse (0.25 ± 0.01g, and 0.29 ± 0.01g, respectively); voles had significantly lower average sst2-positive cell counts per counting frame than mouse (1.80 ± 0.23 cells and 2.60 ± 0.29 cells, respectively); and the voles showed indications of higher GH-plasma and rest-activity synchronicity than mice. Regrettably, we obtained inconclusive data regarding the sst2-positive cell stereological estimation, and we encountered issues with the GHRH immunofluorescence staining. Moreover, further work – such as establishment of transgenic, knockdown, and knockout strains – would be essential to more confidently place voles on the new-animal-model map, specifically where synchronous group studies are required in the fields of neuroendocrinology and neuroanatomy.

Résumé

L'hormone de croissance (GH) est un neuropeptide produit par la glande pituitaire antérieure (GPA), sous l'hypothalamus, et a des effets autour du corps, notamment sur la croissance de l'organisme. L'hypothalamus libère l'hormone de libération de GH (GHRH) dans le noyau arqué (ARC) pour stimuler la libération de GH de la GPA, et la somatostatine (SOM) dans le noyau périventriculaire antérieur pour l'inhiber. La libération du GH est pulsatile avec des pics et creux (niveaux d'hormone hauts et bas) durant la journée chez les souris. Pour mieux comprendre les mécanismes qui gouvernent cette libération pulsatile, nos études antérieures ont comparé le nombre des entrées synaptiques sur les neurones exprimant GHRH dans l'ARC pendant des niveaux de sécrétions GH variables; ceci a requis du tissu de cerveau de souris correspondant à soit un pic, soit un creux de sécrétion GH. Cependant, n'étant pas connu en avance, il était difficile de prédire le statut hormonal avec certitude à cause de la libération asynchrone de GH entre animaux et jours. Alors, pour obtenir des données significatives, nous avons eu besoin de beaucoup de souris et de travail. Je propose le campagnol commun (*Microtus arvalis*) comme meilleur modèle animal potentiel dans l'étude des modèles de la libération de GH, dans l'espoir de réduire le travail et les animaux requis pour une étude statistiquement solide, en accord avec le principe « 3R » en recherche animale : remplacement, réduction, et raffinement. Les campagnols vivent en communauté et pour éviter leurs prédateurs et pour s'accoupler, ils sont synchronisés dans leurs comportement et système endocrinologique. Or, ils n'ont jamais été utilisés pour une telle étude. Par la suite, nous nous sommes concentrés sur ouvrir une nouvelle voie en vérifiant qu'ils sont en fait convenables pour nos buts de recherches. En premier, les anticorps primaires que nous utilisons à date dans notre laboratoire sont connu à réagir contre les souris et rats, donc, sans données correspondants en campagnol, nous avons testé les anticorps primaires variés en tissu de campagnol. Deuxièmement, nous avons choisi de caractériser le cerveau campagnol – en fonction de son volume cervical et d'ARC et son nombre de cellules exprimant GHRH et récepteur de SOM sous-type 2 (sst2) – en relation à la souris, en utilisant la stéréologie non-biaisée. Finalement, nous et nos collaborateurs avons visé à confirmer que les individus dans une colonie de campagnols sont en fait plus synchronisés endocrinologiquement que la souris en utilisant une méthode de collection de sang clip-de-queue et de la détection d'hormone sandwich-ELISA (données non présentées). Malgré quelques différences, nous voyons des promesses en l'utilisation

de *M. arvalis* : les anticorps qui fonctionnent dans les souris ont fonctionné également avec les campagnols; le volume de l'ARC n'a pas été significativement différé entre souris et campagnol ($0.21 \pm 0.03 mm^3$ et $0.22 \pm 0.01 mm^3$, respectivement); le poids total du cerveau campagnol a été significativement moins de ce du souris (0.25 ± 0.01g et 0.29 ± 0.01g, respectivement); le campagnol a eu un compte moyen de cellules positif en sst2 par cadre de comptage significativement moins que la souris (1.80 ± 0.23 cellules et 2.60 ± 0.29 cellules, respectivement); et les campagnols ont montré des indications d'une meilleure synchronicité de GH plasmique et d'activité-repos que les souris. Malheureusement, nous avons collecté des données peu concluantes concernant l'estimation stéréologique des cellules positives pour sst2, et nous avons rencontré des problèmes avec la coloration immunofluorescente de GHRH. Par ailleurs, la poursuite des travaux – par exemple l'établissement des souches transgéniques, knockdown et knockout – serait essentiel pour mettre les campagnols sur le mappe de modèle animal utile, spécifiquement où les études de groupe synchronisé sont nécessaires en le domaine de la neuroendocrinologie et la neuroanatomie.

Acknowledgements

I would like to thank Dr. Thomas Stroh for your unwavering encouragement and support over the course of this long and many-times delayed project. For your guidance in putting my best foot forward when discussing research. For sharing all your microscopic and anatomical knowledge, and of course, for all the fascinating conversations we had outside the scope of this degree.

To my friend, fellow scientist, and comrade-in-arms, Klaudia Bednarz, for your invaluable support in helping me carry out my research, learn to think and express myself as a scientist, and your company on our many bull sessions. I hope I can count you as a close friend in the years to come. *Dziękuję ci bardzo, moja przyjaciółko*!

To the plucky undergraduate student, Sarah Beydoun, for your tenacity in carrying out the cell counting on my behalf with the StereoInvestigator program. Good luck in your future studies!

I would like to extend greatest thanks to our collaborators in the Storch Lab – Dr. Kai-Florian Storch and Pratap Singh Markam – for your willingness to perform the ELISA experiments on our behalf during the height of the pandemic. And again, for later letting us move the *Microtus arvalis* colony to the Neuro. And of course, to Pratap for always being willing to answer my questions.

I would like to thank Dr. Fernando Chaurand for your kindness in setting aside your time to help me euthanise the animals. What interesting conversations we had: what happens in the perfusion room, stays in the perfusion room! And of course, thanks to all the people in the animal facility.

To Dan Peruzzi for your patience and kindness in assisting us with the use of the StereoInvestigator program and answering any theoretical questions with such dexterity. Without you, the better part of this project would have not been possible.

To the Petrides Lab, specifically Sarah Lefebvre and Dr. Kep Kee Loh, for lending us your microtome, time, histology expertise and for sharing your stock of Cresyl Violet. Of course, also for your friendship and the many lunchtime conversations over the years.

To everyone in the Peyrache lab, for your assorted help: lending of PBS tablets, your ddH_2O tap, your desk lamp, your magnifying glass for tissue selection; and of course, for your camaraderie.

Thanks to my advisory committee, Dr. Jean-François Cloutier, Dr. Maia Kokoeva, and Dr. Nathalie Lamarche-Vane for your interest in my project and invaluable advice during my degree.

I would like to also extend my thanks to Joelle Denomy, Penny Kaill-Vinish, and Naomi Takeda for all your patience in answering all my many questions regarding, and helping me with, the administrative aspects of this degree and in my preparation for my next degree. You're the best!

Thanks to my mother (Janice Goldfarb), brother (Joshua Goldfarb), late father (Usher Joffre Goldfarb), Joan O'Malley, Dr. Walaa Alshafie, the Pack Lab and all my friends for your moral support throughout my life and this very long degree.

I would be remiss in not thanking the mice and voles for their sacrifice in the name of this project, and of course to Covid-19 for teaching me the meaning of persistence, adaptability, how to bounce back from setbacks, and for showing me the importance of friendship, comity, and camaraderie.

Finally, thanks to Dr. Pablo Henny Vargas for examining the initial thesis.

Contribution of Authors

I performed all vole brain freezing and all sectioning, processing, staining, confocal and widefield imaging, Cavalieri stereology, and data analysis on vole and mouse brains.

Dr. Thomas Stroh and Pratap Singh Markam conducted initial vole, and Klaudia Bednarz initial mouse, perfusions, and brain extractions. Klaudia froze the initial mouse brains. Later mice and later voles were perfused by Dr. Fernando Chaurand and their brains extracted and frozen by me. Sarah Beydoun counted the sst2+ cells using the optical fractionator stereology workflow.

Pratap Singh Markam conducted the vole habituation, sandwich ELISA experiments, and plotted the data related to that (not shown) and gave us permission to discuss said data in this thesis. With the help of Dr. Thomas Stroh and Klaudia Bednarz, I designed all other experiments. I performed all statistical analysis, with some help from Klaudia Bednarz, and created all graphs and figures. Laurent Garcia and Élise le Guillou helped me with the French translation of the abstract.

I wrote the thesis and Dr. Thomas Stroh and Klaudia Bednarz reviewed the initial version.

List of Tables, Figures and Appendices

Table of Contents

1. INTRODUCTION

1.1 Growth Hormone and Somatostatin

Growth hormone (GH) is a neurohormone that is involved in a multitude of functions throughout the body. It is involved in protein, glucose, and fat metabolism; bone and muscle development; and, perhaps most explicitly, growth [1,2]. With so many functions, there are also several dysfunctions associated with GH. Such disorders include gigantism (child-onset excess GH), acromegaly (adult-onset excess GH), dwarfism (child-onset GH insufficiency), growth hormone deficiency syndrome (adult-onset GH insufficiency), Laron syndrome (GH insensitivity), and many others [1,2,3,4,5]. GH is even implicated in insulin resistance and diabetes [1,6]. With such a wide net of functions and dysfunctions, there is naturally a motivation to further understand growth hormone physiology and pathophysiology, as well as to elucidate pharmacological and other strategies to correct and maintain GH homeostasis.

GH is a polypeptide containing 191 amino acids, produced by pituicytes in the two lateralmost wings of the anterior pituitary gland, at the ventral part of the brain, immediately below the hypothalamus [1,7]. GH has a half-life of approximately 10-20 minutes in plasma and travels from the pituicytes via the bloodstream to various downstream effectors such as the liver, bone, and muscle [1,8,9]. When the liver is stimulated by GH it releases insulin-like growth factor-I (IGF-I), a molecule which is related to insulin and has similar effects on the body; though the liver produces 75% of the body's IGF-1, many tissues also locally produce it [1,5,6]. GH can act either directly on downstream targets or indirectly through IGF-I [1,5]. Moreover, IGF-1 has been found to independently effect organismal growth, alone and in concert with GH [1,5]. Furthermore, GH (and IGF-I) promote glucose and lipid metabolism [1,7]. Though excess IGF-I production can result in diabetes, the effect of GH on insulin-resistance is markedly less important [1]. GH and IGF-I promote muscle growth by retaining amino acids in muscle from the bloodstream while encouraging protein production and discouraging proteolysis [1,7]. These are just to name a few of GH's functions. Overall, GH acts to encourage growth via chondrocyte stimulation, increased protein production, and it encourages lipid breakdown and the breakdown of glycogen [1,7].

Somatostatin (SOM) is a polypeptide that has a half-life of 2 minutes and comes in two main forms: SOM-28, which is 28-amino acids long, and SOM-14, which is 14-amino acids long and makes up part of SOM-28 [10]. SOM is produced throughout the central nervous system, the peripheral nervous system, as well as many organ systems, such as the small intestine, placenta, and kidneys [10]. It acts as a classical hormone, a neurotransmitter-neuromodulator, and, especially in the gut, locally as a paracrine-autocrine regulator [10]. Despite this plurality of actions, it generally has an inhibitory effect, notably on GH rhythmic secretion [10]. There are five SOM receptors, dubbed sst1, sst2, sst3, sst4 and sst5, each with specific localisation across the brain and body [10]. Sst2 is perhaps the most widely distributed of the SOM receptors; in the arcuate nucleus (ARC), the most common receptors are sst1 and sst2 [10,11,12]. As a result of being produced, and having so many receptors (particularly sst2), in so many locations, SOM has a wide variety of functions (growth, cognition, learning, memory and metabolism) [10,11,12].

GH production is regulated through the interactions between the hypothalamus and the anterior pituitary gland [1,10]. In the hypothalamus, or more precisely the ARC, GH-releasing hormone (GHRH) is produced by the GHRH-positive parvocellular endocrine-neurons and released into the hypophyseal portal blood system at the median eminence (a bump at the base of the ARC which attaches to the pituitary gland via the pituitary stalk) [1,10]. There it travels to the anterior pituitary gland to stimulate production and release of GH by the pituitary somatotrophs into the systemic blood [1,10]. Following stimulation by GH, the various organ systems feed back to the ARC and pituitary gland and stimulate the release of SOM which inhibits the release of GHRH and GH, in a rhythmic fashion [1,10]. Furthermore, GHRH autoregulates itself, and it is worth noting that GH's main downstream effector, IGF-1, also plays an important inhibitory role by stimulating SOM release as well as by directly inhibiting GHRH [1,10]. Moreover, adrenocorticotropic hormone (ACTH) release is known to be inversely related to GH release [8]. That is, when an animal is in stress, ACTH secretion is increased, decreasing GH secretion [8]. Similarly, a compound produced by the stomach in response to hunger, ghrelin, is also implicated in controlling GH release [13]. Specifically, ghrelin directly targets and stimulates GHRH neurons in the ARC [13].

GH, like many other hypophyseal hormones, is released under an ultradian rhythm (a rhythm which occurs many times within a day, such as a heartbeat): in male rats, this rhythm has

a period of 3h, while female rats have peaks of GH release roughly every hour [14,15]; in male mice it has a period of 2h, and female mice, like female rats, have more frequent and more continuous GH release of about every 1h [16]; and similar to the rodents, in humans, men have a large release of GH at night with very small peaks the rest of the day and women have more uniform pulses of release over the course of 24 hours [9]. This pulsatility is generated by the interplay between SOM and GHRH, and in an indirect way, ghrelin and IGF-1 [10,13,14]. Furthermore, it has been shown repeatedly that the hypothalamus undergoes rhythmic changes alongside these cyclic hormonal rhythms [10,17,18]. Specifically, our lab and others have shown that there are changes in the number and density of synaptic connections on hypothalamic neurons and these may in fact cause changes in synaptic transmission leading to the hormone rhythms we see; though up until recently, aside from some studies done in the magnocellular oxytocinergic system implicating astrocytic involvement, the mechanisms that might underlie such a process were totally unknown [18,19,20,21]. In our lab, we recently sought to test the hypothesis that there would be more inhibitory synapses during low-levels (troughs) of GH release, identifiable via the presence of VGAT (presynaptically) and Gephyrin (postsynaptically); and more excitatory synapses during high-levels (peaks) of GH release, identifiable via the presence of VGLUT2 (presynaptically) and PSD-95 (postsynaptically) [22,23]. Using direct stochastic optical reconstruction microscopy (dSTORM) we identified synapses by immunolabelling tissue against VGAT, Gephyrin, VGLUT2 and PSD-95, and defined them as synapses when clusters of labelling were close to one another. We found that during troughs, 66% of all synapses were inhibitory and 34% were excitatory; during peaks, 29% of all synapses were inhibitory and 71% were excitatory. Interestingly, 40% of non-synaptic clusters also appear to have formed excitatory synapses during peaks [22,23]. Furthermore, using focused ion beam scanning electron microscopy (FIB-SEM), we found some evidence that astrocytic processes were involved, confirming the work of Theodosis et al., though this was less conclusive [19,20,21,22].

However, over the course of our previous study, there were some challenges. In order to compare synapse numbers between peak and trough hormone release, we needed to euthanise the animal at the right time in its hormonal cycle, without knowing the hormone concentrations at the time of euthanasia. While troughs can last several hours, the peak period (from onset to the end of the peak curve) lasts no more than one hour, with the peak proper lasting about 20 minutes, leaving little space for error in accurately predicting its timing. To gain some insight into the timing of the

peak and trough, we profiled the plasma GH over the course of a day in each animal. The following day, we euthanised the animal at the same time as the observed peak from the previous day with the expectation that the peak would occur at the same time. However, plasma GH level measurements taken the day the animals were euthanised were rarely consistent between days in a given individual, nor did the mice have GH release synchronicity between each other. This made obtaining tissue during the peak very challenging. We were required to euthanise many mice, without certainty of the outcome. Moreover, considering that the animals also needed to undergo procedural habituation for weeks to minimise stress (and thus minimise the possible confounding variable of stress hormone abolishing or attenuating the GH cycle), the success rate of such a study becomes limited. Though our lab obtained everything it needed to continue the study, the amount of time and animals needed to obtain these results could potentially be optimised with the use of the common vole, *Microtus arvalis*, instead.

1.2 *Microtus arvalis*; or, the Common Vole

August Krogh, sometimes called "the father of modern physiology", wrote a famous essay in 1929 on the state and future of physiology, prescient about the interdisciplinary path the field ultimately took. In this paper, he is particularly lauded for formulating "Krogh's Principle", which states that "for a large number of problems there will be some animal of choice, or a few such animals, on which it can be most conveniently studied" [24]. Indeed, lately there has been more and more interest in expanding the repertoire of animal models and moving away from the "big 6" (*Escherichia coli* bacteria, *Saccharomyces cerevisiae* and *Schizosaccharomyces pombe* yeasts, *Caenorhabditis elegans* nematodes, *Drosophila melanogaster* flies, and *Mus musculus* mice), which were chosen merely because they are the most conveniently accessible animals [25]. Yet, there is controversy about how best to apply the Krogh principle, since as Green says, "organisms picked out using the Krogh principle may be 'special cases' rather than ideal models", though at the same time, she says this is their particular strength as they are thus "well-suited for identifying and studying a specific mechanism or physiological problem" [26]. Indeed, Green also says "Krogh organisms" are not selected for their similarity to other animals or representational scope, but rather because their unique anatomical/physiological features make them experimentally accessible; this makes them not model organisms in and of themselves but instead they may serve a highly complimentary role to model organisms [26]. All to say, though fraught with some

controversy, it is undeniable that there is some appeal to using more than the "big 6" for research in the life sciences [25].

In light of this, the genus of *Microtus* in particular is facing much interest, being a rodent genus with one of the largest radiating phylogenetic trees, consisting of at least 44 to as many as 70 members [27,28,29,30]. Many species of *Microtus* are currently used in a rather wide variety of interesting specialised research, for example: *Microtus agrestis* (Short-tailed field vole) and *Microtus californicus* (California vole) have been used for more general research, especially in phylogenetic and population dynamics studies [29,31,32]; *Microtus pennsylvanicus* (Meadow vole) is used in nutrition and toxicity studies as well as being used as a model for epileptic seizures due to their tendency, in certain handling and environmental conditions, to develop tonic-clonic seizures following periods of head-shaking and stilted gait [29,33]; most famously perhaps, *Microtus ochrogaster* (Prairie vole) is used as a model in researching courtship, pair-bonding and territoriality mediated through oxytocin and vasopressin – note that *M. pennsylvanicus* is frequently used in contrast to *M. ochrogaster* in such studies [29,34,35]; *Microtus montanus* (Mountain vole) is used as a model to study African trypanosomiasis, as well as having some sensitivity to 6-methoenzoxazolinone [29,36]; *Microtus oeconomus* (Tundra vole) has been used as a model to study cholesterol's effects in atherogenic diets [29,37]; and finally, *Microtus arvalis* (Common vole) has been used as an herbivorous model to study diabetes, (microbiotic) nutrition, and sex chromosome abnormalities [29,38,39,40,41].

Most voles are endemic to North America, but *Microtus arvalis* inhabits the grasslands of (particularly Western) Europe, ranging from the coasts of France and northern Spain to as far east as Mongolia and as far north as the southern tip of Finland [29,42,43]. This species of vole is particularly prone to overpopulation (also called rodent plagues) causing much damage to the agriculture industry, especially that of alfalfa, with records going as far back as the Middle Ages [28,44,45]. Indeed, *M. arvalis* has been a topic of scientific agricultural study from as early as 1949, by the German Plant Protection Service (*Deutschen Pflanzenschutzdienstes*), to as recently as 2021 [44,45]. *M. arvalis* has been studied extensively to understand its population dynamics, behaviour, and reproductive states for the purposes of better controlling this noxious pest [44,45,46,47]. Up until about 1975, studies looking at any rhythmicity of *M. arvalis* were focused mainly on seasonal rhythmicity of hormone levels (LH and GH), as noted above. By the 1980's,

researchers began investigating the common vole's activity patterns and by the 1990's, and ever since, earnest work on the common vole's biological rhythms has been carried out (see below). Over this time, many interesting peculiarities about *M. arvalis*' rhythms have been elucidated.

Adult common voles are mainly active during the day and are synchronised to the group, with bursts of feeding activity about every two hours: i.e., they all leave their burrows as a population to feed [48]. This rhythm is mainly dictated by their feeding and predation patterns, though territoriality and exploration are also involved in this rhythm [48,49]. It was initially believed that this two-hour-periodic synchronicity was to facilitate microbial digestion, but an elegant paper by Gerkema and Verhulst showed that when a group of voles are feeding in proximity (some in one enclosure and others in an adjacent walled-off one), those that spot a kestrel (their main predator) will react by either freezing or fleeing, and the other voles that cannot see the kestrel will copy their reaction, even when they cannot see one another [50]. In so doing, they demonstrate that they warn each other of the presence of danger as well as how to react to it, likely auditorily (ultrasound), providing an explanation of the advantage to being synchronised; namely: while feeding in the field, they can warn each other of lurking predators, and, in the burrow, they can huddle to save energy especially when it gets cold [50].

Looking at these rhythms in more detail, researchers discovered that after 30 days in total darkness, though ultradian feeding remained in all intact common voles, circadian rhythms in intact voles completely broke down [51]. Circadian rhythms are biological rhythms that last about 24 hours, like the sleep-wake cycle in humans or the nocturnal nipping habits of *Chippendale mupp*, both of which have a sleeping period of eight hours [52]. This means that ultradian rhythms in voles are somehow separated from their circadian rhythms. In fact, lesion studies showed that the suprachiasmatic nucleus (SCN) is the circadian pacemaker, while the retrochiasmatic and arcuate nuclei are required for the ultradian rhythm [51]. Moreover, this feeding rhythmicity is connected to an independent clock system and is not dependent on the voles' rest-activity or on any hunger or thirst regulation; indeed, when deprived of food and water, the voles will attempt to feed as often and at the same times as during *ad-libitum* food access [53]. This independent clock system makes each vole's ultradian feeding rhythm synchronised to the community's and it is composed of a light-sensitive ultradian oscillator; this oscillator's rhythm is reset at dawn, not directly by light but by the end of the activity phase which is, however, controlled by the circadian

pacemaker [54], i.e., the SCN, which is itself controlled by the external effect of light [55]. In other words, the voles' circadian rhythm largely exists, not to generate the rhythm, but rather to adjust the timing of the ultradian rhythm to keep the voles synchronised [51,53,54,55]. However, the mechanisms and substrates of this ultradian oscillator have been a topic of debate. Yet when dopamine transporter is removed from mice, the ultradian period of their activity cycles is lengthened from 2-4 hours to about 12 hours [56,57]. Furthermore, Bmal1$^{-/-}$ mice kept in constant darkness (DD) show a synchronisation between extracellular dopamine levels and their ultradian locomotor activity period [56,57]. Moreover, it was found that methamphetamine administration in mice created a circadian clock in addition to the SCN, and that ablation of the SCN did not significantly affect the rhythmicity of this meth-induced oscillator [56,58]. When these meth-treated, SCN-ablated mice were administered haloperidol (an antipsychotic which binds to dopamine receptor 2), the rhythm phase was shifted according to when haloperidol was administered [56,59]. This suggests that there is involvement of dopamine in the functioning of the ultradian oscillator. Moreover, dopamine neurons exist in the ARC, which, as previously described, is involved in ultradian rhythmicity [56]. This seeming central role of dopamine in ultradian oscillator generation prompted researchers to coin it the Dopaminergic Ultradian Oscillator (DUO) [56,57]. Studies on *M. arvalis* in DD show that their ultradian rhythms are locked to the circadian clock, which would suggest the two are coupled [54,56]. This is confirmation of the above, where the ultradian oscillator is reset at dawn thanks to the SCN. At any rate, our collaborators at the Storch Lab at the Douglas Research Centre (Montreal, Quebec) were interested in using the voles to study adrenocorticotropic hormone which is strongly influenced by the SCN-DUO circadian timer. As such, we postulated that since the SCN-DUO circadian timer also heavily influences GH, *M. arvalis* could thus be used in the context of ultradian secretion of GH [60]. We chose to test this by: 1) measuring their rest-activity periods via actograms (graphical representations of rest and activity behaviours used in circadian research to extract information about an organism's biological rhythms over the course of a day or during light and dark periods) through which we can confirm that the voles in our colony are synchronised because their rest-activity cycles are independent to the circadian clock, i.e., are linked to the ultradian clock; and 2) measure their GH plasma levels to verify that they are also synchronised at the level of their GH hormone secretion. Indeed, Vadász published a communication on GH in the common vole in 1974 where he found seasonal and sexually dimorphic differences, which is a minor precedent of

the animal's use in the study of GH [46]. Furthermore, given *M. arvalis*' usefulness in studying insulin and diabetes, and given GH's implication in both, it would not be unreasonable to suggest that *M. arvalis* might have practical use in this field too [6,7,38,39,40].

1.3 Antigen Selection for Immunofluorescence Staining

Over the course of the present project, we targeted several proteins and peptides with immunofluorescence staining. These were the same antigens targeted over the course of our lab's past studies, which we were hoping to target in vole tissue in this and future studies as well. [18,22,23]. At the outset of this project, we were uncertain whether these antigens in vole tissue would bind the antibodies that are raised and verified to only react with rat and mouse. Therefore, we chose to first test them in vole tissue. Given that *Microtus* and *Mus* are in the same superfamily (*Muroidea*), as well as the fact that many of our selected antigens are crucial proteins unlikely to differ from species to species, we hypothesised that the mouse/rat-reactive antibody would bind the vole antigen [30].

Since proteins involved in synaptic plasticity and synaptic transmission (synaptic proteins) are typically concentrated near neuronal synapses, immunofluorescent staining of such proteins tends to produce dots, or "punctae", which are known to represent clusters of the synaptic protein targeted by the antibody, and thus may be taken as a proxy for a potential presynaptic or postsynaptic membrane [61,62]. Though when found alone these markers do not reliably indicate a synapse, when a presynaptic punctum and a postsynaptic punctum are found overlapping, together they may be taken as a potential synapse [63]. All but two of the antigens we tested (GHRH and sst2) are synaptic proteins, and thus found across the brain:

GHRH is produced by parvocellular neurons in the ARC. However, like all parvocellular neuropeptides, it does not stay long in the cell body. It is rapidly transported to the axonal compartment (i.e., there is high flux of the hormone), making it difficult to strongly visualise the hormone in the cell body, unless the antibody is very sensitive. One way to overcome this quick exit of the antigen is to inject the animals with colchicine, which has the effect of capping microtubules, thereby preventing cellular trafficking, causing a backup of GHRH in the cell body, and allowing us to visualise the cell body [64]. However, the strong systemic toxicity of the drug poses a challenge when studying natural hormonal cycles, where a multitude of processes happen to maintain the natural hormonal rhythm. As such, we had to conduct immunofluorescent staining

of GHRH cells without the use of colchicine. In sum, antibodies targeting it will produce a strong stain of the cytoplasm of cells in the ARC.

Sst2, as mentioned previously, is a receptor on the entire cell membrane (including axons and dendrites) of many cell types across the brain that respond to somatostatin; it is also the more prevalent of the five somatostatin receptors in the brain [10,11,12]. A small population is found in the ARC with a larger population in the anterior periventricular nucleus, immediately adjacent to the ARC [10,11,12]. Due to its location on the cell, the corresponding antibody will produce the most staining on the membrane of the cell body, axons and dendrites. This antibody is very effective because it targets a receptor found outside the cell, which means that only partial cell-permeabilisation is required, and unlike a hormone, it is not excreted, so its presence is more stable.

Vesicular GABA Transporter (VGAT) *i*s a presynaptic protein indicative of inhibitory synapses and is used as a marker for such. It is a protein found on presynaptic vesicles and acts as an antiporter exchanging vesicular protons for GABA and glycine into these vesicles for later release into the synaptic cleft [65]. Such vesicles may be found fusing at the presynaptic membrane or docked in a pool near a (potential) presynaptic membrane, as such the corresponding labelling shows up as punctae scattered throughout the tissue, and because there are also many synaptic connections to cell bodies, we expect to see many punctae associated with cell bodies. For this reason, this antigen is often used to delineate neurons that receive strong inhibitory inputs.

Gephyrin is a postsynaptic protein associated with microtubules and is indicative of and used as a marker for inhibitory synapses. It anchors inhibitory neurotransmitter receptors, like GABA type A and glycine receptors, to tubulin dimers on subsynaptic microtubules [66,67]. Given its anchoring role for the postsynapse, with this labelling we expect to see many punctae all over the tissue, representing dendritic and cell body membranes.

Vesicular Glutamate Transporter 2 (VGLUT2) is a presynaptic protein, and it is indicative of and used as a marker for excitatory synapses. It is found on presynaptic vesicles and acts as a uniporter for glutamate, allowing it into vesicles for later release into the synaptic cleft, as well as acting as a channel for ions like chloride, potassium, sodium, and phosphate [68]. These vesicular proteins may be found fusing at the presynaptic membrane or docked in a pool near a (potential) presynaptic membrane. As such, the corresponding labelling shows up as punctae scattered throughout the tissue, and because there are also many synaptic connections to cell bodies, we

expect to see many punctae associated with cell bodies. For this reason, this antigen is often used to delineate neurons that receive strong excitatory inputs.

Post-Synaptic Density-95 (PSD-95) is a postsynaptic scaffolding protein, indicative of and used a marker for excitatory synapses. It associates with PSD-93 to be recruited into glutamate-receptor and potassium-channel clusters, as well as to form a scaffold for receptor clustering, ion channels and signalling proteins; it is also implicated in synaptogenesis and synaptic plasticity [69,70]. As it is a scaffolding protein for the postsynapse, with the corresponding immunofluorescent stain, we expect to see many punctae all over the tissue, representing dendritic and cell body membranes, and it may sometimes visualise cells.

Shank2 is a postsynaptic synaptic-density adaptor-protein, indicative of and used as a marker for excitatory synapses. It is believed to be an adaptor protein that interconnects receptors of the postsynaptic membrane (including glutamate receptors) and the actin cytoskeleton; it may also be involved in organising the synaptic junction and dendritic spines [71]. Given its role in the dendritic spine and in the postsynapse, we expect to see punctae all over the tissue.

NeuN is a protein found only in the nucleus of neuronal cells, so it is not found in glial or cardiovascular cells. It is involved in the regulation of alternative splicing of pre-mRNA of those mRNAs destined for nonsense-mediated decay [72]. NeuN is often used as a marker for postmitotic neurons, and though it is not as widely used as DAPI (which stains all cells' nuclei), it can be used as a more informative alternative since it visualises neuronal nuclei specifically [73].

Piccolo and ***Bassoon*** are both presynaptic scaffolding proteins. These proteins act closely together and have many roles at the presynaptic cytomatrix of the active zone as scaffolding proteins: following synthesis, they form at the Golgi apparatus, and from there they travel together in Piccolo-Bassoon transport vesicles (PTVs) to nascent synapses; they regulate the organisation of presynaptic vesicles (piccolo specifically earmarks some as a reserve so that not all are released in response to a single action potential), as well as protein complexes involved in membrane fusion and compulsory endocytosis at the presynaptic membrane; they are also implicated in synapse-to-nucleus communication and the regulation of presynaptic protein ubiquitination [74,75]. Given this wide variety of roles for both piccolo and bassoon, with immunofluorescent staining, we expect to see punctae all over the tissue, though due to their localisation in PVTs at the Golgi, it would not be a surprise to see labelling of cell bodies as well.

Homer1 is a postsynaptic scaffolding protein, indicative of and a marker for excitatory synapses. It binds and cross-links many other proteins including glutamate and inositol receptors, different ion channels, adaptor proteins, and scaffold proteins; it regulates the trafficking and surface expression of glutamate receptors and may be involved in structural synaptic changes which occur during neuronal plasticity and development; and as part of a high-order complex, it is necessary for the function and structure of dendritic spines [76]. With so many roles, particularly its implication at the dendritic spine, we expect immunofluorescent staining to label punctae all over the tissue.

1.4 Design-Based Stereology

For this study we decided to count the number of GHRH and sst2-expressing cells in the ARC, as done in our lab before, and measure the volume of the ARC in the vole, as compared to mice [18]. Since GHRH and sst2-expressing cells are greatly involved in GH rhythmicity (i.e., the up or downregulation of its plasma levels), knowledge about their cell counts and the volume of physical space they occupy becomes important, especially considering how little is known about the vole's GH endocrinology. To do this in a statistically sound way, as before, we opted to use the well-established (*design-based*) *stereology* (DBS). There are several approaches using DBS to obtain useful measurements, including but not limited to length, area, volume, and number. We were interested in number and volume measurements specifically. These utilise the Optical Fractionator and Cavalieri methods, respectively. Stereology is a discipline defined as the study of effectively obtaining 3D information from 2D data and its goal is to sample the objects-of-interest in a way that allows us to do less work than counting every point, or more precisely, "to take small parts of a whole or an entirety in such a way that conclusions drawn from observations in the sample are valid for the entirety" [77,78].

The struggle of stereology is to avoid sampling models based on assumptions in order to obtain unbiased data. Since 1925, stereologists grappled with an unsolvable riddle, called the Corpuscle Problem, which states that in a given tissue, not all arbitrarily chosen objects have the same size and shape, and, as such, some might be sampled by the sampling probe (i.e., hit by the knife blade) multiple times and others not at all [79]. This means that the number of counted objects may be unequal to the number of existing objects; and worse, since we do not know how many objects there actually are in the tissue, we cannot tell when this is the case while conducting a

given estimation [79]. For nearly 60 years, stereology's answer was in "correction factors", formulas that estimate the parameters of the tissue, and in so doing, they force biological objects to fit Euclidean geometrical models like spheres and lines [78]. However, this is problematic: for example, we may define all cells as spheres, but what about ovoid cells? Are they not cells too? Should we exclude them? Correction factors such as this introduce assumptions and biases that are difficult to justify, create a mismatch between the counted objects and the existing objects, and unfortunately do not account for the corpuscle problem anyway [78]. In 1984, however, Gundersen proposed the Disector Principle as the resolution to the Corpuscle Problem; and later in 1986, improved it, by creating the Optical Disector [77,80]. This technique makes use of Gundersen's unbiased counting rules (see Methods, section 3.5) and because of this we may obtain a reliable and accurate unbiased estimate of objects from our tissue. Briefly, this technique works by comparing two optical sections a known distance apart, and on one of these we count objects which do not appear in the other; in this way we ensure we count an object only once, while also only needing to count a subset of all objects to get an estimate of total object number in the section [78,80,81]. Another technique called the Fractionator, which estimates the total number of all objects taken from a selection of a stack of sections with an arbitrarily chosen interval, gives an estimate of objects counted across the stack [77]. Gundersen combined these two techniques to make the Optical Fractionator, allowing us to get an estimate of objects within and between sections [78]. For more treatment on the history and theory of stereology, see appendix 1.

Of the many equations used in stereology to effectively estimate object number and volume, we will go through the main ones used over the course of this study to better understand what is going on. The first is the *Optical Fractionator Estimator* seen below:

$$N = \sum \mathrm{Q}^{-} \bullet \frac{t}{h} \bullet \frac{1}{asf} \bullet \frac{1}{ssf}$$

where Q^{-} is the particles counted; t is the section mounted thickness (for more detail, see Methods, section 3.5); h is the counting frame height; asf is the Area Sampling Fraction (i.e., the counting frame/grid size); and ssf is the Section Sampling Fraction (i.e., 1/p, or the interval between sections) [82]. Though this formula is actually quite simple, it is difficult to initially parse, so I will break it down. The fraction t/h is really the reciprocal of h/t, which is more easily understood: the ratio of the counting frame height to the total section height, e.g., an h of 20 within a t of 100 would give an h/t of 0.2 and the reciprocal t/h is 20. The asf can be considered the ratio of the grid

to the counting frame, e.g., a 90x90mm frame on a 900x900mm grid square would give an asf of 90x90/900x900 or 1/100, and the reciprocal 1/asf would be 100. The ssf is the ratio of the sections used to those not used (i.e., the frequency of selected sections), e.g., every sixth section used would make the ssf 1/6 and the reciprocal 1/ssf would be 6. If the particles counted ($\sum Q^-$) is found to be 30, our calculation would be thus: N = 30 particles • 20 • 100 • 6 = 360,000 particles. In other words, the optical fractionator takes the sum of points counted and estimates how many points we should have if we were to include the non-counted sections, the non-counted height, and the non-counted area of each section. Note that the combination of disector and fractionator into the optical fractionator is illustrated thusly: "t/h • 1/asf" can be considered equivalent to "V(ref)/v(dis)" in the disector formula; and "1/ssf" equivalent to "p" in the fractionator formula [see appendix 1].

For the Cavalieri volume estimation we use the *Estimated Volume formula, $\hat{v}$*:

$$\hat{v} = A_p m' \bar{t} \left(\sum_{i=1}^{n} P_i \right)$$

where A_p is the area associated with a single point ($A_p = g^2$, where g^2 is the grid area corresponding to one point); m′ is the section evaluation interval (i.e., the frequency of selected sections); $\bar{t}$ is the mean section thickness; and P_i is the number of grid point corners counted (only one corner counted per grid square) [82]. In other words, we calculate the total volume in the region by multiplying the volume per point (area per point by height of the region) by the sum of all points counted. Note that m' and $\bar{t}$ together correspond to the total thickness of the region-of-interest.

In both cases, we conduct a pilot study, and through use of an error formula, we determine if the pilot study's sampling parameters are adequate to statistically estimate with the tissue; if they are adequate, our experiment's parameters can be defined by this pilot study. This aforementioned error formula is called the *Gundersen Coefficient of Error (CE)*. There is a variation for the Optical Fractionator Estimator (left below) and another for the Cavalieri Estimator (right below):

$$CE_{OptFrac} = \frac{\sqrt{TotalVar}}{s^2} \qquad\qquad CE_{Cavalieri} = \frac{\sqrt{TotalVar}}{\sum_{i=1}^{n} P_i}$$

where TotalVar is the Total Variance; s^2 is the variance due to noise; n is the number of sections; and P_i is the number of points counted on the grid [82]. In both cases, TotalVar is calculated by adding variance due to noise (s^2) with the variance caused by systematic random sampling (VAR_{SRS}), see formula 7 in appendix 2. VAR_{SRS} is the variance of the objects counted, calculated

between sections (as caused by our regime of systematic random sampling); see formula 8 in appendix 2. For the Optical Fractionator CE, s^2 is the variance within a single section, and it is calculated by summing all objects counted across all sections (see formula 9 in appendix 2). Note, however, that in the Cavalieri CE, the s^2 contained within the TotalVar is different (see formula 10 in appendix 2). In the Cavalieri CE, $\Sigma P_{i,}$ like s^2, represents the total sum of all counted points (in this case, the corners of counted grid squares). Putting the CE formulas into simpler terms, the CE asks if there is any variance in the counts between *and* within sections. Ideally the answer should be no, or close to no, variance. This "close-to-no" is usually defined as being 0.1. Any more and there is too much variance, and we need more sampling. Any less and we are doing too much work and can sample less, though this latter situation is acceptable from a statistical point of view. As such, if the Gundersen CE is not adequate (not $\lesssim$0.1), we need to review our pilot study's parameters to reduce the error. As seen in the two CE formulas above, we may either increase the number of sections we use or increase the number or size of counting sites or counting frames. In other words, sample more tissue to get a more statistically representative pilot study on which to base our estimate. When our sampling parameters are acceptable, we can be assured we will get a representative and accurate estimate.

2. RATIONALE AND HYPOTHESIS

In view of the above, we postulate that, voles being a species related to mice at the superfamily level [30], there will be similarities between the two species in terms of antibody reactivity, and GHRH-positive and sst2-positive cell counts. However, voles might be better-suited than mice to questions that would benefit from using a model organism displaying hormone synchronicity between animals and between days. Since *M. arvalis* has not yet been investigated as a model system for the study of GH, this study is an exploration of the similarities and differences between the mouse and the vole apropos some of the metrics used in neuroendocrinology and neuroanatomy, particularly in our lab. Through this, in the context of ultradian hormone studies, we hope to improve "The three Rs" of animal research: Replacement, Reduction and Refinement. We hypothesise that *M. arvalis* 1) will be recognised by the commercially available antibodies already established by our lab in mouse, which we hope to use in vole in future studies similar to those we have already done in mouse [18,22,23]. As such, we chose to exclusively test our antibodies against: GHRH, sst2, VGAT, gephyrin, VGLUT2, PSD-95, shank2, NeuN, bassoon, piccolo, and Homer1; 2) will have similar numbers of GHRH- and sst2-expressing cells in the ARC; 3) will have similar total brain and ARC volumes as compared to mouse, given how similar in size the two are; and 4) will have a more consistent and predictable GH blood plasma pattern than *M. musculus* mice, as well as synchronicity in their rest-activity cycles. In sum, we expect *M. arvalis* to be more endocrinologically predictable in terms of GH secretion than *M. musculus*, while remaining similar enough to *M. musculus* to be accessible through our lab's usual neuroscientific tools. By establishing the vole's compatibility with our experimental setup, methods and protocols, we plan to use *M. arvalis* in future experiments, for example to follow up on some of our previous findings looking at the synaptic distance and synaptic population study that we carried out in mouse in our prior studies [18,22,23].

3. MATERIALS AND METHODS

3.1 Animal Housing and Tissue Collection

All animal procedures were approved by the Animal Care Committee of McGill University and conducted in compliance with the guidelines of the Canadian Council of Animal Care. Adult (10–13-week-old) C57BL/6 mice, from Charles River Canada (St-Constant, Quebec), were group-housed in groups of no more than five, under a 12-hour light, 12-hour dark cycle (lights on at 08:00 A.M and off at 08:00 P.M). Mouse chow and tap water were made available *ad libitum*. Adult (10–14-week-old [for the ELISA experiment] and 11–12-month-old [for the anatomical experiments]) wild-type *Microtus arvalis* voles, whose colony was supplied by our collaborators, the Storch Lab (Douglas Research Centre, Montreal, Quebec), were either group housed if weaned together, or individually housed if a male and female were born in a litter of two pups (litters are not mixed). Those voles used in the ELISA experiment were kept at the Douglas Research Centre's animal facility under constant darkness (DD), due to the Storch Lab's own experimental setup, which required the animals to be housed under DD in order to lift the effect of the circadian rhythm; this allows visualisation of the effect of the ultradian rhythm and associated brain regions, see Introduction (section 1.2), Results (section 4.4) and Discussion. Those used for our later anatomical experiments were kept instead under a 12-hour light, 12-hour dark cycle (lights on at 08:00 A.M and off at 08:00 P.M). at the Neuro (Montreal, Quebec) after the colony was entrusted to us by our collaborators. Moreover, of these latter voles, only those already slated to be euthanised due to age were used for whole brain extraction for reasons pertaining to colony management. Therefore, the latter voles used for the experiments we conducted ourselves were very old (11-12 months old). Mouse chow and tap water were available *ad libitum* and the boxes were filled with fresh hay and grasses (the voles need these to survive; they eat the hay and use it to nest). Prior to the blood tapping experiments in the voles, those animals being tapped were habituated to the test environment to try to curtail stress (tail-massage and human-touch, voice, and smell) for two to three weeks, about two minutes per day. Habituation was carried out by the same person who performed the blood analysis and produced the actograms. As is standard in the field, actograms were generated by measuring the voles' running wheel activity: a running wheel was placed in the cage and animals were free to use it whenever they desired.

To obtain the brains of both mice and voles, we performed a transaortic perfusion. Animals used while the colony was still at the Douglas Research Centre were anesthetised by administering a mixture of ketamine, xylazine and acepromazine via intraperitoneal injection prior to perfusion. Those used once the colony was moved to the Neuro Animal Facility were anesthetised with isofluorane until unresponsive, then perfused (isofluorane continued to be administered throughout the rest of the procedure). Perfusion was done with a 0.1M SPB wash at 8ml/min for five minutes and a 4% PFA in 0.1M PBS fixation at 8ml/min for ten minutes. Then the brains were immediately removed and postfixed in the same PFA solution for at least two hours. Following this, brains were immersed in 30% sucrose solution in 0.1M PBS overnight (or until the brains sank). The brains were then cut in two halves at about two-thirds caudally at the frontal end of the cerebellum, to facilitate sectioning with a flush embedding surface, and they were then immediately flash-frozen at -40°C in isopentane and stored at -80°C until sectioning.

Sectioning on both mouse and vole brains was carried out with a Leica SM2000R sliding microtome with cryo stage. Frontal brain halves were placed on the cooled stage (about -22°C) in a glue, Tissue-Tek, flush-side down (i.e., frontal side up) with the lateral aspect (temporal lobe) perpendicular to the knife to reduce both the amount of surface area exposed the initial cut and reduce damage to the area-of-interest (ARC). Brains were cut into 30µm thick sections and placed in 24-well plates, as per our previous experiments [18,22,23] and were taken from approximately -1.06mm to -2.92mm Bregma, according to the Paxinos Mouse Atlas [83]. Sections containing ARC and tuberal hypothalamus were selected on sight via location within the brain as well as tissue morphology, which included size and shape of the brain, presence of the median eminence, division of the optic chiasm into the optic tracts, morphology of the fornix, and the presence and morphology of the third ventricle. Those sections being used for stereology were selected such that they conform to the rules of stereology: every sixth section from a 24-well plate – composed of six columns and four rows – was picked, i.e., a single column was chosen, and this column was randomly selected; in other words, the section evaluation interval was 6.

3.2 Immunofluorescence Staining for Confocal and Widefield Stereology

Brain sections were incubated in a solution of 0.1% $NaBH_4$ in 0.1M TBS for 15 minutes and washed three times in 0.1M TBS with an extra 1% of NaCl (TBSN), five minutes each time. They were then incubated in a blocking buffer, consisting of 10% normal goat serum (NGS), 0.1%

Triton-X, and 3% BSA in 0.1M TBSN, for two hours. Immediately following this, they were incubated in a primary antibody solution, containing the antibody at a predetermined concentration (see Table 1), as well as 2% NGS, and 0.1% Triton-X in 0.1M TBSN; wrapped in parafilm; and kept at 4°C overnight.

The primary antibodies used were polyclonal rabbit anti-GHRH (AB5343 AB Clonal, Woburn, Massachusetts); monoclonal rabbit anti-sst2 and polyclonal mouse anti-PSD-95 (Abcam, Cambridge, United Kingdom); monoclonal rabbit anti-gephyrin, polyclonal guineapig anti-VGAT, polyclonal guineapig anti-VGLUT2, polyclonal rabbit anti-shank2, polyclonal rabbit anti-bassoon, polyclonal rabbit anti-piccolo, and monoclonal mouse anti-Homer1 (Synaptic Systems, Göttingen, Germany); and monoclonal mouse anti-NeuN (MAB377, Merck Millipore Sigma, Burlington, Massachusetts). All were used at the appropriate or revised concentrations (Table 1).

The following day, the sections were washed three times in 0.1M TBS with 1% NaCl and 0.1% Triton-X (TBSNT), five minutes each time. They were then incubated in a secondary antibody buffer, containing the secondary antibody at the appropriate concentration as well as 0.1M TBSN, 2% NGS and 0.1% Triton-X, for one and a half hours. Following this, they were washed in 0.1M TBSNT, then 0.1M TBSN, both three times for five minutes each time. They were then incubated in 0.1% DAPI in 0.1M TBSN for five minutes (for those experiments using DAPI), and finally washed three times in 0.1M TBS, five minutes each.

The secondary antibodies used over the course of this study were Alexa Fluor 488 (Jackson ImmunoResearch Labs, West Grove, Pennsylvania), Alexa Fluor 594 (Invitrogen, Carlsbad, California), Alexa Fluor 647 (Life Technologies, Grand Island, New York), Cy2 (Bethyl Laboratories, Montgomery, Texas), Cy3 (Jackson ImmunoResearch Labs), Cy5 (Jackson ImmunoResearch Labs for anti-rabbit; Bethyl Laboratories for anti-rabbit; or Abcam, Cambridge, United Kingdom for anti-guineapig), CF 568 (Biotium, Fremont, California) and Star Red (Abberior Instruments GmbH, Göttingen, Germany). All secondaries used were either anti-rabbit, anti-guineapig, or anti-mouse, depending on the primary antibody species antigen used. All secondary antibodies were used at a 1:500 concentration unless they were pre-diluted during aliquoting. DAPI (Invitrogen) was used at a dilution of 1:1000.

Following the secondary stain, the sections were mounted on gelatinised object slides and allowed to air-dry at least two hours, or overnight. To ensure clear imaging, we also dehydrated

and defatted the sections in serial soaks: 70% ethanol (diluted with double-distilled water) for two minutes, 80% ethanol for two minutes, 95% ethanol for two minutes, twice in 100% ethanol for five minutes both times, and finally twice in xylene substitute (Safeclear Xylene Substitute, PROTOCOL™, Fisher Scientific, Hampton, New Hampshire) for ten minutes both times. Following this, the sections were mounted in Permount (Fisher Scientific) and coverslipped. The object slides were allowed to dry at least overnight. See Results (section 4.2) for explanation on this part of the experiment.

For the experiment conducted to remove granules from the sections via pre-bleaching, we performed the test according to Sun, et al, whereby we shone bright light on the sections in 4°C for three days using the following set-up: A box lined with tinfoil, six pipette tip trays stacked in a pair of three acting as "legs" on which we laid the plate containing brain sections, under which we shone an LED desk lamp (TT-DL11, Taotronics, Fremont, California) set at maximum light intensity (386lm) [84]. Following tissue pre-bleaching, all experiments were conducted as normal.

3.3 Cresyl Violet Histological Staining

To visualise the ARC for our volume measurements, cresyl violet histological staining was performed. Extracted brain sections were washed six times in 0.1M PBS, for five minutes each time. They were then mounted on gelatinised object slides and allowed to air-dry at least two hours, or overnight. The object slides were then subjected to dehydration and defatting via an alcohol series: 70% ethanol (diluted in ddH_2O) for two minutes, 80% ethanol for two minutes, 95% ethanol for two minutes, 100% ethanol twice for five minutes each time, then xylene twice for ten minutes each time. They were then rehydrated using the same solutions in reverse order. Following this, they were left in 0.1M PBS for at least two minutes, and then incubated in 0.5% cresyl violet in a sodium acetate buffer (2.72% sodium acetate and 1.2% acetic acid in ddH_2O) for 15 minutes. Subsequently, they were differentiated twice in two separate dishes of fresh double-distilled water, one minute each time. Then they were dehydrated a second time, as above. Finally, they were mounted and coverslipped in Permount out of the second xylene, without delay, and left to dry.

3.4 Confocal Data Acquisition and Analysis

All confocal experiments were conducted using either a Zeiss LSM 880 confocal microscope (Zeiss Axio Observer.Z1 inverted) with a motorised x/y and z-Galvo stage, GaAsP

and multialkali PMT detectors, and X-Cite 120 LED fluorescence illumination system with emissions of 360-700nm (Excelitas Technologies) as well as 405nm, 561nm and 633nm solid state lasers and a 458/488/514nm multiline argon laser (Carl Zeiss Microscopy); or a Leica TCS SP-8 confocal (DM6 upright) microscope with a motorised x/y and Super Z Galvo stage, Ultra-sensitive high-signal-to-noise GaAsP-Hybrid Detectors (HyD), EL-6000 metal halide light and 405nm, 552nm and 638nm solid state lasers (Leica Microsystems). Images were acquired using 40× oil-immersion objectives (LSM-880: Plan-Apo 40×/1.4NA Oil; SP-8: HC PL APO 40×/1.30 OIL CS2 FWD: 0.24mm) at a zoom factor of 1.00. Both microscopes were optimised to detect DAPI, Cy2, Cy3, Cy5, Alexa Fluor 488, Alexa Fluor 594, Alexa Fluor 647, CF 568, and Star Red.

All images were cropped and processed using FIJI. As stated previously, no knock-out models exist for *Microtus arvalis*, and thus there is no quantification that can be carried out for the receptivity of antibodies to antigens in the vole. To make such a knock-out model is very labour-intensive and would have required time beyond the limits allotted for this project. As such, we opted to do a qualitative test instead. This means comparing, by eye, signal intensity and distribution between mouse (a species in which there is precedent for the antibodies working) and vole; namely, seeing if the antibody labels the same microscopic structures (axons, cell bodies, punctæ) in vole that we expect in mouse, at the same density and brightness.

3.5 Stereology Data Acquisition and Analysis

All stereological experiments were conducted using a Nikon Eclipse E800 microscope, with a motorised x/y/z-stage, colour CCD camera (Optronics, Microfire S99808, 1600×1200 pixel), standard transmitted light 12V halogen lamp, an X-Cite Mini+ compact 120 LED Illumination System with emissions of 360-700nm (Excelitas Technologies). Images were acquired using a DAPI filter set (Chroma, 49000, excitation: bandpass 350/50 nm; dichroic mirror: long-pass 400 nm; emission: bandpass 460/50 nm), a Cy3 filter set (Chroma, 49004, excitation: bandpass 545/30 nm; dichroic mirror: long-pass 565 nm; emission: bandpass 605/70 nm), a 10× air-immersion objective (Plan Apo 10×/0.45 DIC NI), and a 60× oil-immersion objective (Plan Apo 60×/1.4 Oil. DIC H).

The cell counting, or optical fractionator, stereology was conducted by acquiring images following the Optical Fractionator Workflow. First, the 10× objective was used for region-of-interest tracing, then the 60× oil-immersion objective was used for imaging proper. Once in a

particular location, to minimise bleaching, an image stack was collected, consisting of 30 frames with a frequency (i.e., z-step) of 1µm, giving a stack of 30µm height. Section mounted thickness was determined by manually measuring thickness at each counting site from which the program computed a mean thickness; it was this mean thickness which was used to calculate the cell estimation. Counting frame depth was defined as 8µm and guard zones as 1.5µm. Counting frame area was selected such that it would encircle two to three cells; in our case, 30µm x 30µm for voles and 35µm x 35µm for mice. Grid size was selected as that which would permit there to be around 10 counting sites per brain; in our case, 70µm x 120µm for voles and 90µm x 60µm for mice. The region-of-interest was defined as a roughly triangular region in which sst2-positive cells are found. Though sst2-positive cells are present across the brain, the arcuate nucleus (ARC) has a cell-poor perimeter, facilitating identification of the region. Cells were counted by tallying the number of cell-tops fitting within the constraints of the disector. Note that the CE's were generally around or below 0.1, however vole 2 had a CE of 0.2. Due to time and resource restraints, we chose to accept this as adequate. Of the four estimates the StereoInvestigator software calculates, we used "estimated population using number weighted section thickness", which weighs thickness when there are more cells in a given section and is generally considered the most accurate. Total Area (see Fig. 19B) was calculated by the StereoInvestigator software as the sum of all region-of-interest areas per section in each animal. Our in-house manual calculation of cell density was defined as the number of markers (i.e., cells) counted in each section, divided by the number of counting frames used in each section, for each animal.

The volumetric analysis, or Cavalieri, stereology, was conducted at 10× magnification, and thus represents a gross anatomical comparison. After the number of sections and the section evaluation interval were inputted, grid size was established using an arbitrary marker that conforms to the scale of the tissue and would allow for a reasonable area. In our case, we used the length of the crosshair cursor itself, which was 30µm. This means that a single grid square, as overlayed on the tissue, was 30µm x 30µm. The parameters for what to count were based partially upon consultation with the Paxinos Mouse Brain Atlas and partially on simple visual estimation for the more-difficult-to-tell cases [83]. Similar to above, the ARC generally appears as a dark, roughly triangular, area at the base of the third ventricle, often with a cell-poor sheath surrounding it. That said, towards the more anterior or posterior sections, it can take on a more oblong or even circular shape. We "coloured-in" the area of the ARC with different markers for each hemisphere (whose

measurements we later combined). Then the StereoInvestigator software inputted this into a statistical formula (see Introduction, section 1.4) to compute the volume. In several cases, the ventral-most aspect of the section was shorn off, either unilaterally or bilaterally. In these cases, we generally excluded the shorn area from the count. However, in some unilateral cases, there was enough apparent symmetry that we could approximate the size of the ARC in the shorn from the intact half; in these cases, we included the approximate area.

3.6 Brain Weight Data Acquisition

Since our brain extraction procedure requires immediate flash-freezing of the tissue to avoid damage, it was not possible to measure the volume of the brain after extraction while keeping the brain intact for later analysis. However, while we could have conducted a Cavalieri estimate, as in Methods (section 3.5), using a random interval of sections from a stack made up of the entire volume of the brain instead of only the ARC, we elected not to do so (see Discussion for more details on this decision). Instead, we opted to weigh the brains. Prior to freezing, in order to facilitate later sectioning by giving ourselves a flush and stable brain surface to which to glue the brain to the microtome's stage, we cut all brains into two at about 1/3 caudally through the frontal cerebellum. To weigh the brains, keeping them on dry ice, we weighed both halves of the frozen brain in a Mettler Toledo AL54 scale and immediately returned them to the dry ice. This was done as quickly as possible to reduce the time the brain had to thaw. Since the condensation ice (which develops on the brains when removed from the freezer) melts and the scale thus records a continuingly decreasing weight, we took the first weight the scale registered as the most accurate. Furthermore, it goes without saying that due to the presence of ice on the brain which adds weight, the brain masses are not accurately represented by the measurements. However, this fact is true for both mouse and vole which means the skew caused by the ice's weight is kept approximately constant between the two species, allowing us to make a comparison of their brain weight.

3.7 Blood Collection and Sandwich ELISA

As stated previously, GH secretion periods ("peaks") are short. This requires frequent blood tapping (as often as every 5-20 minutes) to accurately track the changes in the GH plasmic concentration [22,23,85]. However, using traditional methods such as saphenous vein tapping would be experimentally difficult due to the frequency of blood collection needed [85]. Furthermore, most traditional methods would require more blood than the animal could give in so

short a time, particularly considering the small size of both mice and voles [85]. Although exogenous blood could be used to replenish the removed blood, such instability in the cardiovascular system could greatly affect the animals' hormonal homeostasis [85]. We previously surmounted this problem by utilising what is known as the tail-clip method, where the tip of the tail is snipped off, producing a single drop of blood, which can then be sampled [22,23,85]. When the wound is closed by scabbing, by reopening the wound we are allowed to take multiple samples over the course of a day [22,23,85]. Such a small volume of blood collected was sufficient due to highly sensitive GH detection by Sandwich ELISA (Enzyme-Linked Immunosorbent Assay). This sandwiching effect (where the antigen is bound or "sandwiched" between two antibodies, one on a plate, the other applied) is what makes it highly specific, thus requiring little blood volume for a detectable sample [85,86]. The tail-clip-Sandwich ELISA method was devised in 2011 by Steyn et al. to observe the ultradian rhythmicity of GH secretion in mice over a six-hour period; and this method is simple, requiring comparatively inexpensive materials, no use of surgery, nor any radioactive materials [85].

To obtain a measurement of plasma GH in voles for this study, the tip of the vole's tail (about 2mm) was cut with a surgical blade and 2µl of blood was extracted with an Eppendorf pipette. The tail was cut once, and further blood extractions were carried out by gently squeezing the tail. Blood was extracted every 15-20 minutes for six hours. When the wound would begin scabbing, thus precluding any blood flow, it was opened by gently rubbing with a saline soaked cloth. The blood was transferred straightaway to 58µl of 0.05% PBS-Tween 20 and put on dry ice until all blood samples were collected. The blood samples were then stored at -80°C until the samples were analysed by ELISA.

Plasma GH levels were measured with the sensitive sandwich ELISA assay previously used [22,23,85,86]. A 96-well plate (Corning Inc., 9018) was coated with 50µl of monkey anti-rat GH antibody (AFP411S, NIDDK-NHPP, Torrance, California) at a dilution of 1:40,000, overnight at 4°C. The wells were all incubated with 200µl of blocking buffer, composed of 5% skim milk powder in 0.05% PBS-Tween 20, for two hours at ambient temperature. A standard curve was generated using two-fold serial dilutions of mouse GH (reference preparation, AFP-10783B, NIDDK-NHPP) in 0.05% PBS-Tween 20 with an additional 1ng/ml NGS, the final concentration being 0.2% NGS-Tween 20. Standard curve dilutions (duplicates) and blood samples (singles), at

a volume of 60µl each, were inserted onto the plate and incubated for two hours at ambient temperature on an orbital shaker.

The plate was then washed, and bound samples and standard curve dilutions were incubated for 90 minutes with 50µl of a detection antibody, rabbit antiserum to rat-GH (AFP5672099, NIDDK-NHPP), at 1:40,000. Following this, the samples were incubated for 90 minutes with 50µl of horseradish peroxidase-conjugated goat anti-rabbit antibody (BioRad) at a dilution of 1:2,000 in blocking buffer. By incubating the samples in every well with 100µl of O-phenylenediamine substrate (00-2003; Invitrogen, Carlsbad, California) for 30 minutes, we were able to produce an enzymatic colourimetric reaction. To stop the reaction, we added 50µl of 3.0M HCl. The absorbance was read at dual wavelengths of 490nm and 650nm with a microplate reader. By using regression of the standard curve, we calculated the concentration of GH in each well.

3.8 Statistical Analysis

All statistical analysis was conducted via either a one-tailed or two-tailed student T-test. We used a one-tailed T-test for brain weight and average cell density per counting frame because we were expecting the vole to have a smaller brain mass and less cell density than mouse, respectively; we used a two-tailed T-test for the ARC volume experiment because we expected that the ARC volume should not be different between species (see Results: sections 4.3 and 4.4, and Discussion).

4. RESULTS

4.1 Staining Optimisation and Confocal Antibody Verification in the Vole. Table 1 and Figures 1-18.

As a result of utilising tissue from a new species for immunofluorescence, the efficacy of the antibodies commonly or previously used in our lab required testing. Moreover, we discovered that our established immunostaining protocol proved to be less than optimal for our stereological goals, particularly using anti-GHRH: under the widefield microscope used for stereology, the poor signal-to-noise ratio (SNR) we observed made cell-counting difficult, if not impossible, so the immunofluorescence staining required optimisation (see explanation in Discussion). In particular, the challenge in widefield image analysis is that tissue sections diffract light, thus creating background fluorescence, which may obscure signals in the plane-of-interest. In fact, this is in large part the reason other more specialised forms of microscopy were created. To improve the SNR of our immunostain, we mounted tissues on gelatinised object slides and subjected them to dehydration in serial alcohol concentrations followed by defatting in xylene and then cover-slipping in Permount (for more, see Methods: section 3.3). The fluorophore we chose for visualisation, Cy3, withstands this harsh treatment and retains much of its fluorescence. The differences were immediately noticeable between any of the stainings performed prior to the change and after. In the pre-optimised tissue, our immunofluorescence was very bright with some tissue architecture visible (holes, representing nuclei), but it was all very blurry (Fig. 1). In fact, it was very difficult to focus on the tissue at all. The optimised antibody staining was much improved: it was much less bright and tissue architecture (nuclei) was more apparent, in more detail, all with less diffraction.

We then qualitatively analysed the various immunofluorescence antibody stains between vole and mouse, via comparison, per area, of the signal intensity, as well as the density of cell bodies, axons and punctae. Ideally, antibody staining in the vole would be controlled for using a genetic knockout model, where, upon removal of the particular gene and thus the particular protein that the antibody recognises, one could assess the antibody's specificity with more certainty (given that the protein is not essential to sustaining life). However, no genetic knockout models of voles are available to date. In both cases it was compared by eye, since the goal was not to make any

particular comparison, but rather to establish if the antibody can be used in the vole, as in the mouse. We considered an immunofluorescent stain to be similar between vole and mouse via the following qualifications: 1) if a difference of signal intensity between the two species was not immediately apparent, or one was not obviously dimmer or brighter (for punctae this may also include the size of the punctae: too large in one species may imply excess antibody is binding to a given antigen); and 2) whether the density of objects that were to be stained (such as axons, punctae, or cell bodies) and the pattern of such stained objects is similar between species (e.g., it should not have stained axons in one species and punctae in the other).

Overall – although three antibodies needed optimisation in the concentration applied, and two of them did not work at all – the antibodies seemed to target the correct proteins-of-interest in voles, as assessed visually by comparing the vole's staining pattern, intensity, and density to that of the mouse. Recall that punctae in brain tissue represent clusters of the targeted presynaptic or postsynaptic proteins: markers for axonal terminals and presynaptic active zones, or postsynaptic densities, respectively [62,63]. Below are the results for each of the antibodies we tested, which we compared to the dilutions that we have already established in our lab as working in mouse and rat. For more information regarding these antigens and their staining patterns, see the Introduction: section 1.3. Also, the optimal dilutions – whereby through brightness, density, and pattern we could easily distinguish tissue architecture in vole as to mouse – are summarised in Table 1.

- ***Controls (Fig. 2)*** The controls were performed to see if Cy3 (our main secondary antibody)'s signal labelled the tissue non-specifically. The controls show there was a little non-specific staining, though some of that staining may have been "granules", see below. But across the tissue, there was nothing that matches the staining of any of the antibodies we tested. Furthermore, Cy3 labelling did not interfere with the DAPI stain.
- ***GHRH, Growth Hormone Releasing Hormone (Fig. 3)*** is normally stained in our lab at 1:200 in the mouse and we expect to see stained cytoplasm (with the hormone inside the cell). However, staining produced dim cell bodies all around the tissue and while it might appear that the stain demonstrates labelled neuropil (there was staining all around the tissue with puncta-like structures in both mouse and vole), it is known that GHRH is not present in the neuropil. This staining was puzzling and not caused by the

unspecific binding of the secondary antibody (see *Controls* above). See final paragraph of this section for further details.

- ***Sst2, Somatostatin Receptor Subtype 2 (Fig. 4)*** is stained in mouse at 1:3000 with an expected staining of axons and cell bodies. At that dilution, cells and axons were labelled brilliantly (perhaps better in vole, as seen visually via comparison of signal intensity) with a roughly similar density. Since cell bodies and axons were very well labelled, so no adjustments were necessary.
- ***VGAT, Vesicular GABA Transporter (Figs. 5 and 6)*** is stained at 1:1000 in mouse and we expect to see many punctae all over. When stained at 1:1000 in vole, the signal was rather dim with a looser distribution than expected based on previous findings in the mouse (Fig. 6). It was different enough to warrant some optimisation. By increasing the concentration in voles two times to 1:500, the staining was rendered adequately bright and dense (Fig. 6). A pattern of many punctae particularly centered around nuclei was apparent with or without the change in concentration.
- ***Gephyrin (Figs. 7 and 8)*** is stained at 1:500 in mouse with an expected staining of punctae, and because gephyrin is a postsynaptic protein of inhibitory synapses, we expected punctae to be clustered around cell bodies and proximal dendrites. In vole at 1:500, the signal was much dimmer and loosely distributed (Fig. 8). As with VGAT, the staining's pattern warranted optimisation. When the concentration was increased to 1:100, the vole's signal corresponded to what we expect in mouse (Fig. 8).
- ***VGLUT2, Vesicular Glutamate Transporter 2 (Fig. 9)*** is stained at 1:5000 in mouse; we expect to see punctae, and because the punctae represent presynaptic vesicles containing the VGLUT2 protein, which are in synapses which often contact the soma, we expect to see these punctae around the nuclei in particular. In vole, the staining produced a slightly dimmer and more sparsely distributed signal, however, we believe it was close enough to use the same concentration.
- ***PSD-95, Postsynaptic Density - 95 (Figs. 10 and 11)*** is stained at 1:500 in mouse and we expect to see punctae distributed across the tissue, with the occasional cell visualised. In vole when stained at 1:500, we got a very similar staining pattern, however it was slightly denser and the background too bright (Fig. 11). As such we

elected to decrease the concentration to 1:1000, at which point the vole's staining pattern became similar to the mouse's (Fig. 11).

- ***Shank2 (Fig. 12)*** is stained at 1:500 in mouse and we expect to see punctae distributed across the section. What we saw were punctae distributed across the section as expected, though, strangely, we also saw cell bodies. Like with PSD-95, at the typical concentration vole tissue was too bright, but of relatively similar density. Though it was a little more intense, we believe that 1:500 remains functional.
- ***NeuN, Neuronal Nucleus (Fig. 13)*** is stained at 1:500 in mouse and we expect to see only neuronal cell bodies and the occasional neuronal cell process. At the normal concentration, staining in voles produced the expected result.
- ***Piccolo (Fig. 14)*** is stained in mouse at 1:500. We expect to see punctae, and possibly cell bodies, all over the section. At the normal concentration vole tissue presented the expected staining.
- ***Bassoon (Fig. 15)*** is stained at 1:200 in mouse and staining is expected to label punctae, and possibly cell bodies, all over the section. We saw the expected punctae, and there was also strong labelling of the cell bodies. In voles it was slightly brighter than in mouse in the typical concentration. Like with Shank2, we consider this difference to be negligible enough to continue using 1:200.
- ***Homer1 (Fig. 16)*** is stained at 1:500 in mouse. Expected staining labels punctae all over the section. In our experience, this antibody is most challenging to use. It did not produce very good staining in either species. In vole, there was excessive background labelling, but there was still some apparent punctae despite the background staining. We discovered these "punctae" were in fact "granules", see below.

Using the GHRH stain, we quickly discovered the presence of non-specifically labelled cells (Fig. 17) and "granules" (Fig. 18). These both confounded effective counting of cells. In the GHRH fluorescent stain, there was faint labelling of cells across the entire brain in both mouse and vole, and most of these sections lacked a bright triangular ARC region. Doing a secondary antibody control removed these cells, suggesting that the primary antibody itself was non-specifically binding to the tissue (Fig. 2 and 17). However, we have had success with this anti-GHRH antibody before in mouse (both in earlier experiments in the present project and in previous projects [22,23]), so we tried another company's GHRH antibody, but found that different primary

GHRH antibodies produced no different effect (data not shown). Moreover, the "granules" were found in clumps resembling even more strongly the GHRH-typical stain and were also widespread throughout the brain (Fig. 18). The "granules" also had the peculiar quality that they were visible in all spectra aside from far-red. We were able to elucidate the causes of the presence of the "granules" (autofluorescence present even in unstained tissue, see Discussion, for further details), but we were unable to elucidate the cause of the non-specific labelling of the GHRH antibody, and as such, further GHRH stereological analysis will be left for a future project. That said, in the sst2 staining, there were no non-specifically labelled cells, and the granules interfered less. Therefore, we were able to complete the sst2 stereological analysis without much difficulty.

4.2 Sst2 Stereology. Figures 19 and 20.

We conducted this experiment to compare the estimated number of somatostatin receptor subtype 2 positive (sst2+) cells in the arcuate nucleus (ARC) between mouse and vole. Our data using the optical fractionator showed a large variation of estimated cell numbers between individuals within the mouse, precluding statistical analysis (student T-test or Wilcoxon Signed-Rank test) of the estimates. Therefore, instead of comparing the mean of each species' estimates (which appeared inappropriate), we examined the "raw" estimated number of sst2+ cells in the ARC, specifically the "estimated population using number weighted section thickness" calculation of StereoInvestigator. In general, the mouse group had a larger estimated number of cells compared to the vole group: mouse 1, 12,441.17; mouse 2, 31,647.45; mouse 3, 73,117.62; vole 1, 6,593.07; vole 2, 14,822.85; and vole 3, 6,259.05 cells (Fig. 19A). In search of a possible explanation for the variation within the mouse group, we plotted the total area observed in the area-of-interest using StereoInvestigator per ARC in each animal sampled: mouse 1, 458,825.0; mouse 2, 1,302,430.0; mouse 3, 1,934,850.0; vole 1, 261,721.0; vole 2, 658,340.0; and vole 3, 457,503.0 μm^2 (Fig. 19B). On this same graph we also plotted the total volume observed in the area-of-interest as measured by StereoInvestigator's Optical Fractionator per brain in each animal sampled: mouse 1, 82,588,400.0; mouse 2, 234,437,000.0; mouse 3, 348,272,000.0; vole 1, 47,109,800.0; vole 2, 118,501,000.0; and vole 3, 82,350,500.0 μm^3 (Fig. 19B). As with the cell estimates, there was too much variation in the ARC area as well as the ARC volume in the mouse group to allow us to conduct statistical analysis. In general, the mice had a much larger total area and volume as compared to the voles, and the bigger area or volume, the more objects would be counted; thus, as

can be expected, the absolute number of sst2-positive cells was also higher. Since it was self-evident that the larger the area and volume, the more we would count cells, an absolute count (and the resulting estimate) of sst2+ cells was not a metric that made sense for a comparison. As such, we needed a measure of how many cells there were in vole ARC compared to mouse, proportional to the size of the brain. So, rather than an estimate of absolute cell numbers, it made more sense to look at the relative density of sst2+ cells. We defined density as the number of sst2+ cells per number of counting frames in the region-of-interest. In this way we avoided the distortive effects of area and volume we see in the above data. However, in doing so the data is no longer an unbiased estimate. Nevertheless, this can still give us an idea as to the characterisation of the tissues. See the Discussion for more in depth treatment of this analysis.

At the same time, while conducting this sst2 stereology experiment, we carried out a proper ARC volume experiment. We found that the ARC volume between mouse and vole brains was not significantly different (see Results: section 4.4, below). Thus, we hypothesised that the density of sst2+ cells in vole must be lower to account for this. To obtain a density of cells per frame per animal we took the ratio of the unestimated "raw" cell counts per section per animal in relation to the number of counting frames per animal used for counting. See Fig. 20A, where average mouse cell density per frame is 2.6 ± 0.29 cells and average vole cell density per frame is 1.8 ± 0.23 cells. There was a small, but significant difference ($P \leq 0.05$, specifically 0.049) between the densities in mouse and vole according to a one-tailed student T-test. Furthermore, looking at the tissue, this difference was visible: generally, vole had fewer cells in the tissue than mouse (Fig. 20B). Both mouse and vole groups had the same distribution of male to female animals.

4.3 Gross Anatomical Comparisons Between Vole and Mouse, Figures 21 and 22

We conducted a comparison of the weight of the brains and the volume of the ARC to better understand the relationship of ARC size to brain size, between the vole and the mouse. As with the sst2 stereology experiment above, considering the ARC volume in context, an absolute ARC volume may not reveal much due to the animals' brains being of visually different size; as such, by also looking at the proportion of ARC volume to total brain volume, we could get a better representation of the difference of ARC volume between both species. Ideally, we would compare the ARC volume to the volume of the brain, however, due to procedural constraints, it was

impossible to conduct total brain volume measurements, so instead we chose to measure total brain weight and compare that to ARC volume (see more in Discussion).

For total brain weight, our initial hypothesis was that because vole brains are visibly smaller, the vole brain should be less massive. Indeed, we found mouse total brain weight was on average 0.37 ± 0.007g and vole total brain weight was on average 0.33 ± 0.01g. Furthermore, there was a significant difference between the two species' total brain weight ($P \leq 0.01$, specifically 0.008) according to a one-tailed student T-test (Fig. 21). Both mouse and vole groups had the same distribution of male to female animals.

For ARC volume, our initial hypothesis was that, given how conserved the ARC is across species and how phylogenetically related mice and voles are, ARC volume should not be significantly different between species [30]. We found that on average, mouse ARC volume was $0.22 \pm 0.01\text{mm}^3$ and vole ARC volume was $0.21 \pm 0.03\text{mm}^3$. Furthermore, there was no significant difference between either species' volumes, according to a two-tailed student T-test (Fig. 22). Both mouse and vole groups had an equal distribution of male and female animals.

4.4 Plasma GH Levels and Rest-Activity Pattern in the Vole. Data Not Shown.

Note: due to the Covid-19 pandemic, the subsequent lockdown, and time restraints, this experiment was generously conducted by the Storch Lab at the Douglas Research Centre on our behalf. As such, it only represents one iteration of testing, under certain experimental condition, specifically: the animals for this part of the experiment were kept under constant darkness (DD) [Singh Markam and Storch, unpublished observations]. DD desynchronises the brain's endogenous circadian rhythm from environmental cues; now decoupled and out of sync with the environment, an underlying rhythm is revealed, and this is called a free-running rhythm [87]. DD also potentially desynchronises ultradian rhythms from circadian rhythms. Though this has minimal effect on feeding or running-wheel behaviour of the voles because their activity rhythms are linked to the ultradian SCN-DUO pacemaker and not a circadian pacemaker [56,57,60].

For this experiment, GH plasma concentrations between individual voles (random gender) as measured by sandwich ELISA and the activity levels (i.e., behaviour) between animals were compared. Blood was sampled in all voles every 20 minutes for six hours, 17 times in all. Vole 4 began sampling in a peak at 12:26, it reached another very small peak at 14:46, and a larger peak

at 17:06, appearing to end the sampling period at 17:46 in a trough. Vole 5 started at 12:26 in a trough which lasted until 12:46, then reached a peak 1:06, it reached a second smaller peak at 15:46 and appeared to be entering another peak at 17:46. Vole 6 also started in a trough at 12:26, which lasted until 13:06 from which it reached a peak at 13:26, with a second, smaller peak at 17:26 [Singh Markam and Storch, unpublished observations]. In sum, Vole 4 had peaks at 0, 140 and 280 minutes; Vole 5 had peaks at 40 and 200 minutes; and Vole 6 at 60 and 180 minutes after the start of sampling [Singh Markam and Storch, unpublished observations]. With just 20 minutes between Vole 5 and Vole 6's two peaks, it is not unreasonable to conclude that they were relatively synchronised. Although peaks in Vole 4 may at first appear to be more frequent than Voles 5 and 6, it appears that there is a phase shift of about 60 minutes with the peak at 0 minutes likely corresponding to the first peak of the other two voles. Furthermore, the basal rhythm of a peak roughly every 150 minutes or 2.5 hours was conserved in all three voles. The absolute GH plasma levels (ng/ml) varied between animals. Vole 4 had a maximum of about 4.25ng/ml, Vole 5 had a much higher maximum of about 11.5ng/ml, Vole 6 had a maximum of about 4.25ng/ml, and all three voles had a minimum of about 0ng/ml. Thus, the range of vole 5 was much larger than the other two voles [Singh Markam and Storch, unpublished observations]. This is an interesting phenomenon that we also saw in our previous project, which can likely be explained by taking individual biological differences into account [22,23].

As the voles were kept in constant darkness (DD) but with access to a running-wheel, rest-activity cycle data for each animal was also obtained [Singh Markam and Storch, unpublished observations]. All three voles had an onset of activity about every two hours (that is, roughly two hours between activity bout onsets). This is consistent with the established literature on vole activity rhythms [48]. In terms of the length of the activity period, Vole 7 had shorter-lasting bouts of activity (approximately 20-30 minutes every two hours), versus Voles 8 and 9 which had longer activity periods (approximately 60-90 minutes every two hours) [Singh Markam and Storch, unpublished observations]. Moreover, between animals, most of their activity periods were consistent between animals each day. For example, between 22 and 24 hours, all three animals had an activity period [Singh Markam and Storch, unpublished observations]. This is remarkable, considering that these animals were kept in constant darkness, i.e., the external circadian clock governed by light was abolished [87]. In sum, while their activity was not 1:1 the same, each hour, each day, the three animals were remarkably synchronous in their activity patterns.

5. DISCUSSION

The first step in this project was to test all our previously used antibodies to verify that they can be used in vole. Since, unlike mice, *M. arvalis* has no knockout models, we were limited in how to test the efficacy of the antibodies. For the purposes of this study, we decided qualitative analysis would be adequate: visually comparing mouse tissue, in which our stains are known to work, to vole tissue, which is unknown. Ultimately, aside from GHRH and Homer1, they seemed to have similar patterns of staining and intensity, though some needed a change in concentration (Table 1; Figs. 2-16), those being gephyrin, VGAT and PSD-95. Moreover, not only did the sst2 antibody work as expected, but sst2-like immunostaining encouragingly appeared more brilliant in voles as compared with mice. Some of the stains also had additional phenomena. Strangely, shank2 (which is known to gather at dendritic spines) strongly stained the cell bodies in addition to the expected punctate staining pattern throughout the neuropil. As mentioned earlier, punctae represent presynaptic or postsynaptic proteins and may be inferred to represent axonal terminals, presynaptic active zones, or postsynaptic densities. The reason for Shank2's cell body staining could not be established. One might speculate that postsynaptic complexes containing Shank2 may be already preassembled at the neuronal cell body [22,23]. Either way, the observation is consistent between species, so it is not too much of a concern for our purposes. Moreover, the Homer1 stain not working does not come as a surprise; in our lab's experience, it has always been a difficult immunofluorescent stain to work with. Furthermore, with VGAT, we see staining within the cell surrounding the nucleus (which is not stained and can be seen as a dark "hole"); this is unexpected since synaptic vesicular proteins are cycled very fast to the axon and little remains in the cell body. The following could possibly explain this staining pattern: 1) non-specificity of the primary antibody, though this is unlikely as the antibodies are KO-verified; 2) the antibody has such high affinity for the antigen that it manages to stain vesicles before they traffic to the axon; or more likely, 3) because presynaptic terminals, which contain synaptic vesicles (like those containing VGAT), are often found surrounding postsynaptic cell bodies on all sides, above and below the focal plane and this makes it appear as if there were VGAT immunofluorescence in the cell body.

For all the antibodies we tested, although we have secondary stain controls which verify that fluorescence is not caused by non-specific binding of the secondary antibody, we would need a primary antibody control to verify that the primary antibody is specifically binding. The best way

to do this is via genetic avenues: knockout or knockdown models where the antigen is removed, and the tissue then incubated with the antibody; however, this was beyond the scope of this project, given the lack of such models in vole. Another idea could be to use an antigen binding assay, in which we first incubate the antibody with the antigen it is supposed to bind to, before incubating the tissue with the primary antibody. This assay is a negative control: we expect to see no binding to the tissue, as all the antibodies should be bound to the free-floating antigen. However, this assay would require us to use the vole specific amino acid sequence (in particular for GHRH) and that is not commercially available, and our lab is not equipped to make it ourselves. In general, from visual observation, it appears that many commercially available antibodies successfully target our proteins-of-interest in vole brains. As such, the qualitative results obtained thus far are a visual and qualitative indication of the useability of mouse antibodies in the vole.

At first, our normal immunofluorescence staining procedure appeared appropriate for this study. However, once we switched from confocal to the widefield microscope we used for stereological analysis, some problems cropped up. First and foremost, there was a blurriness, or low signal-to-noise ratio, to the samples. This was caused by a mismatch in the refractive index of the tissue, mounting medium, and the objective oil used on the microscope. It was not as visible on the confocal microscopes because they, by nature, only scan the image at the plane in focus, rejecting out-of-focus light, while widefield microscopes "see" light from all planes, giving the appearance of so-called "background fluorescence" which interferes with imaging. We decided to apply the histological technique of dehydration and delipidation in order to remove the main causes of tissue background fluorescence, which is to say fat and water. This markedly improved the contrast of our stains (Fig. 1). However, it is worth noting, this switch to dehydrating and defatting meant we also had to change which secondary antibodies we used. Cyanine (Cy) dyes are particularly resistant to losing their fluorescence following this process, in contrast to other more sensitive dyes we were using, like the Alexa Fluors. Moreover, we also observed that great improvement came from using Permount as a mounting medium instead of Aqua-Poly/Mount (the former has a refractive index closer to objective oil than the latter).

We found that our GHRH stain produced non-specific staining (in a manner similar to a normal GHRH immunofluorescent stain) across the whole brain tissue in both animals, and though the neuropil was nicely defined, it is not supposed to be labelled. Our secondary antibody control

revealed that the non-specific staining was due to the primary antibody (Fig. 17). We also observed fluorescent granules located in clusters around the nucleus in neurons throughout the brain that looked remarkably like GHRH staining (Fig. 18). They appeared to be lipofuscin granules which are a known histological problem for neuroscientists. It is currently unknown what lipofuscin is precisely, but it is known to be most common in old, especially senescent cells; they are described as lysosomes that accumulate indigestible waste like carbohydrates, metals and oxidised lipids and proteins [88]. Lipofuscin is perhaps most notorious because it is particularly common in postmitotic cells such as retinal cells, neurons, and cardiac myocytes [88,89]. The contents of these lysosomes are autofluorescent and emit light concurrently in all spectral bands, from 400nm to 700nm, i.e., all except the far-red channel [88,89,90]. Our observed problem correlates very strongly to this visual description. Furthermore, all the animals used for the stereology experiments were older animals obtained towards the end of their lifespan. Thus, it is unsurprising that we should find lipofuscin under such conditions. There are a few ways to remove this autofluorescence, such as staining our sections in the presence of Copper Sulfate ($CuSO_4$) or quenching with Sudan Black B or TrueBlack® [91,92,93]. However, $CuSO_4$ has a negative effect on immunofluorescence, although its deleterious effect is stronger on the unwanted autofluorescence; Sudan Black B would have required that we not use any kind of detergent, and it introduces a strong red background fluorescence; and TrueBlack®, though an improvement over Sudan Black B due to less red background fluorescence and the ability to be used following the secondary stain, is incompatible with our usual organic mounting media [84,92,93]. In 2017, Sun et al. published an elegant paper proposing a cheap and effective solution to this problem: we could expose our tissue to bright light for three days to pre-bleach the tissue and in so doing, remove the autofluorescence. What is more, no protocol change is needed for this to work: after pre-bleaching, we merely need to continue the protocol as usual [84]. This worked remarkably well: the granules were almost all removed to the point where it no longer resembled any stain (Fig. 18). All other antibodies still stained as expected, and if affected by the granules, the granules could be disregarded because of the difference in the pattern of staining. Nevertheless, due to the appearance of the unspecific binding of the GHRH antibody, we abandoned quantifying GHRH-positive cells.

In our sst2 immunofluorescence staining, although the lipofuscin granules were still visible, they did not impede sst2-positive cell identification, as the granules form a pattern very different from the sst2 staining. Upon performing sst2 cell-count estimation in voles and mice, a

large difference in raw estimate number was observed between individual mice, in other words, the data was not parametric and could not be pulled together for statistical analysis (Fig. 19A). The large difference in cell number estimation within the mouse group correlates with the large difference in observed arcuate nucleus area and volume associated with the cell-estimate dataset (Fig. 19B). This comes as no surprise since a given experimental group in a stereological analysis must have the same parameters (i.e., identical length and width for all grid squares as well as all counting frames), which means we usually expect the region-of-interest to be of similar size within a group. Naturally, if the region-of-interest is larger in a given animal and has a fixed parameter set, the number of grid squares will be higher, which results in more counting frames, which thus allows for the possibility of higher number of cells able to be counted. Moreover, minute changes in the region-of-interest can change estimated measurements dramatically, e.g., if we add an extra little bit to the spinal cord radius, this dramatically increases its volume; additionally, region-of-interest selection is the step in the optical fractionator most prone to observer bias. Due to these two last points, density could be said to be a more appropriate measure of choice than absolute number. As such we could have conceivably taken the sst2+ cell-number estimates and divided them by an ARC volume estimated in a similar way using the Cavalieri method (which we did in fact calculate, see paragraph below and Fig. 22). However, as discussed above, it is the relationship between estimated cell counts of each animal that is problematic, and as such, we could not define density as the estimated number of cells divided by an estimated volume (such a calculation would not remove the nonparametric variance in the mouse group). Furthermore, we could not define density as the number of objects counted per the estimator's calculated area or volume, as neither the area nor the volume obtained by the optical fractionator estimator could be compared between mouse and vole (Fig. 19B). This issue is caused by the relationship between the size of the region-of-interest in each species, which translates into the number of counting frames and the difference in area, and thus the volume; the latter of which is used in the estimator formula (see Introduction, section 1.4) and which impacts the cell estimation. Therefore, there is no way to reconcile the data obtained by our estimation. For this reason, we instead defined density as the number of objects counted per counting frame in each species so that we need not take area and volume into account. To compare these counting frame cell densities in the ARC, we applied a one-tailed t-test since we already knew from the estimated cell comparison that there are more cells in the mouse than vole.

The statistical analysis shows a significant difference with a p-value of 0.0495, which, though significant, is not a dramatic difference, consistent with the error bars on the graph (Fig. 20A).

To obtain quantitative measurements of the vole brain's physical features, we measured and compared the weight of the vole and mouse brains and measured the volume of the ARC using basic histology and a volumetric stereological analysis called Cavalieri Estimation (see Introduction, section 1.4). We found that the vole brain was significantly less massive than the mouse brain (Fig. 21), which does not come as much of a surprise since the vole brains are visibly smaller (which would suggest smaller volume and smaller mass). Interestingly, there was no significant difference between the ARC volumes in vole and mouse (Fig. 22). Given that we can visually confirm that the volume of vole brain is smaller and that the measured brain mass is also smaller, this would suggest that the ARC in voles is possibly larger relative to the total brain as compared to mouse. In fact, this is consistent with known neuroscience: since voles are highly synchronised and thus have a high activity in the ARC and SCN, it stands to reason that such hyper-utilised areas should be larger in vole. This is much in the same way humans have proportionally larger cerebral cortices as compared to many other mammals. It also lines up with our observation of the larger pituitary gland in the vole proportional to the size of the brain (see below). That said, such a comparison is not ideal because we are comparing two different measurements (weight and volume – although the vole's total brain volume is *visibly* smaller) and the resolution of the measurements is different: the ARC volume was done using the Cavalieri estimator and thus by definition, the results have a very small margin of error, while the total brain mass was measured using a typical lab-grade scale and has a much less insignificant margin of error. Furthermore, part of the brain freezing process included incubating the brains in a 30% sucrose solution (and then subjecting them to flash freezing in isopentane) to cryoprotect them and prevent freezing artefacts, like ice crystals, from forming [94]. Specifically, the sucrose solution is a hypertonic solution which forces water out of the cells, in this way precluding crystal formation; this loss of water volume has the effect of shrinking the brains as well, and thus our freezing protocol might have influenced our results as has been observed by others [94]. That said, we also fixed the brain tissue with PFA, which has the effect of solidifying soft tissue when well-fixed, and as such, the tissue should largely have held its size and shape despite the dehydration caused by the sucrose solution. Moreover, the frozen brains were weighed very quickly to minimise any noticeable effect on our measurements caused by vapor condensation, subsequent

freezing and then unfreezing. Taken together, though the effects of sucrose shrinkage and melting condensation might skew the data in a single species, the bias applies to both groups, so it is not unreasonable to compare the data. Additionally, instead of measuring brain weight, we could alternatively have measured the total brain volume. This would have been relatively straightforward: in the same way we measured the ARC volume, we could have used the Cavalieri method, and a random interval of sections chosen from a stack consisting of the entire brain and contoured each brain section's entire circumferential area. However, we chose not to do such an analysis; recall that to process the brains for sectioning, we cut off the caudal third of the extracted brain before flash-freezing to create a flush and stable surface with which to glue it to the microtome's frozen stage. To glue it, we apply Tissue-Tek into which we insert the brain and, because the caudal end of this frontal two-thirds of brain is embedded in the glue, we lose that from sectioning. For our normal experiments this is not a problem, but for a total brain volume estimate it would not be suitable. Furthermore, the caudal third of the whole brain that is flash-frozen but unsectioned is too small to section since most of it would be imbedded in the glue. Therefore, to conduct a Cavalieri estimate of the total brain, we would need to have used a different sectioning process for the volumetric experiment, perhaps a paraffin embedding sectioning protocol, but we are not equipped to carry out such a procedure, and, because we must maintain antigen integrity, such a protocol would render the sections difficult to use for every other immunofluorescence application for which we use the sections. This is something that would be worth considering doing in a future project. As a final consideration of this observation, the ARC is part of a very ancient region of the brain (hypothalamus) which tends not to differ much between animals. As such, though merely conjecture, it may well be that despite the overall brain being of different sizes between the two species, the apparent largeness of the vole ARC is not a reflection of a proportional increase of vole ARC volume, but rather more a proportional lack in size of other parts of the brain, such as cerebral cortex. As such, as another future line of inquiry, it would be interesting to see if the entire hypothalamus (and perhaps other brain regions) also differs in volume between mouse and vole, or if it is specifically the ARC.

The results of the Sandwich ELISA experiment (provided by our collaborators, the Storch Lab, at the Douglas Research Centre) indicate GH release rhythmicity between voles, where the peaks of GH secretion in voles 5 and 6 occur at similar time points (around 50 minutes past the first blood collection point) and the peak of vole 4 occurs at the time of the first collection point

(about 50 minutes earlier than the other two voles) [Singh Markam and Storch, unpublished observations]. Although the group size of three animals is small, one could formulate a hypothesis for future investigation: when trying to predict a peak of GH secretion in voles, two out of three animals will be sacrificed at the right time due to the voles' colony synchronicity, though with more experiments this could be further elucidated. This is significantly better than in mice, where many more animals needed to be euthanised to obtain a peak. It is worth mentioning that there is a procedural time difference in the blood sampling procedure: one animal is treated at a time, and the sampling procedure (removing the animal from the cage, opening the closed wound, pipetting the blood out, putting the Eppendorf tube on ice, and returning the animal to the cage), takes about 5 minutes per animal. As such, ideally more than one person would perform the blood collection at a time to prevent an unnecessary time lag between animals. Additionally, our collaborators' project was being conducted under constant darkness (DD). This was done because putting an animal under DD eliminates the link between the animal's endogenous circadian rhythm and the external circadian rhythm (i.e., sunlight), and in doing so, will reveal the animal's endogenous circadian rhythm, called a free-running circadian rhythm, which was useful for the purposes of their research but made no difference to our study [87]. In the case of the voles, their activity rhythms do not change, and, as already described in the Introduction (section 1.2), this is because their activity cycles are linked to their ultradian rather than circadian rhythm.

An interesting next step would be to further elucidate the voles' GH synchronicity over the course of two or more days. For example, in the experiment conducted by our collaborators (not shown), there was a peak at 15:30 in all animals. Would there have been a peak in the animals around the same time the following day? Given the consistency over 10 days in the actograms produced by our collaborators (not shown; see below), it stands to reason that the GH profile would also stay consistent between days; if so, this would allow us to confidently narrow our time slot selection for obtaining a vole experiencing a GH peak. Furthermore, there is a difference of magnitude between the voles' GH baseline blood concentration. This was observed before in our lab: mice had a different magnitude of absolute GH plasma concentration. As before, this is not concerning as it is expected that individual animals will have differing baseline absolute concentrations of circulating hormone. What is more important is that the pattern of GH plasma secretion be internally consistent enough to find a cyclic release pattern.

Along with the GH profiles, our collaborators provided us with an actogram of three voles (please note that these voles are from a different group than the ones used for GH blood profiling) [Singh Markam and Storch, unpublished observations]. The voles have a nearly identical roughly two-hour cycle, according to the actograms, which is consistent with the literature on the length of their ultradian rhythms [48]. Additionally, as found by others, the data shows that a given vole's rest-activity cycle is consistent between days, with a two-hour activity period the same time each day. The voles had more daily consistency in a single animal than did mice in our previous project [22,23], and all three voles had remarkable synchrony between individuals. Furthermore, due to the connection of both rest-activity and hormonal oscillations with the ultradian SCN-DUO timer [56,57,60], and the fact that, like the rest-activity cycle rhythm, the GH plasma concentrations peak roughly every two hours, it is very likely that the voles are indeed more synchronised than mice with regards to GH release (and perhaps other rhythmically released hormones too).

Work with the voles also illuminated certain challenges. For one, vole tails are very short and very fragile; unlike mice, they cannot be picked up by the tail, as it can detach. This happens in the wild to enable the vole to escape once captured by the tail (e.g., one of their predators, the black stork, flings them into the air by their tail to catch them in their beak) [28]. Secondly, in mice and rats, it is common to massage the tail in a "milking" fashion to encourage blood flow after tail-clipping, but this is considerably harder in vole as, again, the tail may detach. Thirdly, as described in the Introduction (section 1.1), stress abolishes the GH profile, so animals need to be habituated to reduce their stress response [8]. However, although the voles are very friendly compared to mice (they can be thought of as rats in mouse bodies) the voles turned out to be harder to habituate. Whereas mice might take a few days to a few weeks to habituate, voles ended up taking months. This is likely because although they have been bred in the lab long enough to be considered inbred, they are still wild animals, unlike mice; tame but not domesticated. Fourthly, our collaborators work specifically with the methamphetamine-sensitive ACTH system, and as an additional interesting finding, they discovered *M. arvalis* is immune to the effects of methamphetamine at the ACTH level, rendering the animals unusable for their project [Singh Markam and Storch, unpublished observations]. Though such a finding would appear to be unrelated, this was the first major instance of a cross-species difference noticed over the course of this project, further illustrating a major difference between the two species; for that reason, it is worth pointing out.

It is also worth mentioning that immediately upon extracting the vole brains, we noticed that vole pituitary glands were much easier to remove intact than those of mice. Even though voles and mice have comparable body sizes, vole pituitary glands are large in proportion to the brain, in fact, almost as big as a sesame seed! In comparison, mouse pituitary glands are about as large as a grain of sand. This increases the vole's possibility of use in (neuro)endocrinology and (neuro)anatomy. As with the ARC, it is tempting to speculate that their pituitary glands are so disproportionally large because neuroendocrine regulation is involved in their social synchrony, similar to how animals with keener senses of smell have larger olfactory bulbs. Another interesting observation is that the vole brain appears to have a different shape from the mouse brain: it is flatter and wider. What effects this may have on brain function, if any, are currently unknown.

Taken together, all our observed differences (the ARC-volume-to-total-brain-weight proportion, brain shape and size, apparent difference of sst2+ estimated cell counts, difference of sst2+ cell density, and their apparent non-reaction to methamphetamine) could be potentially related to the relative phylogenetical distance between voles and mice (interestingly, voles are more closely related to hamsters than to mice and rats) [30, Singh Markam and Storch, unpublished observations]. It is important to note that for all these neuroanatomical observations, the old age of the animals may have influenced the results. It is possible that both aged mouse and vole brains have a lower volume and weight due to normal age-related atrophy, and perhaps there is a likewise decrease in aged animals' number of GHRH and sst2-positive cells as compared to young-adult animals. However, a "younger" animal would still be an adult animal and the differences should not be as dramatic as with a pup. Furthermore, as age is most notably implicated in declines in memory, fine-motor coordination, and reasoning, we expect age to have a stronger effect on the volume of the hippocampus, cerebellum, and cerebrum, respectively, and as such, even if the effects of age dramatically skew our other results, these effects may not be so noticeable on the volume and cellular distribution of the ARC. Aside from all these observed differences, the vole appears more synchronised than the mouse (from both the GH plasma profiling and the rest-activity data) [Singh Markam and Storch, unpublished observations] yet retains the ability to be recognised by most of the commercial antibodies established in our lab. This makes the vole well suited to GH neuroendocrinology studies.

6. FINAL CONCLUSIONS

In sum, over the course of this project we compared the neuroanatomy and neuroendocrinology between *Mus musculus* mice and *Microtus arvalis* common voles, to the end of investigating if voles are a viable model to use in lieu of mice. We found that voles are largely compatible with our established commercial antibodies, with some (VGAT, gephyrin and PSD-95) needing optimisation, and some others (GHRH and Homer1) encountering issues. Furthermore, while we found that mouse brain weight is significantly larger than the vole's, our results show that the vole arcuate nucleus (ARC) is proportionally larger than the mouse ARC. We also found that mouse tissue has a higher density of sst2+ cells than vole tissue. Finally, our collaborators found that there are indications that vole plasma GH daily patterns are more consistent than in mouse. In addition, we had some setbacks with regards to the GHRH staining itself as well as absolute cell number estimation, due to the variability of mouse ARC area; and there were some challenges in using the vole, namely: their tails are especially fragile making their handling more complicated, they take longer to habituate than already established animal models, and they are interestingly unresponsive to methamphetamine at the level of their circadian rhythm. Despite these challenges, we believe that along with our other findings, their synchronicity (as the most important aspect of our study) shows much promise. Going forward, the next natural step would be to collect more data on the GH hormonal synchrony of the voles, namely, to see if their synchrony and internal consistency carries over more than one day. It would also be interesting to see if this synchrony applies to other pituitary hormones, as well as how the synchrony is affected by different conditions, such as sex, hunger states, stress, etc., and to do so in young-adult animals to rule out any confounding by very old age. As per Matthews and Vosshall (2020), because the genetic code of *M. arvalis* has already been recorded [25,95], we currently sit at the third step of their ten-step outline ("assemble [the animal's] genome and profile its gene expression"). Thus, once the hormonal synchrony is established, we could begin creating antibodies against specific proteins, properly conduct antigen preabsorption tests, or even create genetic models using *M. arvalis*, such as GFP tagged proteins and knockouts, knockins, or knockdowns. It is our hope that this study assists others who hope to expand the animal model repertoire beyond the "Big 6", particularly in our field of neuroanatomy and neuroendocrinology where interspecies synchronicity is required, and thus our findings may broadly fulfill the three Rs of animal research, thereby lessening the use of animals, resources, and the labour required for such studies.

7. TABLES, FIGURES AND APPENDICES

Table 1: Summary of the different antibodies tested as well as their function, clonality, established dilution in mouse and rat, and functional dilution in *Microtus arvalis* voles. Tilde (~) indicates dilutions that needed to be modified during optimisation.

Antigen	What it targets	Clone	Dilution in mouse and rat	Dilution in voles
GHRH	GHRH hormone, primarily in the cell body	Polyclonal	1:200	1:200
Sst2	Somatostatin receptor subtype 2 on cell surface	Monoclonal	1:3000	1:3000
VGAT	Inhibitory presynaptic vesicular protein	Polyclonal	1:1000	~1:500~
Gephyrin	Inhibitory postsynaptic microtubule-associated protein	Monoclonal	1:500	~1:100~
VGLUT2	Excitatory presynaptic vesicular protein	Polyclonal	1:5000	1:5000
PSD-95	Excitatory postsynaptic scaffolding protein	Polyclonal	1:500	~1:1000~
Shank2	Excitatory postsynaptic-density adaptor-protein	Polyclonal	1:500	1:500
NeuN	Neuronal Nucleus	Monoclonal	1:500	1:500
Piccolo	Presynaptic scaffolding protein	Polyclonal	1:500	1:500
Bassoon	Presynaptic scaffolding protein	Polyclonal	1:200	1:200
Homer 1	Postsynaptic excitatory scaffolding protein	Monoclonal	1:500	1:500

Figure 1: Results of optimisation of the staining protocol to improve the signal-to-noise ratio (SNR). Stained with anti-GHRH primary (1:200 dilution) and Cy3-conjugated secondary antibody in vole arcuate nucleus tissue. The scale bar is 50μm in length and images were obtained with a 60× oil-objective on a Nikon E800 microscope. Insets, to the right of the main micrograph, are magnified 3 times. 3V = Third ventricle.

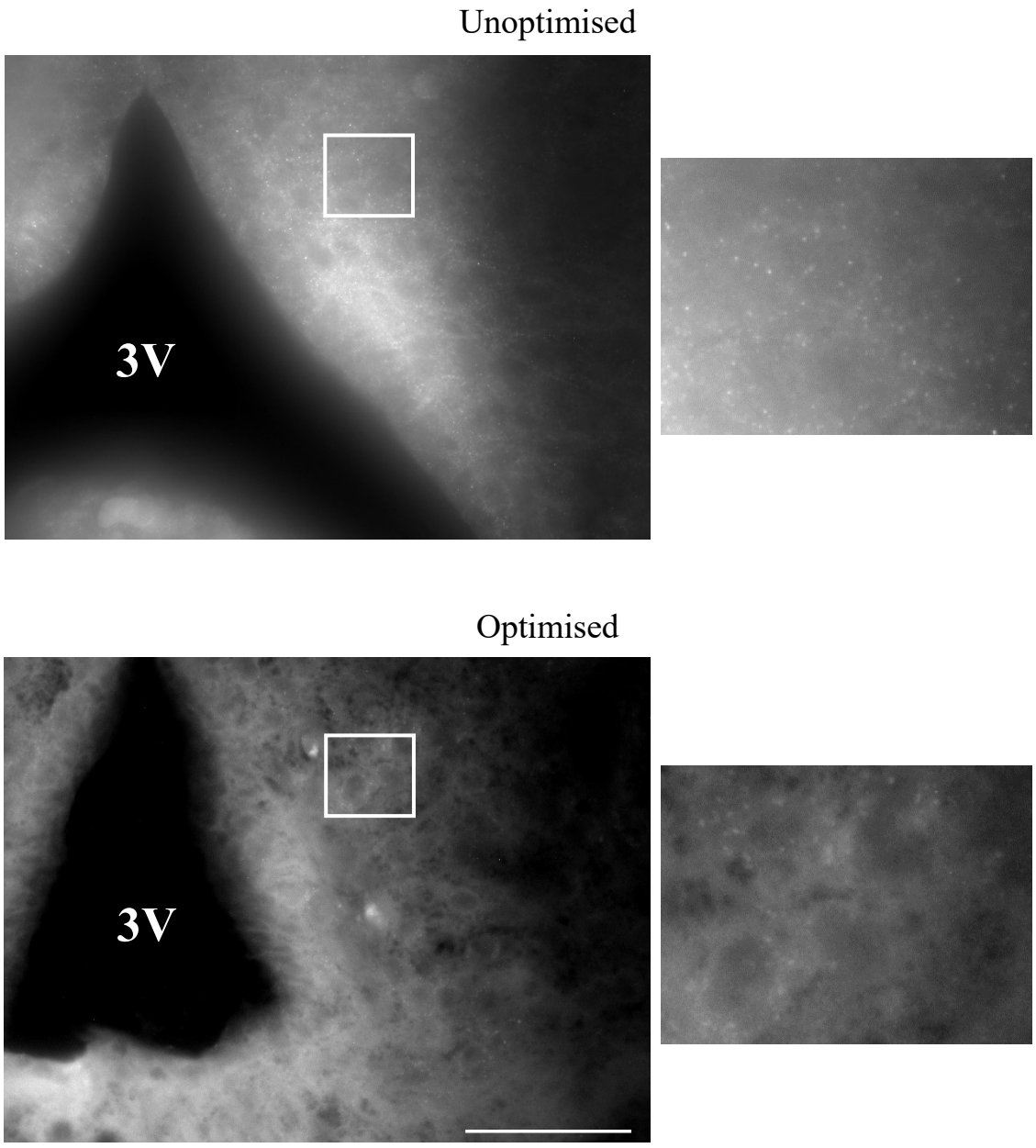

Figure 2: Secondary Antibody Control: Cy3-conjugated secondary antibody with a DAPI counterstain in the arcuate nucleus. The scale bar is 50μm in length and images were obtained with a 40× oil-objective on a Leica SP-8 microscope. Insets are magnified two times. 3V = Third ventricle.

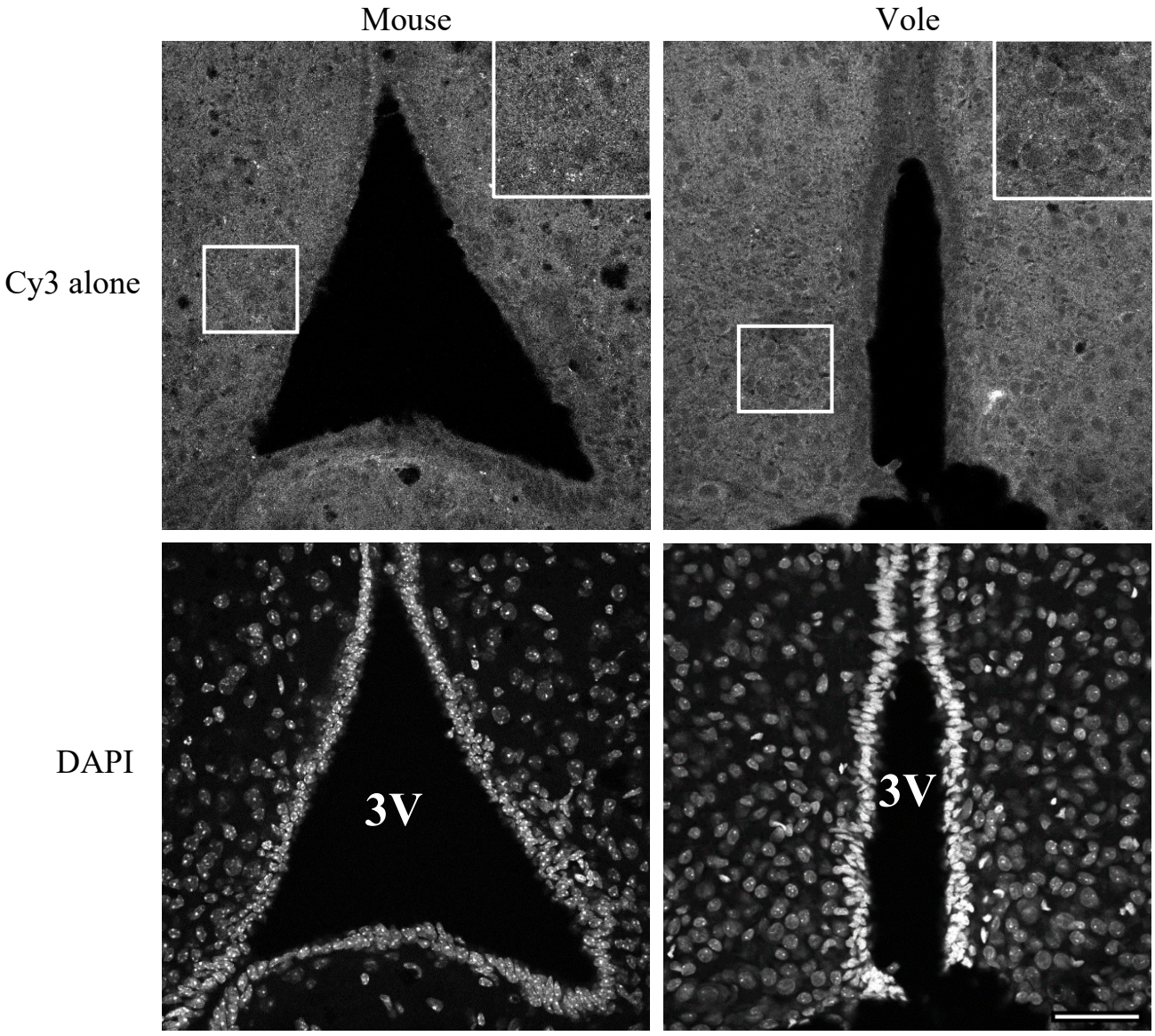

Figure 3: anti-GHRH primary antibody with Cy3-conjugated secondary antibody and DAPI counterstain in mouse and vole brain arcuate nucleus tissue. Dilution at 1:200 in both species. The scale bar is 50μm in length and images were obtained on a Leica SP-8 microscope with a 40× oil-objective. Insets are magnified two times. 3V = Third ventricle.

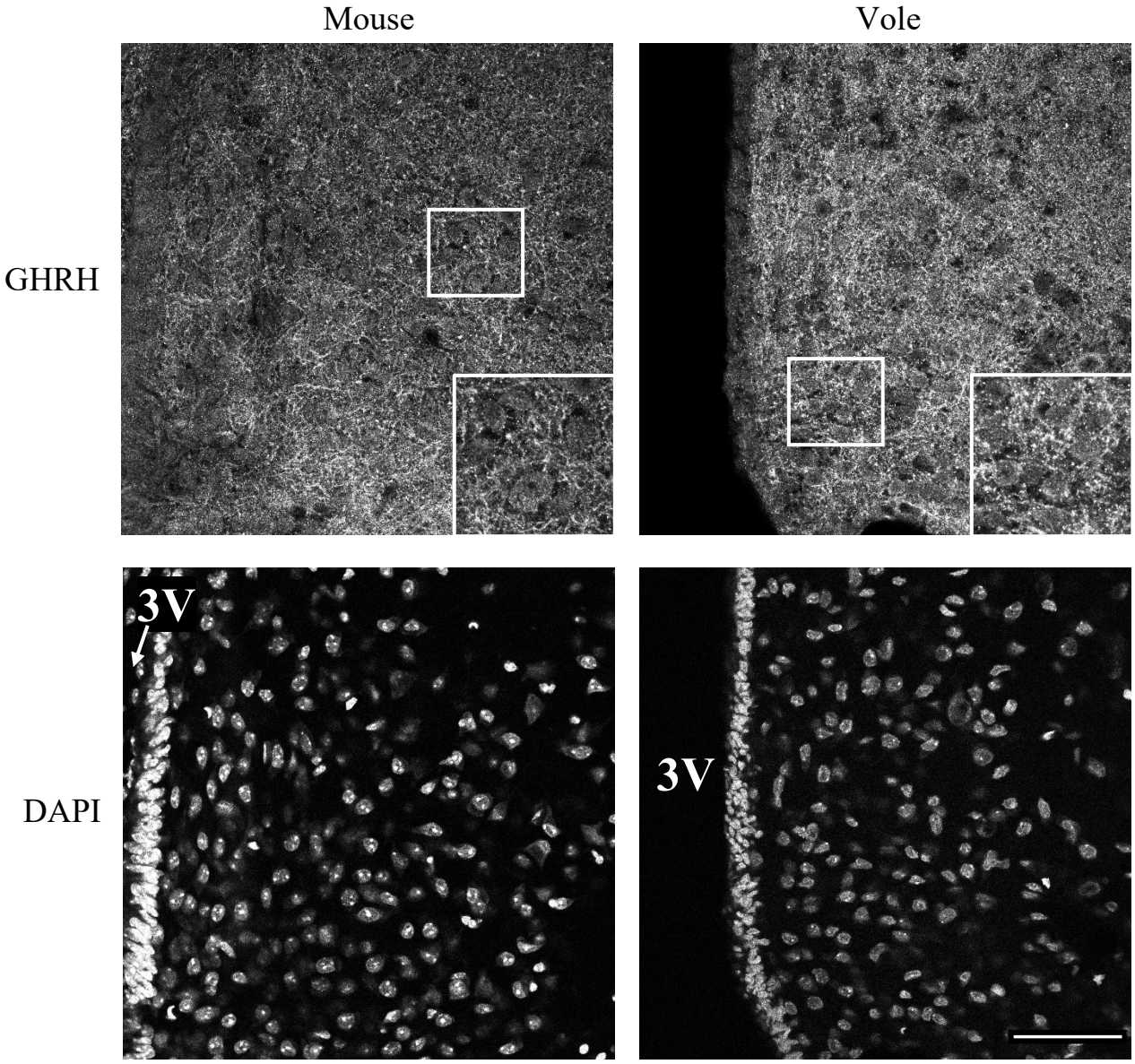

Figure 4: anti-Sst2 primary antibody with Cy3-conjugated secondary antibody and DAPI counterstain in mouse and vole brain arcuate nucleus tissue. Dilution at 1:3000 in both species. The scale bar is 50μm in length and images were obtained on a Leica SP-8 microscope with a 40× oil-objective. Insets are magnified two times. 3V = Third ventricle.

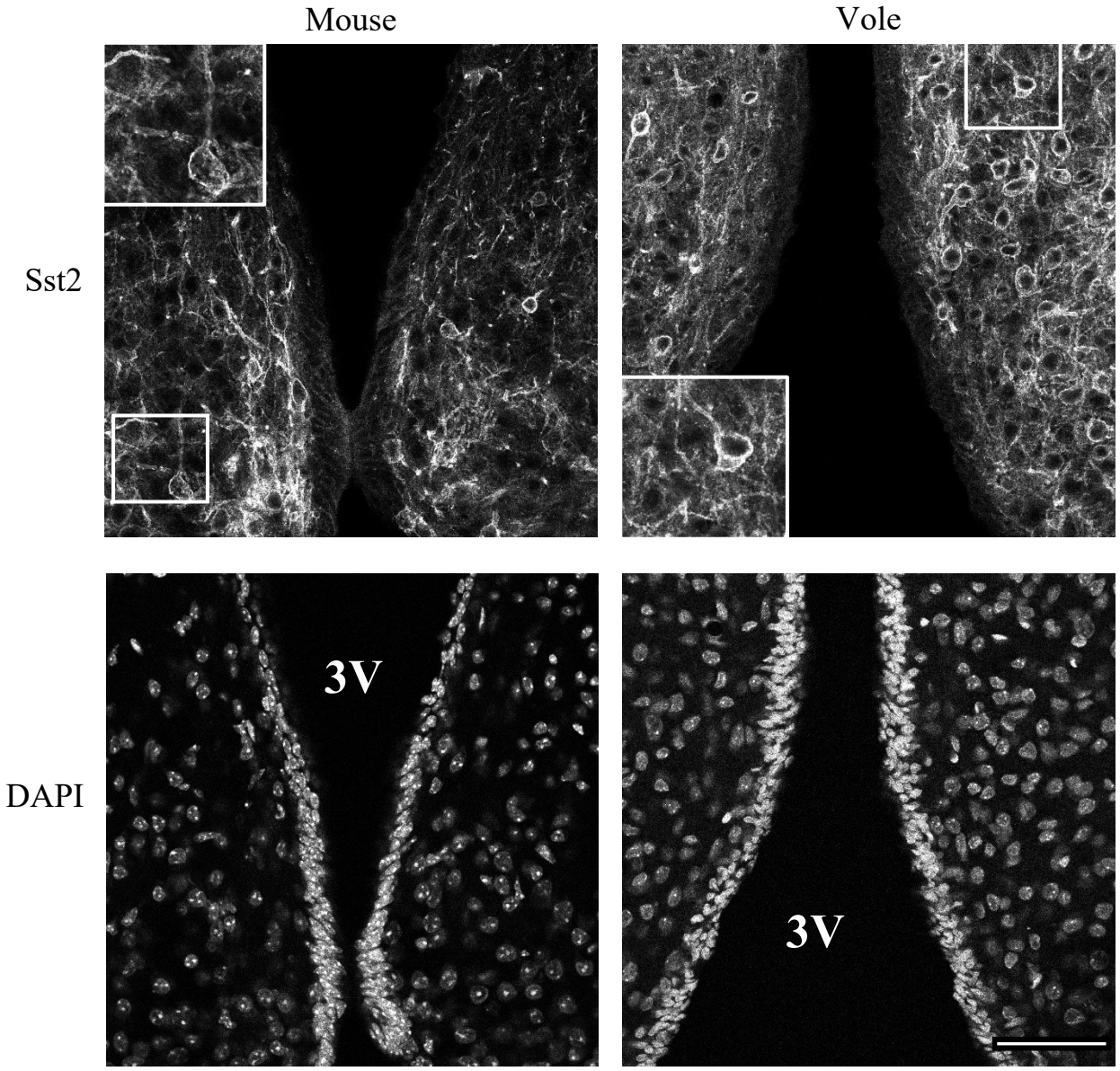

Figure 5: anti-VGAT primary antibody with Cy3-conjugated secondary antibody and DAPI counterstain in mouse and vole brain arcuate nucleus tissue. Dilution at 1:1000 in mouse and 1:500 in vole. The scale bar is 50μm in length and images were obtained with a 40× oil-objective on a Leica SP-8 microscope. Insets are magnified two times. 3V = Third ventricle.

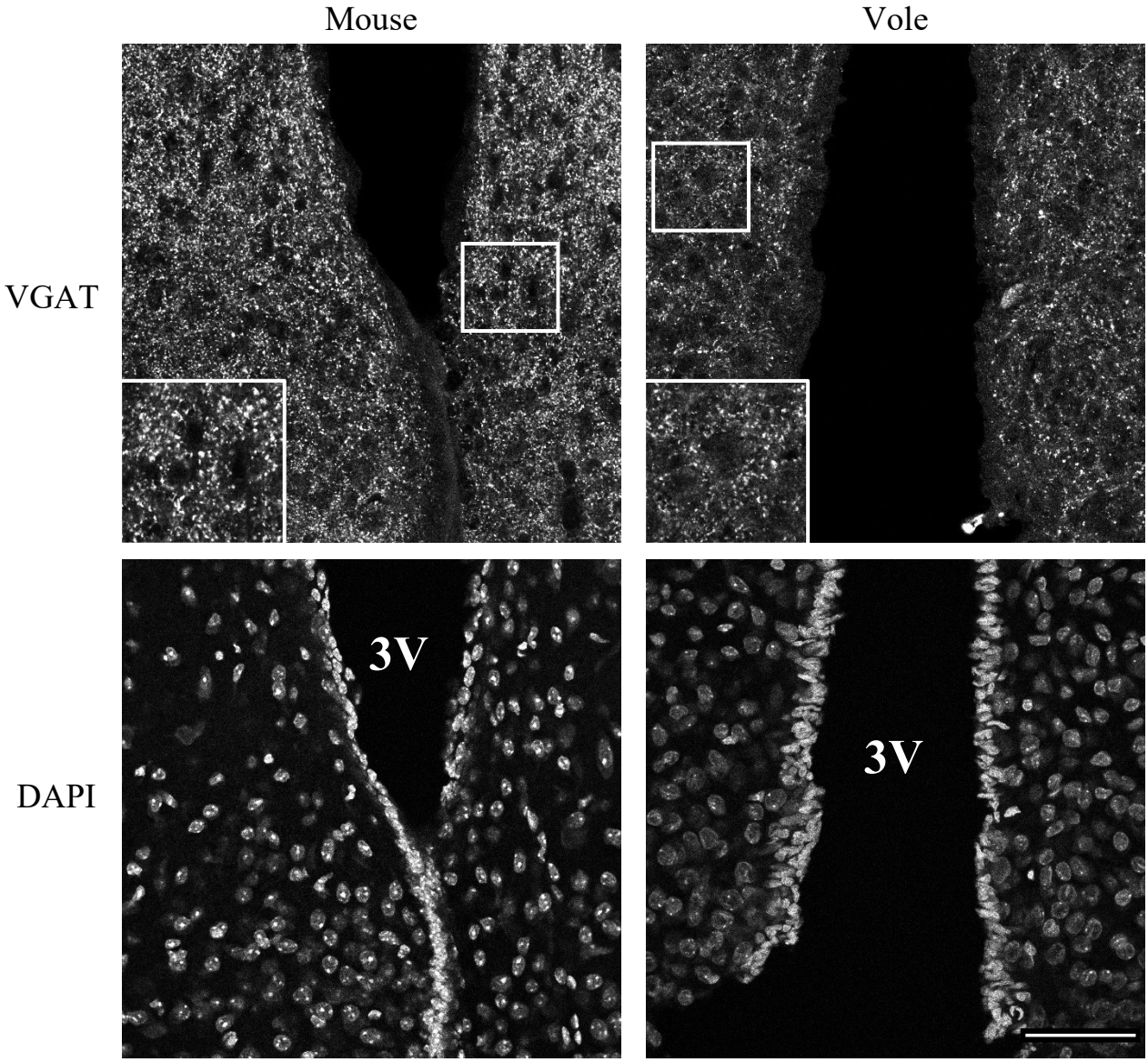

Figure 6: Concentration comparison of anti-VGAT primary antibody stains with Cy3-conjugated secondary antibody in mouse and vole brain arcuate nucleus tissue. The scale bar is 50μm in length and images were obtained with a 40× oil-objective on a Leica SP-8 microscope. Insets are magnified two times. At the normal concentration of 1:1000, staining in vole was slightly too sparse, and the intensity a little too weak. When increased to 1:500, vole tissue more closely matched that of mouse.

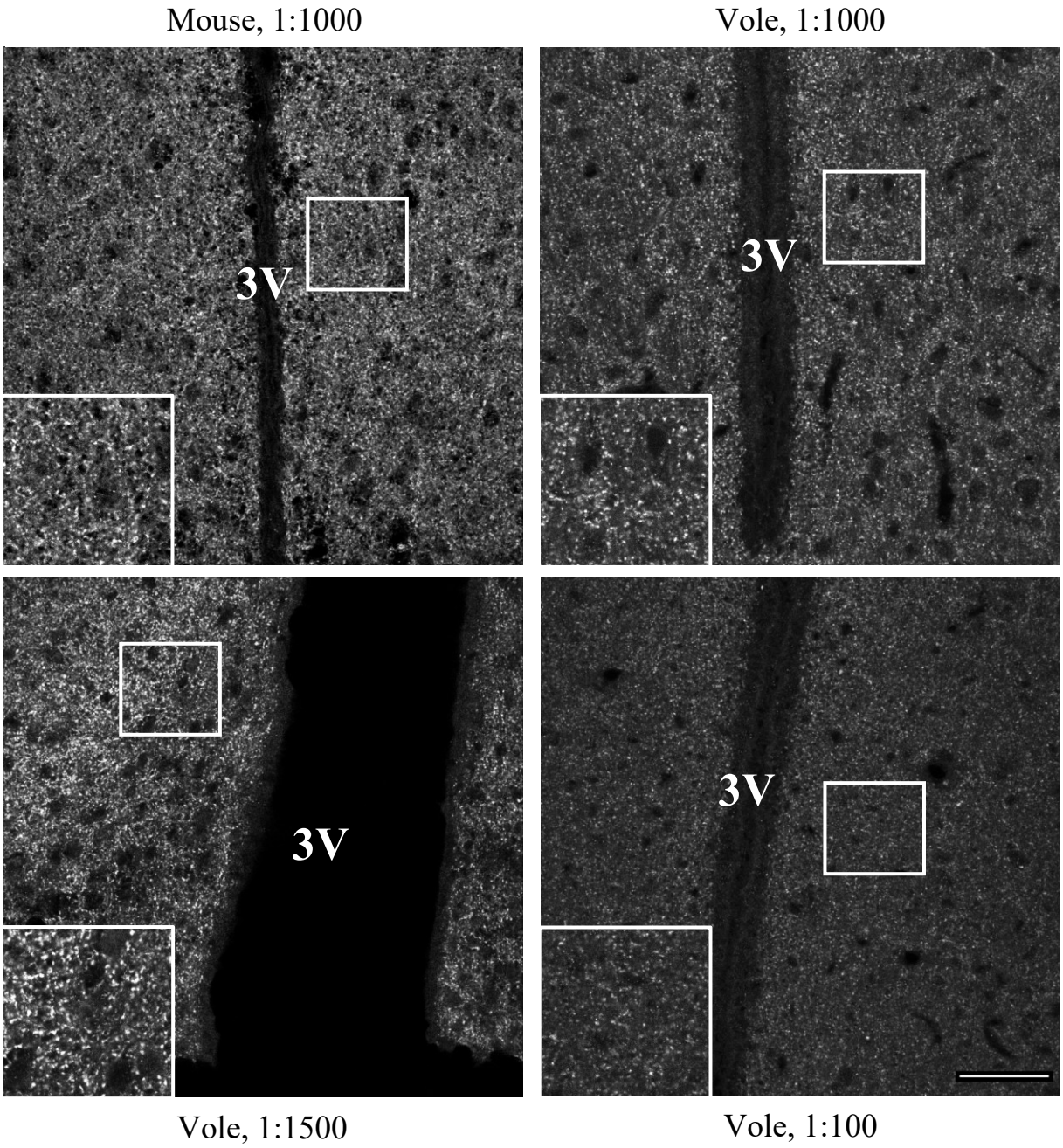

Figure 7: anti-Gephyrin primary antibody with Cy3-conjugated secondary antibody and DAPI counterstain in mouse and vole brain arcuate nucleus tissue. Dilution at 1:500 in mouse and 1:100 in vole. The scale bar is 50μm in length and images were obtained on a Leica SP-8 microscope with a 40× oil-objective. Insets are magnified two times. 3V = Third ventricle.

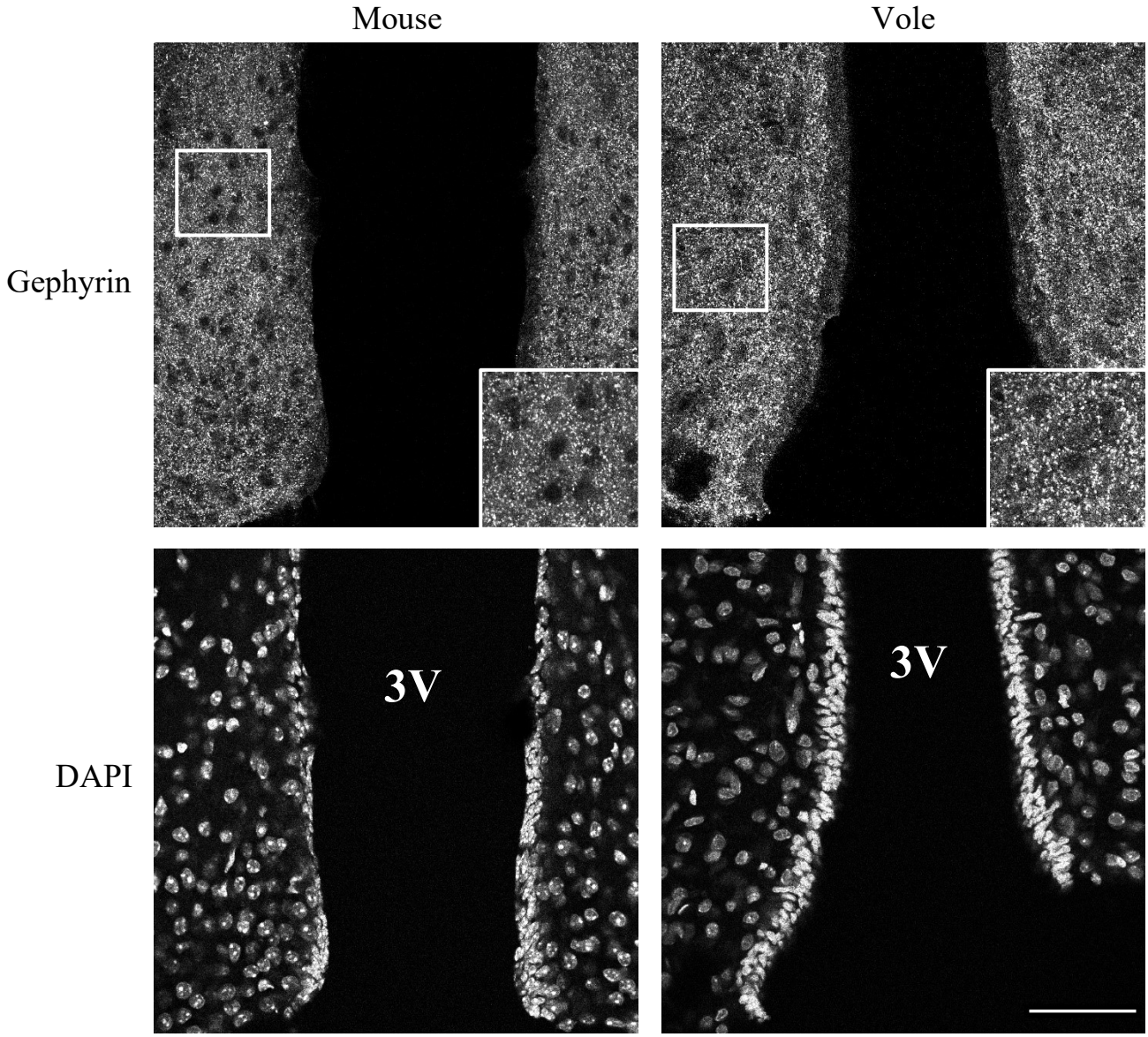

Figure 8: Concentration comparison of anti-Gephyrin primary antibody stains with Cy3-conjugated secondary antibody in mouse and vole brain arcuate nucleus tissue. The scale bar is 50μm in length and images were obtained with a 40× oil-objective on a Leica SP-8 microscope. Insets are magnified two times. At the normal concentration of 1:500, staining in vole was markedly too sparse, punctae much smaller, and intensity barely visible. When increased to 1:100, vole tissue matched mouse tissue reasonably well. This was the most concentrated it is cost-effective to go while nearing closer to a match between species.

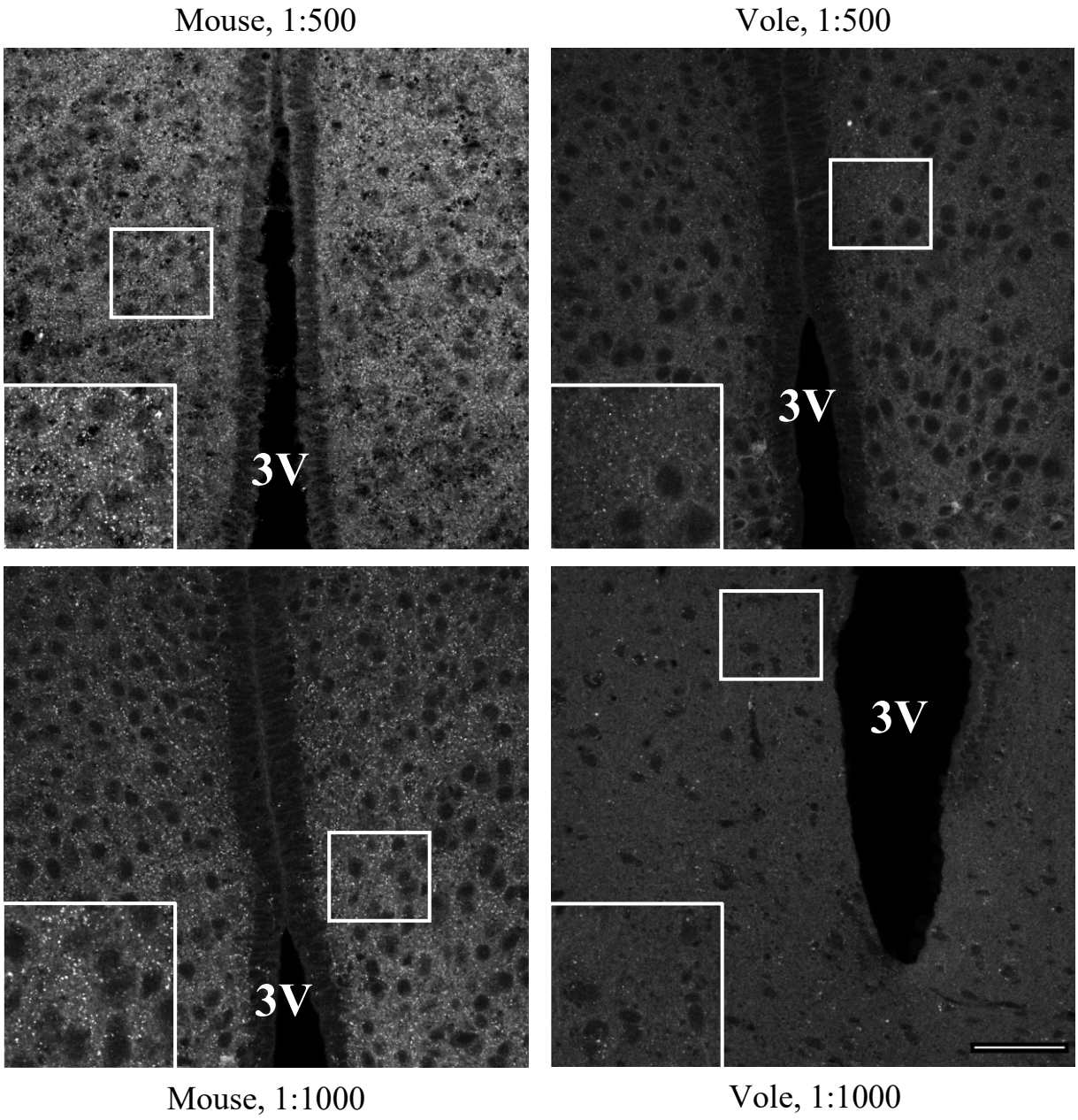

Figure 9: anti-VGLUT2 primary antibody with Cy3-conjugated secondary antibody and DAPI counterstain in mouse and vole brain arcuate nucleus tissue. Dilution at 1:5000 in both species. The scale bar is 50μm in length and images were obtained with a 40× oil-objective on a Leica SP-8 microscope. Insets are magnified two times. 3V = Third ventricle.

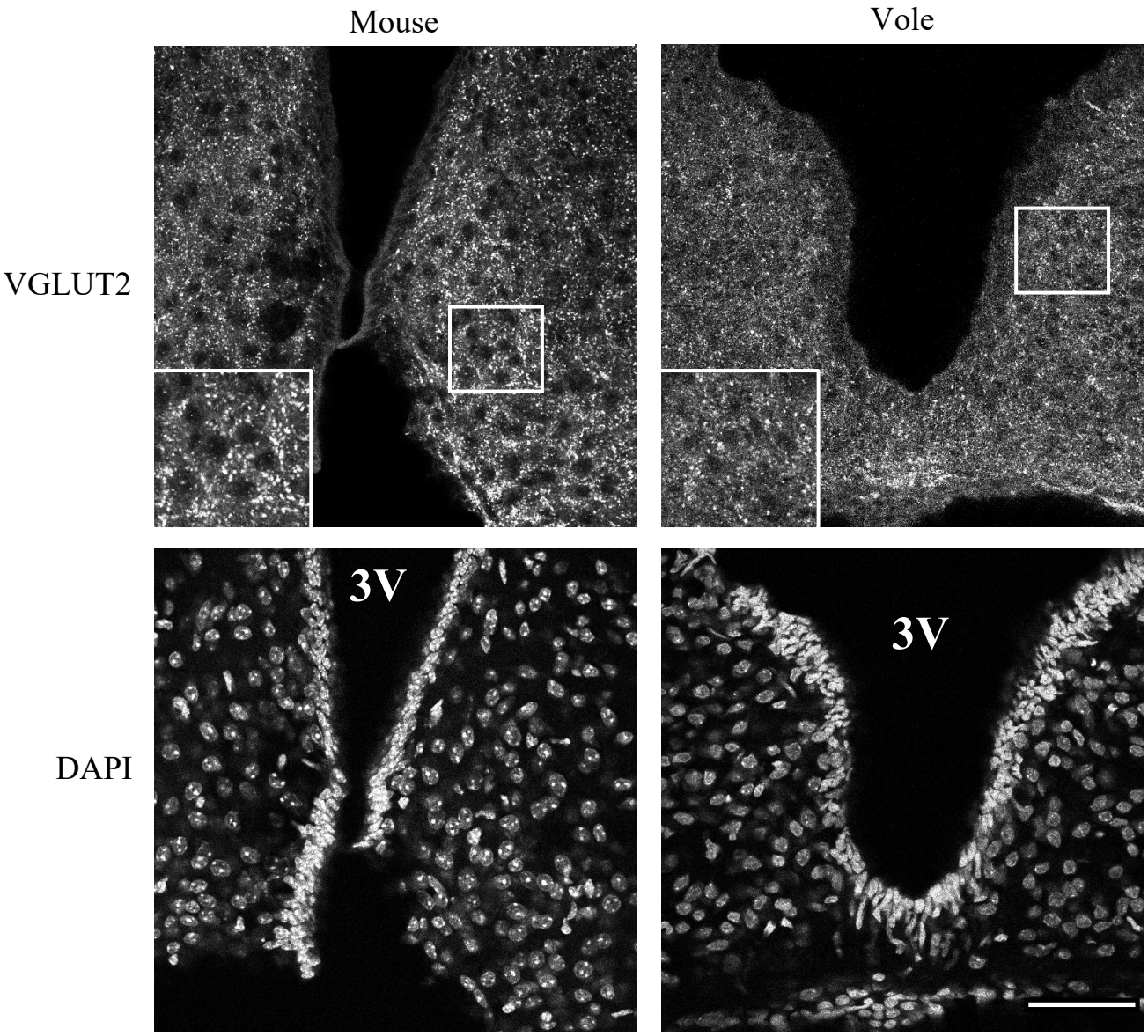

Figure 10: anti-PSD-95 primary antibody with Cy3-conjugated secondary antibody and DAPI counterstain in mouse and vole brain arcuate nucleus tissue. Dilution at 1:500 in mouse and 1:1000 in vole. The scale bar is 50μm in length and images were obtained on a Leica SP-8 microscope with a 40× oil-objective. Insets are magnified two times. 3V = Third ventricle.

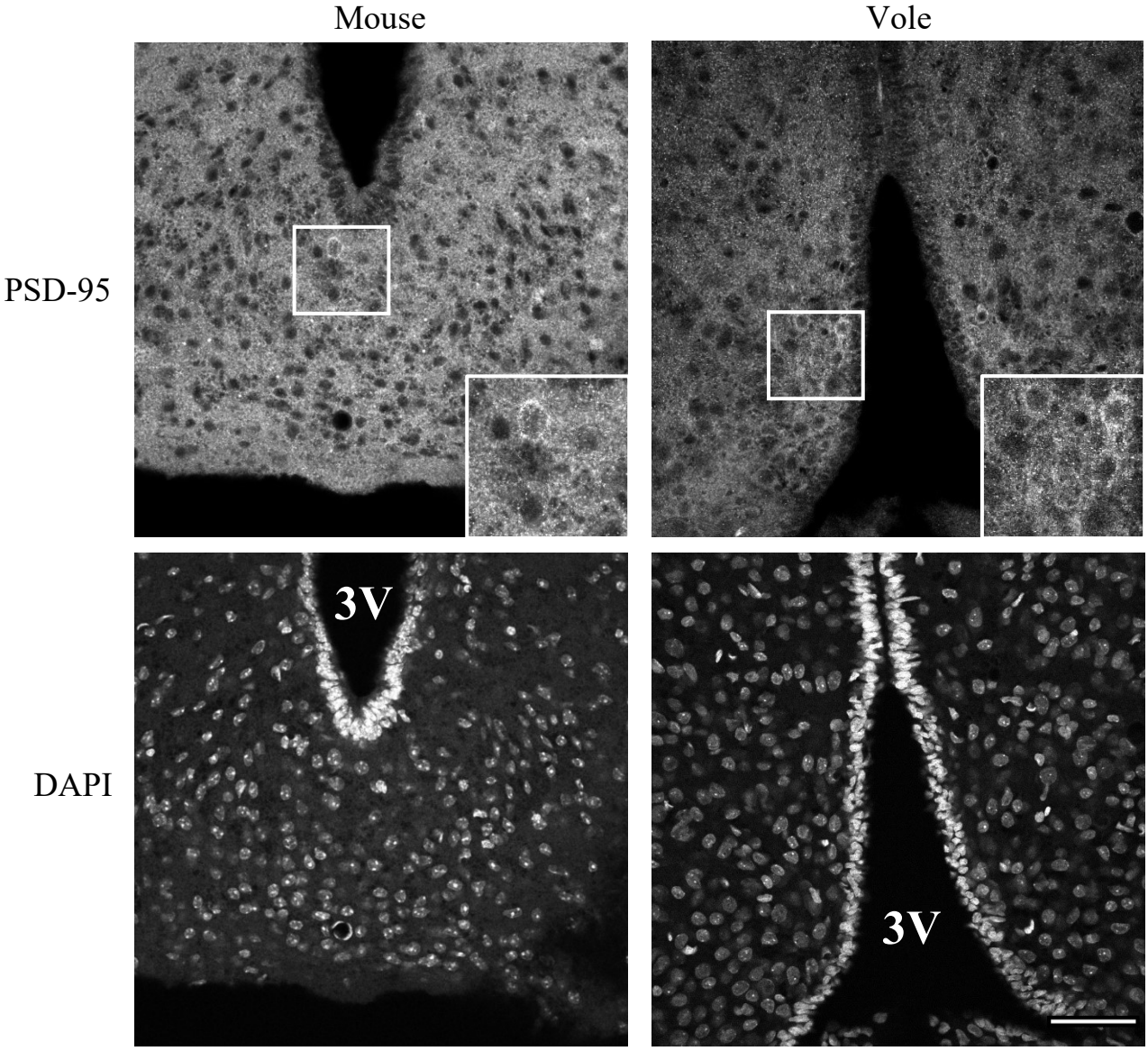

Figure 11: Concentration comparison of anti-PSD-95 primary antibody stains with Cy3-conjugated secondary antibody in mouse and vole brain arcuate nucleus tissue. The scale bar is 50μm in length and images were obtained with a 40× oil-objective on a Leica SP-8 microscope. Insets are magnified two times. At the normal concentration of 1:500, though staining in vole was adequately bright, it was slightly too dense and punctae slightly too large. When reduced to 1:1000, vole tissue more closely matched that of mouse. NB: the staining in this figure for vole 1:1000 is not as bright at it could be, however, note the improvement of punctae size and density.

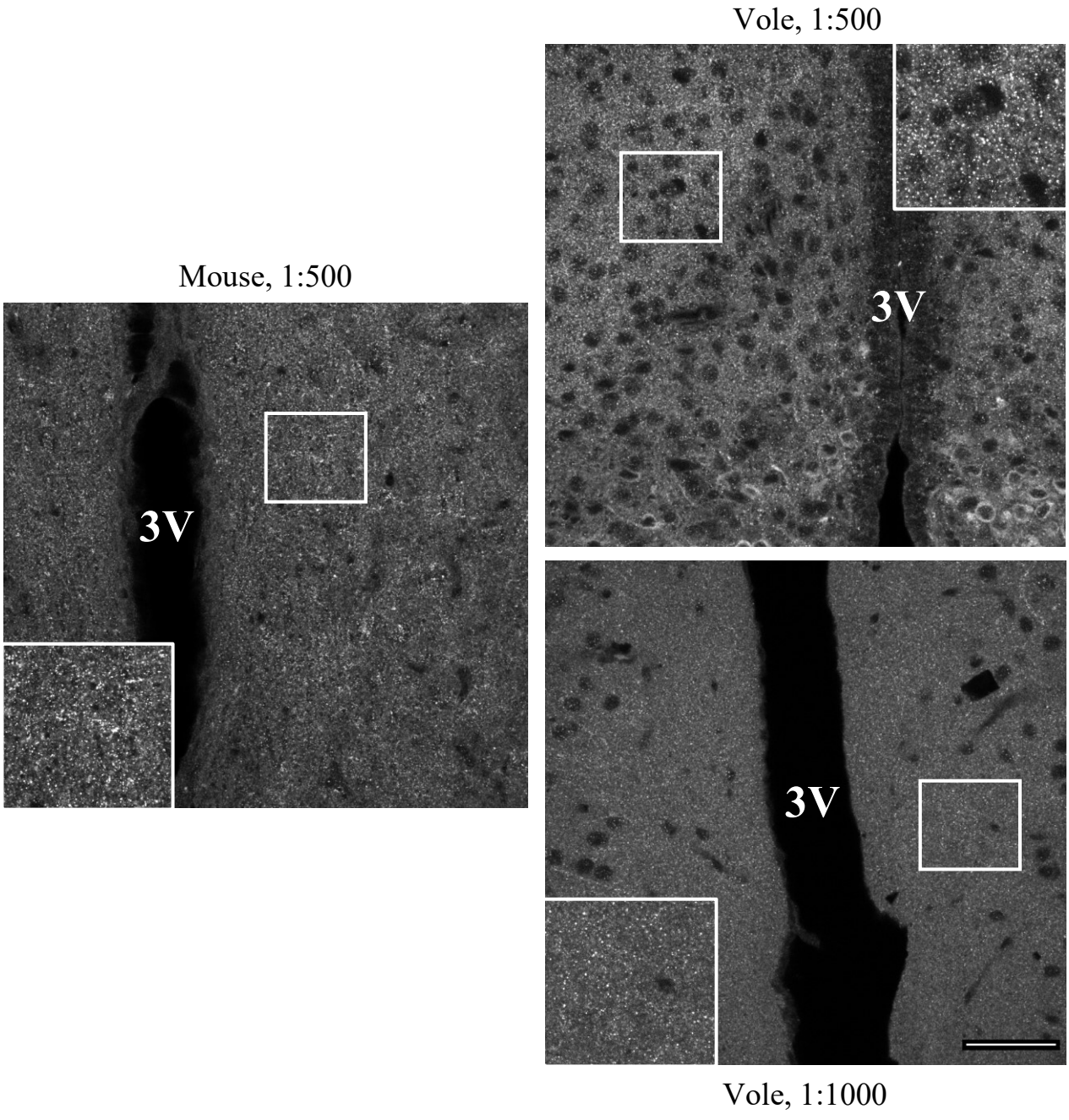

Figure 12: anti-Shank2 primary antibody with Cy3-conjugated secondary antibody and DAPI counterstain in mouse and vole brain arcuate nucleus tissue. Dilution at 1:500 in both species. The scale bar is 50μm in length and images were obtained with a 40× oil-objective on a Leica SP-8 microscope. Insets are magnified two times. 3V = Third ventricle.

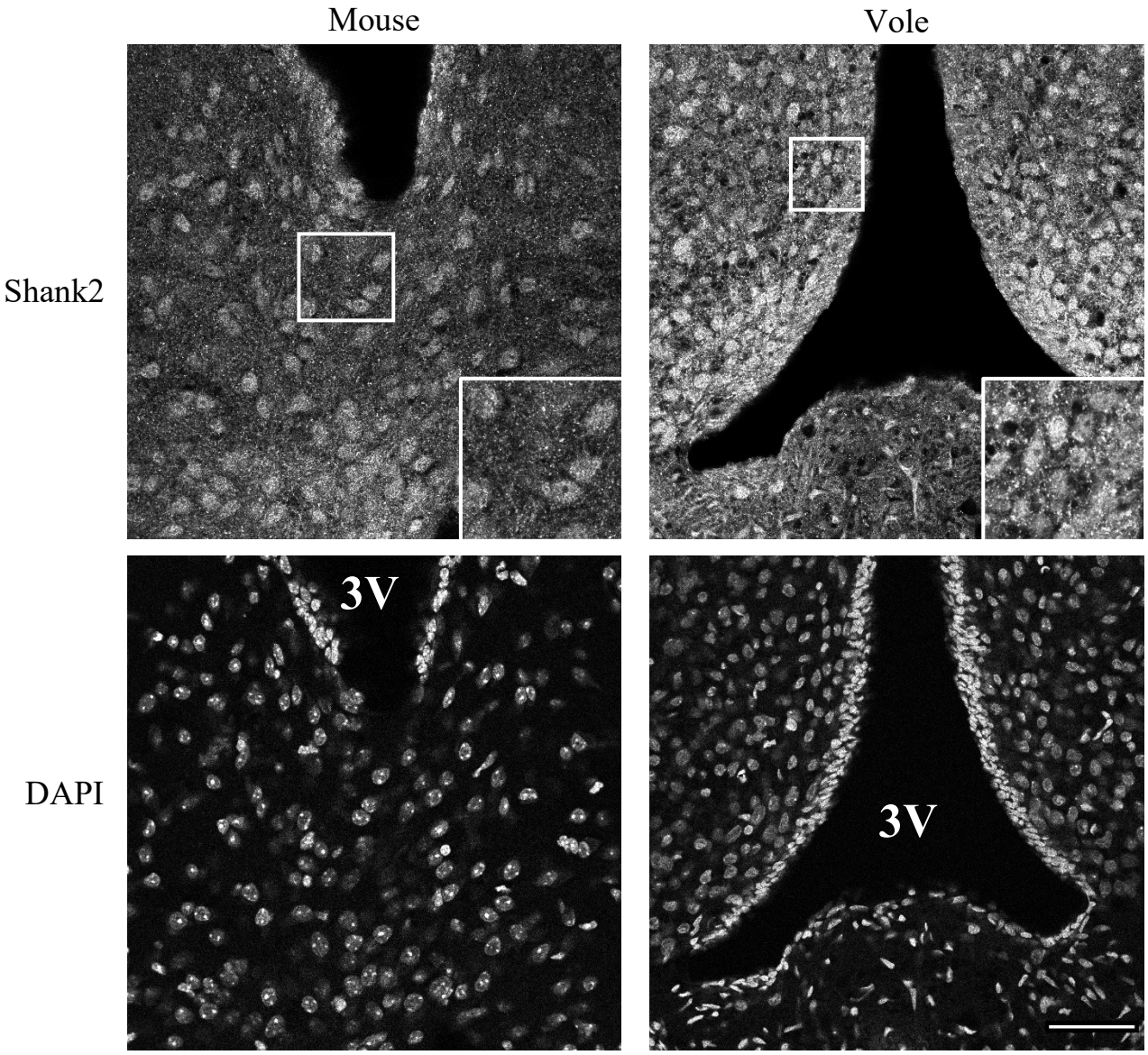

Figure 13: anti-NeuN primary antibody with Cy3-conjugated secondary antibody and DAPI counterstain in mouse and vole brain arcuate nucleus tissue. Dilution at 1:500 in both species. The scale bar is 50μm in length and images were obtained with a 40× oil-objective using a Leica SP-8 microscope. Insets are magnified two times. 3V = Third ventricle. Note that in vole, the ventral aspect of the arcuate nucleus has no staining whatsoever. This is to be expected as there are supposed to be no neural cells there.

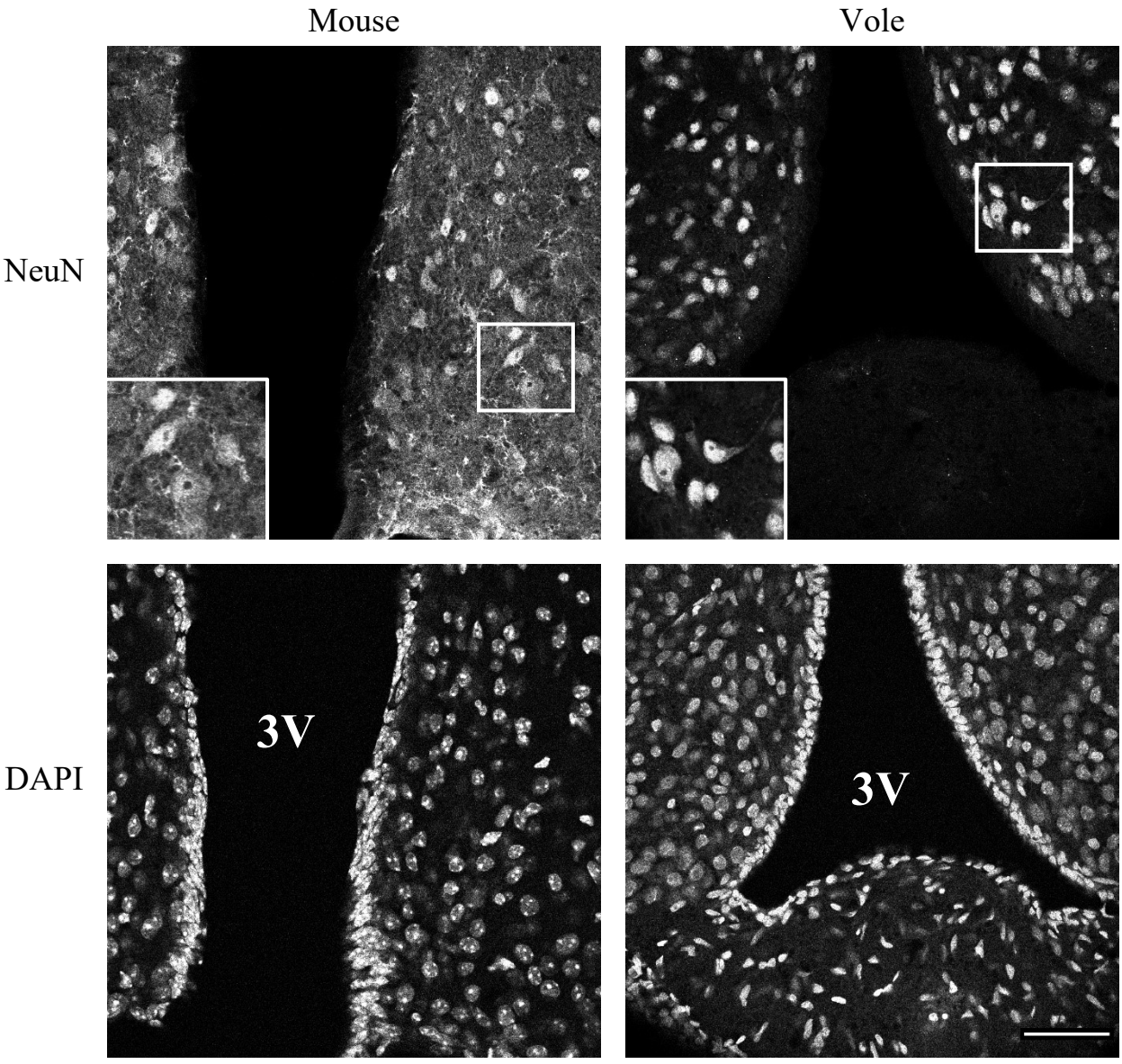

Figure 14: anti-Piccolo primary antibody with Cy3-conjugated secondary antibody and DAPI counterstain in mouse and vole brain arcuate nucleus tissue. Dilution at 1:500 in both species. The scale bar is 50μm in length and images were obtained with a 40× oil-objective on a Leica SP-8 microscope. Insets are magnified two times. 3V = Third ventricle.

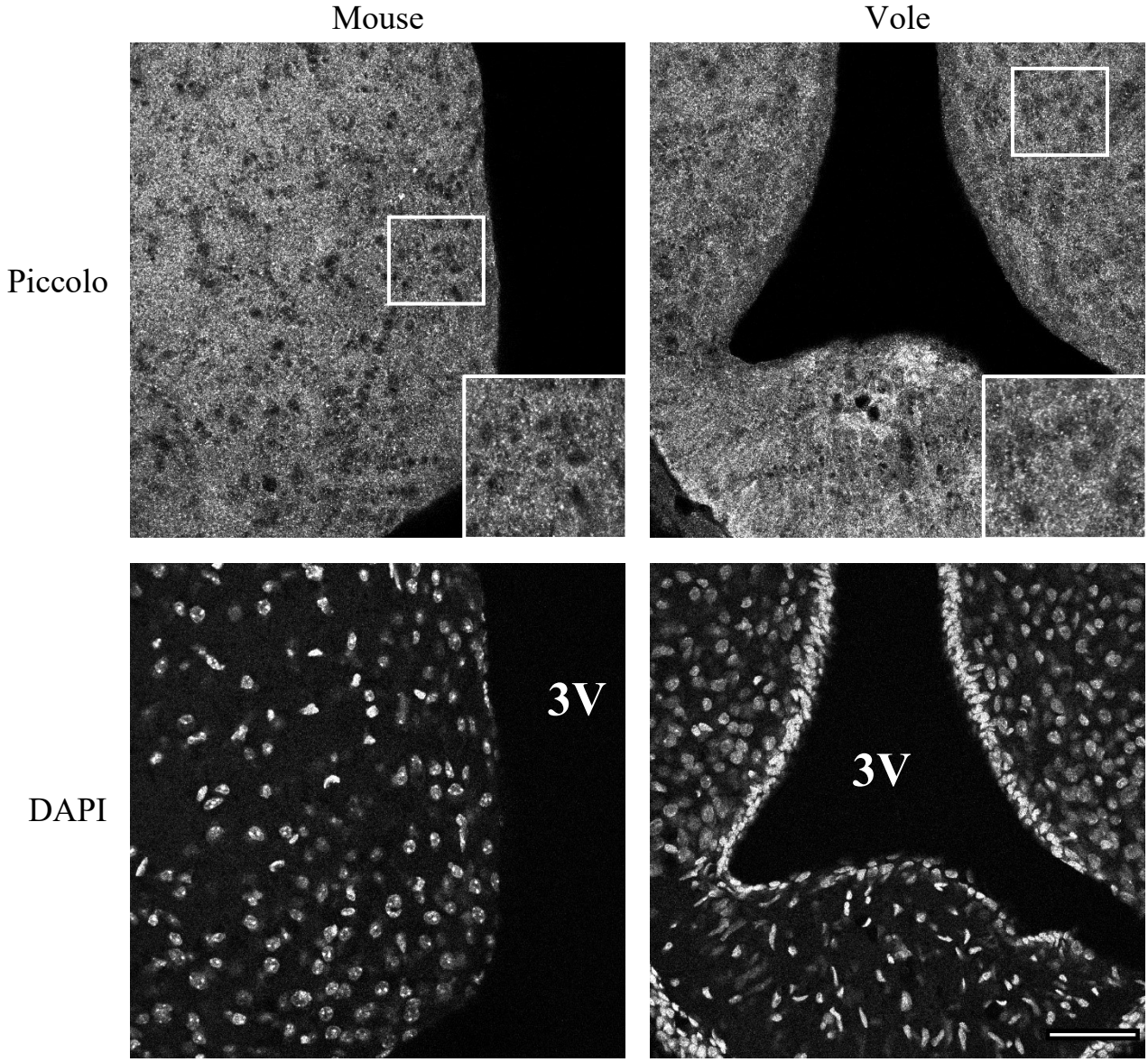

Figure 15: anti-Bassoon primary antibody with Cy3-conjugated secondary antibody and DAPI counterstain in mouse and vole brain arcuate nucleus tissue. Dilution at 1:200 in both species. The scale bar is 50μm in length and images were obtained with a 40× oil-objective on a Leica SP-8 microscope. Insets are magnified two times. 3V = Third ventricle.

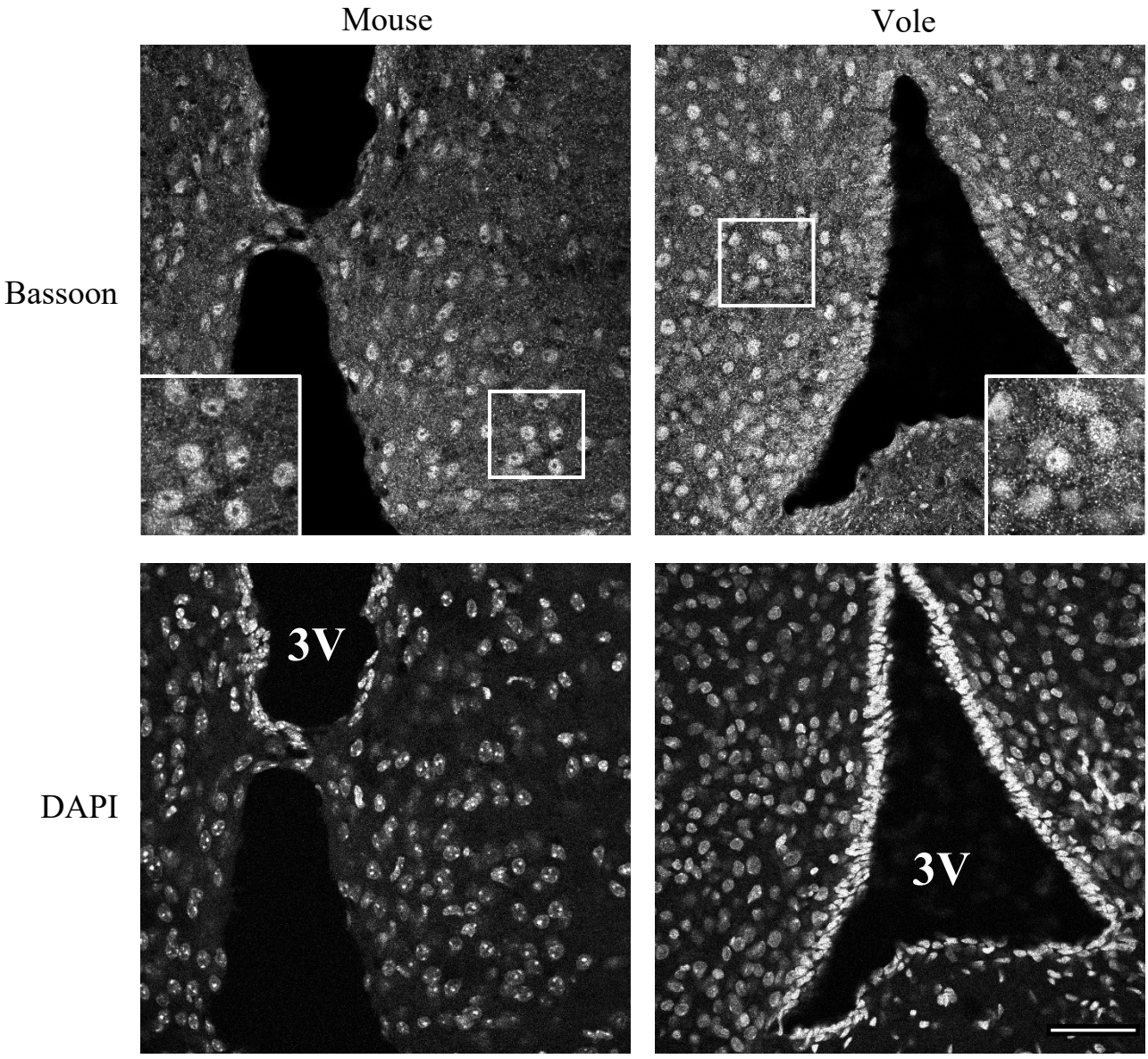

Figure 16: anti-Homer1 primary antibody with Cy3-conjugated secondary antibody and DAPI counterstain in mouse and vole brain arcuate nucleus tissue. Dilution at 1:500 in both species. The scale bar is 50μm in length and images were obtained with a 40× oil-objective on a Leica SP-8 microscope. Insets are magnified two times. 3V = Third ventricle.

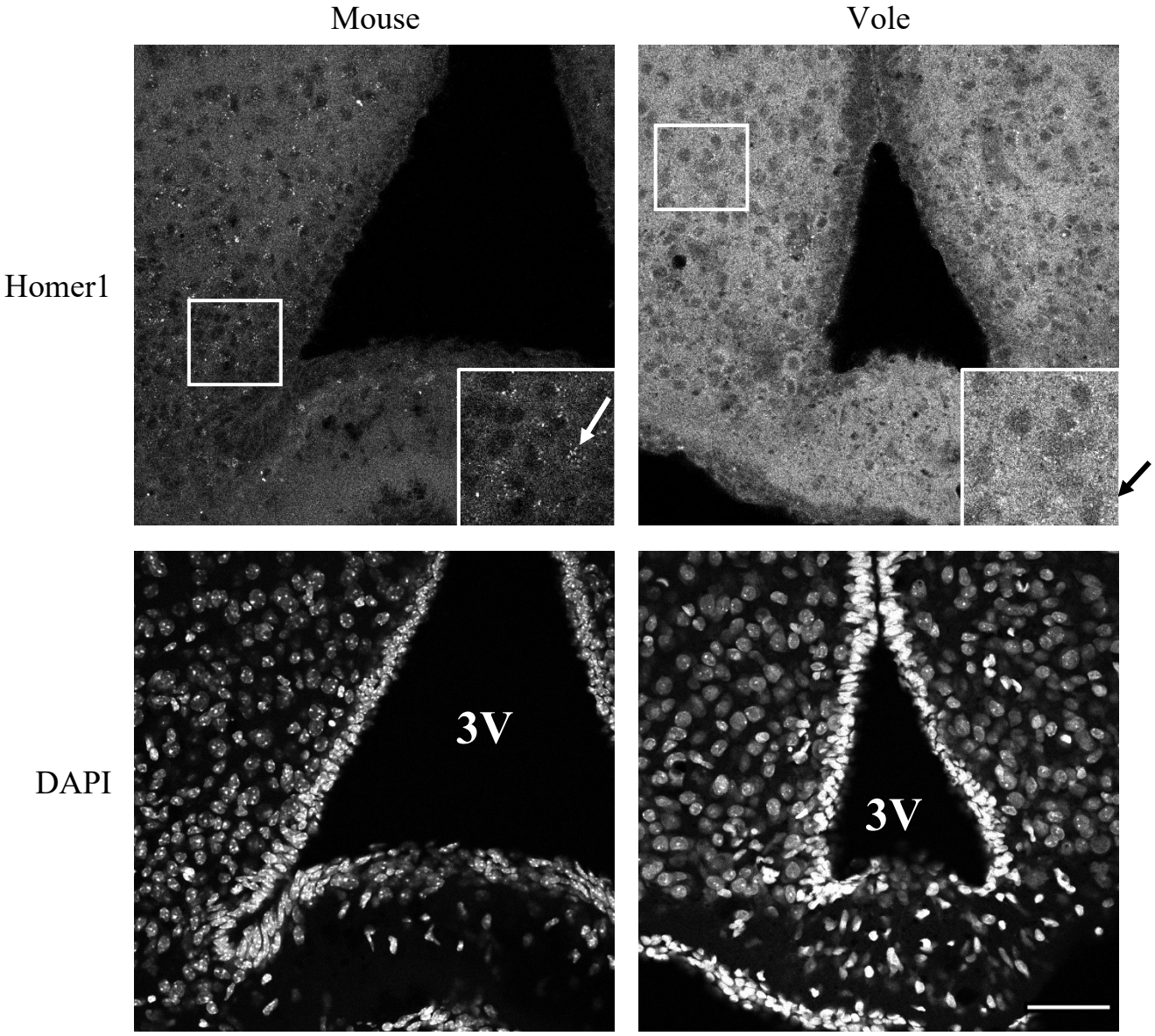

Figure 17: Non-specifically stained cells by the anti-GHRH antibody. All images here are taken just below the lateral ventricle. The scale bar is 50μm in length and images were obtained with a 60× oil-objective on a Nikon E800 microscope. LV = Lateral ventricle. Indicated cells are very distinctive of the typical binding pattern of anti-GHRH antibodies, despite staining in areas of the brain where we expect not to find GHRH. The same phenomenon is found in both vole and mouse. Notice in the secondary control the lack of such faded cells.

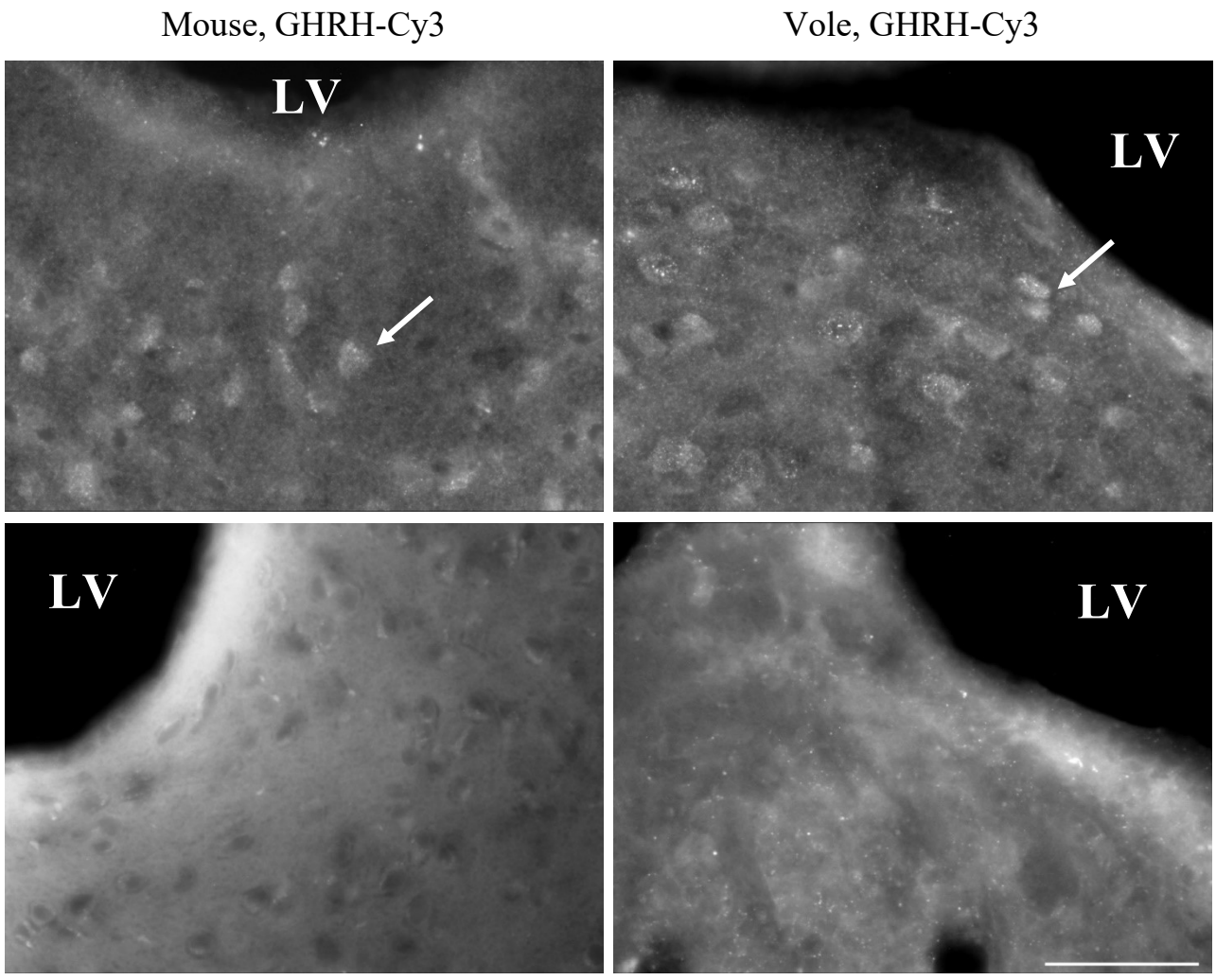

Figure 18: "Granule"-filled tissue in contrast to tissue pre-bleached non-stop in strong light for three days. Nothing has been stained, everything visible is tissue autofluorescence. The scale bar is 50µm in length and images were obtained with a 60× oil-objective on a Nikon E800 microscope. LV = Lateral ventricle. Indicated are representative examples of the "granules" which we believe represent autofluorescent lipofuscin vesicles, visible in all spectra except far-red (i.e., the images below look exactly the same in all spectra except far-red). These granules look remarkably like typical GHRH staining and confound effective counting. As per Sun et al., three-day bleaching almost completely removed these autofluorescent granules [84].

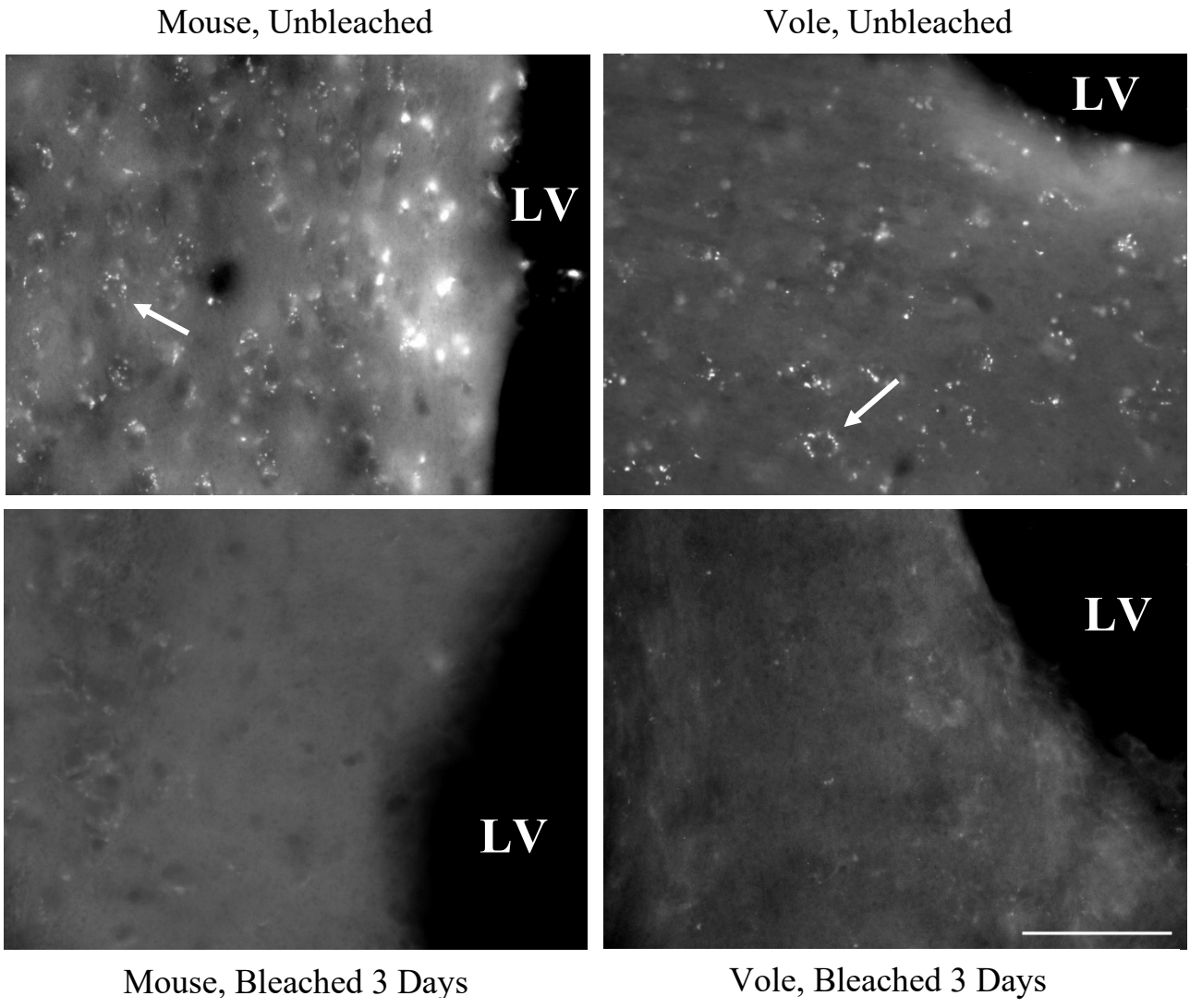

Figure 19: Relationship between sst2+ cell number estimate in arcuate nucleus (ARC) and observed ARC area and volume. Both graphs' display units have been modified to respect space requirements, see along top of each axis. **A.** ***Stereological estimates (estimated population using number weighted section thickness) of sst2-positive cells in the ARC per vole and mouse.*** **B.** ***Comparison of total area in µm² (left) and volume in µm³ (right) of selected region-of-interest (observed ARC) per vole and mouse, as calculated by the Optical Fractionator.***

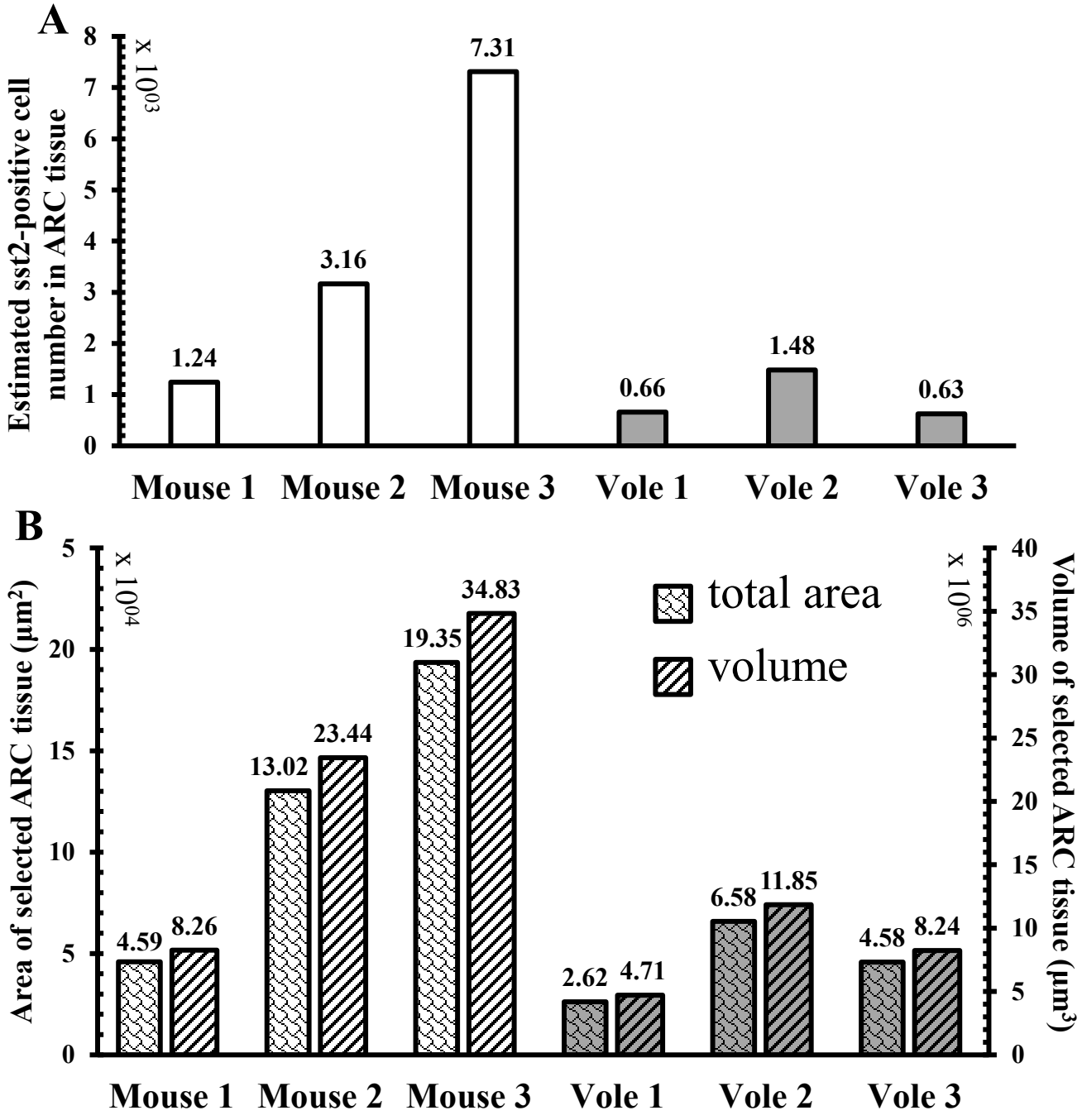

Figure 20. Difference of sst2+ neuron density between vole and mouse. ***A. Non-estimated average marker per frame (i.e., density) per species.*** There is a significant difference ($P \leq 0.05$) between vole and mouse cell density. Average mouse cell count was 2.6 ± 0.29 cells and average vole cell count was 1.8 ± 0.23 cells. Statistical analysis was conducted using a one-tailed student T-test. ***B. Visual representation of density comparison between mouse and vole arcuate nucleus.*** Tissue stained with sst2-Cy3. Scale bar is 50μm in length and images were obtained with a 60× oil-objective on a Nikon E800 microscope. 3V = Third ventricle.

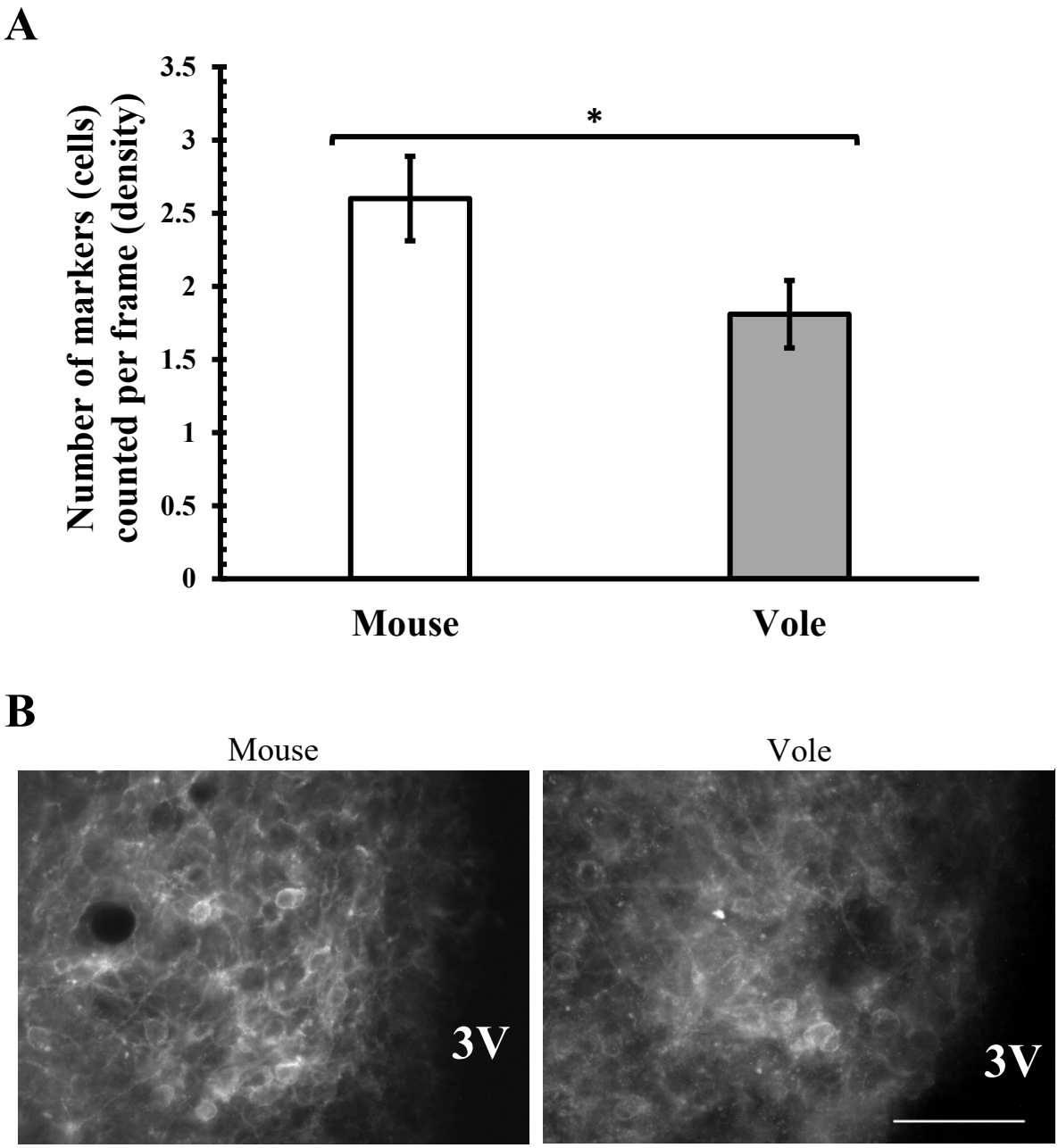

Figure 21: Frozen brain weight difference in grams (g) between mouse and vole. There is a significant difference ($P \leq 0.01$) between the weights of vole and mouse brains. Average mouse brain weighed 0.37 ± 0.007g and average vole brain weighed 0.33 ± 0.01g. Statistical analysis was conducted using a one-tailed student T-test.

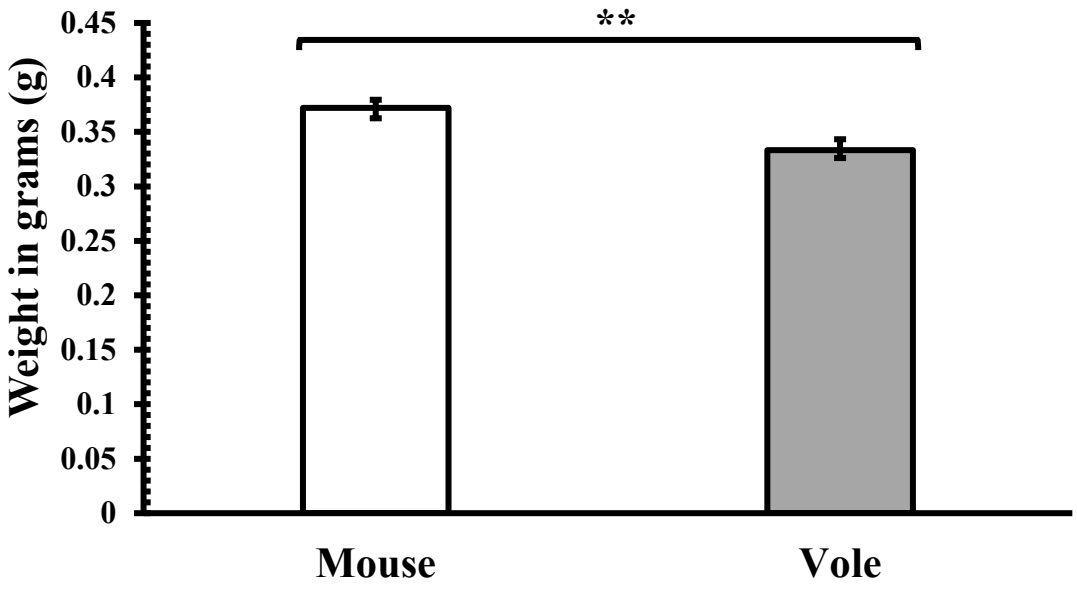

Figure 22: Comparison of arcuate nucleus (ARC) volume in mm^3 between mouse and vole. There is no significant difference between the two species' ARC volumes. Average mouse ARC volume is $0.22 \pm 0.01 mm^3$ and average vole ARC volume is $0.21 \pm 0.03 mm^3$. Statistical analysis was conducted using a two-tailed T-test.

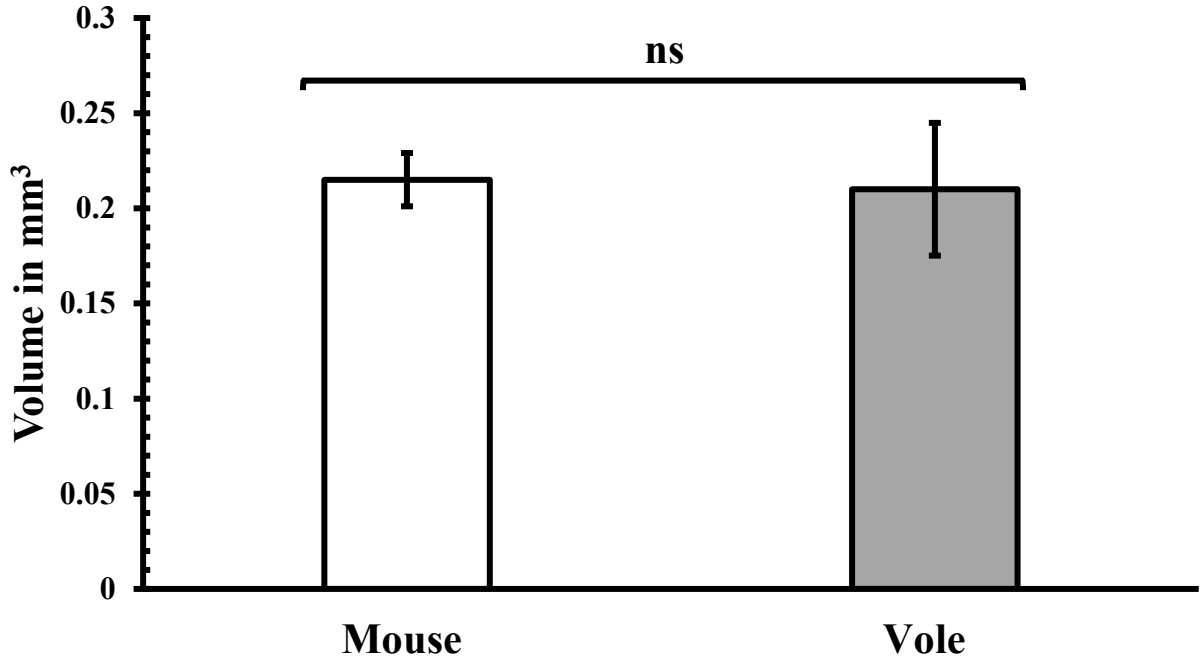

Appendix 1: History and theory of stereology.

Starting in the 1960s, new powerful microscopic innovations, such as improvements in light and electron microscopy as well as the nascent immunocytochemistry, were suddenly resolving cells with better resolution [78]. In 1961 there was the famous Feldberg Meeting which assembled scientists from many disciplines all seeking an answer as to how to quantitatively analyse 3D objects imaged from 2D sections [78] It was here that "stereology" was coined from the Greek for "study of 3D objects" [78]. This meeting was essentially the first congress for what would become the International Society for Stereology, which seeks to find the best way to obtain 3D information from 2D data [78]. At these congresses, biologists discovered that scientists from fields other than biology (such as mathematics or physics) had already come up with interesting techniques to answer this, like Bonaventura Cavalieri who proposed, in 1637, the Cavalieri principle, which states that the volume of an irregularly shaped object could be estimated from the sum of areas on the cut surfaces of the object, or more specifically, that if two objects of the same height have the same cross-sectional area, then they must be of the same volume [78,96].

Until the 1970s however, all forms of stereology used assumption-based sampling methods whereby we force biological objects to fit Euclidean geometrical models such as spheres and lines; models which are inevitably based on false or non-verifiable assumptions (e.g., not all cells are spheres) [78]. When mathematicians specifically began joining the effort, they pointed out the errors in such unverifiable assumptions and proposed unbiased sampling strategies (i.e., probes), stochastic geometry and probability theory as a more solid foundation on which to base our predictions [78]. These theories gradually supplanted the old-fashioned biased stereological models, and the combination of the unbiased geometry probes and sampling allowed us to quantify so-called first order stereological parameters (i.e., number, length, area, and volume) without the need to know anything about the size, shape, or orientation of the objects [78].

Such a breakthrough was revolutionary in the field, but stereology had not yet been accepted by the greater scientific community, which would not come until the 1980s, when stereologists came up with a solution for the most enduring problem of the field dating back to 1925: the Corpuscle Problem [78,79]. The corpuscle problem states that in a given tissue, not all arbitrarily chosen objects have the same size and shape, and, as such, some might be sampled by the sampling probe (i.e., hit by the knife blade) multiple times and others not at all; as such, there

might be a disconnect in the number of existing objects in the tissue and the number of counted objects, which is a serious problem [79]. For a long time, the best answer was the use of "correction factors", formulas that attempt to estimate the parameters of the tissue. For example, we could assume all cells in a group we wish to count are spherical, but the problem comes up: how do we quantify a spherical cell? Is a slightly ovoid cell a sphere? Naturally these correction factors introduce assumptions and bias that are difficult to justify. Unfortunately, correction factors also fail to account for the corpuscle problem. In 1984, however, the Disector Principle was proposed as the solution: it is an unbiased method to estimate the number of objects in a volume, without any assumptions or bias [78,80,81]. The disector is described as two serial sections a known distance apart and on one of these sections (called the lookup section) we superimpose the counting frame [78,80,81]. It is here that we count the tops of objects in consultation with the other, so-called reference, section [78,80,81]. This technique makes use of Gundersen's unbiased counting rules (see in Methods: section 3.6). As such, since we will only count objects seen in the lookup section but not the reference section and due to the use of Gundersen's rules, we will not count objects twice in a stack and we will avoid double-counting objects within the counting frame. Objects, or points, in this technique are called "Q^-" and this is because the points counted are defined as those not appearing in the reference section and are thus "negative" points [77]. Later in 1986, Gundersen improved this technique by creating the Optical Disector [77]. This is the same principle, but rather than serial sections, he proposed using serial optical planes separated by a known distance from within a single thick section [77,78]. Given we used highly complicated statistical equations in our project, I found it useful to understand where these equations come from and why they give us the values we expect. The (optical) disector is defined as such:

$$N = \sum Q^- \bullet \frac{V(\text{ref})}{v(\text{dis})}$$

where V(ref) is the reference volume (i.e., the total volume), and v(dis) is the volume of the disector (or "height • area" of the disector) [77,81]. So, we multiply the counted objects by the reciprocal of the ratio of the total volume used by the disector. In other words, we estimate the number of objects across the section of tissue by accounting for the amount of unused space.

Finally, a further technique called the Fractionator was devised, which eliminates the need for any dimensional data (i.e., information regarding section thickness, distance between sections,

etc.) and does not make any assumptions about section shrinkage, swelling, compression, or about lost caps (cells damaged by the sectioning process, which distorts counts) [77]. In stereology, there is a "General Requirement" which states that "it [must be] possible to unambiguously identify an item from the set(s) of profiles produced by one or more sections through it" [77]. In other words, the researcher must be able to identify what they are looking at. Thus, if the General Requirement is fulfilled, no other spatial information (like shape, size, orientation) is relevant to the sampling of the objects. The fractionator also introduces a statistical efficiency: whereas including every section and counting all objects ($N = \Sigma Q_i^-$) is neither sampling nor time-efficient, we can opt instead for an estimate [77]. According to the fractionator method, "estimating" means that if sections are sampled from the section stack (M) at an arbitrary probability of 1/p, and all objects (Q_i^-) in these sampled sections (m) are counted, we will get an estimate for the total number of objects across the stack (N) [77]. This can be described with the following formula:

$$N = p \bullet \sum^{m} Q_i^-$$

It is noteworthy that the *M and m* variables are effectively missing from the above formula. This is because when the values approach infinity, resulting from infinite repetitions (denoted as "E(x)"), as the following proof demonstrates:

$$E\left(p \bullet \sum^{m} Q_i^-\right) = p \bullet E(m) \bullet E(Q_i^-) = p \bullet \left(\frac{M}{p}\right) \bullet \left(\frac{N}{M}\right) = N$$

where $1 \leq p$ and $0 \leq m \leq M$, we do not need to know either M (total number of sections) or m (number of sampled sections); we need only know p (the sampling probability) [77]. In other words, we need only know the frequency of the sampled sections and the number of counted objects, and thus the resulting number is the estimate accounting for the sections not counted. This principle is essentially the same for other measurements such as volume and length. It was not long before these two principles, the (optical) disector and the fractionator, were combined to make the *optical fractionator estimator* [78].

Since then, stereology has gained acceptance in the greater scientific community and more recent changes to the field comprise the combination of high-resolution microscopes, modern hardware, and user-friendly software into computer systems that generate 1, 2 and 3D probes [78].

Appendix 2: Essential formulas used by stereologists to estimate object number and regional volume [82].

1. **Optical Fractionator Estimator, N**

$$N = \sum \mathrm{Q}^{-} \bullet \frac{t}{h} \bullet \frac{1}{asf} \bullet \frac{1}{ssf}$$

where Q^{-} is the particles counted; t is the section mounted thickness; h is the counting frame height; asf is the Area Sampling Fraction (i.e., counting frame/grid size); and ssf is the Section Sampling Fraction (i.e., interval between sections).

2. **Estimated Volume formula, $\hat{v}$**

$$\hat{v} = A_p m' \bar{t} \left(\sum_{i=1}^{n} P_i \right)$$

where A_p is the area associated with a given point; m′ is the section evaluation interval; $\bar{t}$ is the mean section thickness; and P_i is the number of grid points counted.

3. **Volume associated with a point, V_P (equivalent to "$A_p m' \bar{t}$" in formula 2)**

$$V_p = g^2 m \bar{t}$$

where m is the section evaluation interval; and $\bar{t}$ is the mean section cut thickness.

4. **Area associated with a point, A_p**

$$A_p = g^2$$

where g^2 is the grid area.

5. **Gundersen Coefficient of Error, (Optical Fractionator) CE**

$$CE = \frac{\sqrt{TotalVar}}{s^2}$$

where TotalVar is the Total Variance; and s^2 is the variance due to noise.

6. **Cavalieri Coefficient of error (Cavalieri), CE**

$$CE = \frac{\sqrt{TotalVar}}{\sum_{i=1}^{n} P_i}$$

where n is the number of sections; P_i is the number of points counted on the grid; TotalVar is the total variance of the estimated volume.

7. **Total Variance Gundersen, TotalVar**

$$TotalVar = s^2 + VAR_{SRS}$$

where VAR_{SRS} is the variance due to systematic random sampling (SRS) and s^2 is the variance due to noise.

8. **Variance due to Systematic Random Sampling (SRS) Gundersen, VAR_{SRS}**

$$VAR_{SRS} = \frac{3(A - s^2) - 4B + C}{12}, m = 0$$

$$VAR_{SRS} = \frac{3(A - s^2) - 4B + C}{240}, m = 1$$

where $A = \sum_{i=1}^{n}(Q_i^-)^2$, $B = \sum_{i=1}^{n-1} Q_i^- Q_{i+1}^-$, $C = \sum_{i=1}^{n-2} Q_i^- Q_{i+2}^-$ (optical fractionator) or $A = \sum_{i=1}^{n} P_i^2$, $B = \sum_{i=1}^{n-1} P_i P_{i+1}$, $C = \sum_{i=1}^{n-2} P_i P_{i+2}$ (Cavalieri estimator); m is the smoothness class of the sampled function; n is the number of sections; and s^2 is the variance due to noise.

9. **Variance due to noise, Gundersen (Optical Fractionator), s^2**

$$s^2 = \sum_{i=1}^{n} Q^-$$

where Q^- is the particles counted; and n is the number of sections used.

10. **Variance due to noise, Gundersen (Cavalieri), s^2**

$$s^2 = 0.0724\left(\frac{b}{\sqrt{a}}\right)\sqrt{n\sum_{i=1}^{n} P_i}$$

where $\frac{b}{\sqrt{a}}$ is the shape factor; n is the number of sections; and P_i is the number of points counted on the grid. The shape factor can be understood as $\frac{boundary}{\sqrt{area}}$, with boundary meaning more or less the perimeter of the region. In other words, if the boundary of the region is large and the region's area is small (i.e., a very convoluted shape with many branches), the shape factor weighs heavily in the formula. Conversely, if the boundary is small with a large area (a simple shape like a circle), then the shape factor's effect is negligible. In our case, the ARC is a comparatively simple shape and as such has a comparatively small shape factor.

References

1. Olarescu, N.C., Gunawardane, K., Hansen, T.K., et al. Normal physiology of growth hormone in adults. [Last update 2019 Oct 16]. In Feingold, K.R., Anawalt, B., Boyce, A., et al. (eds). Endotext [Internet]. South Dartmouth (MA): *MDText.com, Inc*.; 2000-. Available from: https://www.ncbi.nlm.nih.gov/books/NBK279056/

2. Bowen, R. Growth hormone (somatotropin). [updated 2021]. Retrieved from http://www.vivo.colostate.edu/hbooks/pathphys/endocrine/hypopit/gh.html

3. Gupta V. (2011). Adult growth hormone deficiency. *Indian Journal of Endocrinology and Metabolism*, 15(Suppl3), S197-S202. https://doi.org/10.4103/2230-8210.84865

4. Ayuk, J. (2006). Growth hormone and its disorders. *Postgraduate Medical Journal*, 82(963), 24-30. https://doi.org/10.1136/pgmj.2005.036087

5. Laron, Z. (2001). Insulin-like growth factor 1 (IGF-1): a growth hormone. *Molecular Pathology*, 54(5), 311-316. https://doi.org/10.1136/mp.54.5.311

6. Kim, S.-H., & Park, M.-J. (2017). Effects of growth hormone on glucose metabolism and insulin resistance in human. *Annals of Pediatric Endocrinology & Metabolism*, 22(3), 145-152. https://doi.org/10.6065/apem.2017.22.3.145

7. Møller, N., & Jørgensen, J. O. L. (2009). Effects of growth hormone on glucose, lipid, and protein metabolism in human subjects. *Endocrine Reviews*, 30(2), 152-177. https://doi.org/10.1210/er.2008-0027

8. Kokka, N., Garcia, J. F., George, R., & Elliott, H. W. (1972). Growth hormone and ACTH secretion: evidence for an inverse relationship in rats. *Endocrinology*, 90(3), 735-743. https://doi.org/10.1210/endo-90-3-735

9. Jaffe, C. A., Ocampo-Lim, B., Guo, W., Krueger, K., Sugahara, I., Demott-Friberg, R., Bermann, M., & Barkan, A. L. (1998). Regulatory mechanisms of growth hormone secretion are sexually dimorphic. *Journal of Clinical Investigation*, 102(1), 153-164. https://doi.org/10.1172/jci2908

10. Tannenbaum, G.S. and Epelbaum, J. (2011). Somatostatin. In *Comprehensive Physiology*, R. Terjung (Ed.). https://doi.org/10.1002/cphy.cp070509

11. Helboe, L., Hay-Schmidt, A., Stidsen, C. E., & Møller, M. (1999). Immunohistochemical localization of the somatostatin receptor subtype 2 (sst2) in the central nervous system of the golden hamster (Mesocricetus auratus). *Journal of Comparative Neurology*, 405(2), 247-261. https://doi.org/10.1002/(SICI)1096-9861(19990308)405:2<247::AID-CNE8>3.0.CO;2-V

12. Dournaud, P., Gu, Y. Z., Schonbrunn, A., Mazella, J., Tannenbaum, G. S., & Beaudet, A. (1996). Localization of the somatostatin receptor SST2A in rat brain using a specific anti-peptide antibody. *The Journal of Neuroscience*, 16(14), 4468-4478. https://doi.org/10.1523/JNEUROSCI.16-14-04468.1996

13. Osterstock, G., Escobar, P., Mitutsova, V., Gouty-Colomer, L.-A., Fontanaud, P., Molino, F., Fehrentz, J.-A., Carmignac, D., Martinez, J., Guerineau, N. C., Robinson, I. C. A. F., Mollard, P., & Méry, P.-F. (2010). Ghrelin stimulation of growth hormone-releasing hormone neurons is direct in the arcuate nucleus. *PLOS One*, 5(2), e9159. https://doi.org/10.1371/journal.pone.0009159

14. Tannenbaum, G. S., & Martin, J. B. (1976). Evidence for an endogenous ultradian rhythm governing growth hormone secretion in the rat. *Endocrinology*, 98(3), 562-570. https://doi.org/10.1210/endo-98-3-562

15. Terry, L. C., Saunders, A., Audet, J., Willoughby, J. O., Brazeau, P., & Martin, J. B. (1977). Physiologic secretion of growth hormone and prolactin in male and female rats. *Clinical Endocrinology (Oxford),* Suppl 6, 19s-28s. https://doi.org/10.1111/j.1365-2265.1977.tb03335.x

16. Macleod, J. N., Pampori, N. A., & Shapiro, B. H. (1991). Sex differences in the ultradian pattern of plasma growth hormone concentrations in mice. *Journal of Endocrinology*, 131(3), 395-399. https://doi.org/10.1677/joe.0.1310395

17. Osterstock, G., Mitutsova, V., Barre, A., Granier, M., Fontanaud, P., Chazalon, M., Carmignac, D., Robinson, I. C. A. F., Low, M. J., Plesnila, N., Hodson, D. J., Mollard, P., & Méry, P.-F. (2016). Somatostatin triggers rhythmic electrical firing in hypothalamic GHRH neurons. *Scientific Reports*, 6(1), 24394. https://doi.org/10.1038/srep24394

18. Stroh, T., van Schouwenburg, M. R., Beaudet, A., & Tannenbaum, G. S. (2009). Subcellular dynamics of somatostatin receptor subtype 1 in the rat arcuate nucleus: receptor localization and synaptic connectivity vary in parallel with the ultradian rhythm of growth hormone secretion. *The Journal of Neuroscience*, 29(25), 8198-8205. https://doi.org/10.1523/JNEUROSCI.0336-09.2009

19. Theodosis, D. T. (2002). Oxytocin-secreting neurons: a physiological model of morphological neuronal and glial plasticity in the adult hypothalamus. *Frontiers in Neuroendocrinology*, 23(1), 101-135. https://doi.org/10.1006/frne.2001.0226

20. Theodosis, D. T., Piet, R., Poulain, D. A., & Oliet, S. H. R. (2004). Neuronal, glial and synaptic remodeling in the adult hypothalamus: functional consequences and role of cell surface and extracellular matrix adhesion molecules. *Neurochemistry International*, 45(4), 491-501. https://doi.org/10.1016/j.neuint.2003.11.003

21. Theodosis, D. T., Poulain, D. A., & Oliet, S. H. R. (2008). Activity-dependent structural and functional plasticity of astrocyte-neuron interactions. *Physiological Reviews*, 88(3), 983-1008. https://doi.org/10.1152/physrev.00036.2007

22. Bednarz, K. (2019). *Changes in synaptic connectivity during ultradian growth hormone secretion are correlated with changes in astrocytic coverage of neurons as seen in super-resolution and electron microscopy* [master's thesis, McGill University]. eScholarship@McGill. https://escholarship.mcgill.ca/concern/theses/3r075045s

23. Bednarz, K., Alshafie, W., Aufmkolk, S., Desserteaux, T., Markam, P. S., Storch, K.-F., & Stroh, T. (2020). Ultradian secretion of growth hormone in mice: linking physiology with changes in synapse parameters using super-resolution microscopy. *Frontiers in Neural Circuits*, 14. https://doi.org/10.3389/fncir.2020.00021

24. Krogh, A. (1929). The progress of physiology. *American Journal of Physiology-Legacy Content*, 90(2), 243-251. https://doi.org/10.1152/ajplegacy.1929.90.2.243

25. Matthews, B. J., & Vosshall, L. B. (2020). How to turn an organism into a model organism in 10 'easy' steps. *The Journal of Experimental Biology*, 223(Suppl 1), jeb218198. https://doi.org/10.1242/jeb.218198

26. Green, S., Dietrich, M. R., Leonelli, S., & Ankeny, R. A. (2018). 'Extreme' organisms and the problem of generalization: interpreting the Krogh principle. *History and Philosophy of the Life Sciences*, 40(4). https://doi.org/10.1007/s40656-018-0231-0

27. Folkertsma, R., Westbury, M. V., Eccard, J. A., & Hofreiter, M. (2018). The complete mitochondrial genome of the common vole, Microtus arvalis (Rodentia: Arvicolinae). *Mitochondrial DNA Part B: Resources*, 3(1), 446-447. https://doi.org/10.1080/23802359.2018.1457994

28. Nowak, R. M. (1999). *Walker's mammals of the world*. Johns Hopkins University Press.

29. Donnelly, T. M., & Quimby, F. W. (2002). Chapter 7 - Biology and diseases of other rodents. In J. G. Fox, L. C. Anderson, F. M. Loew, & F. W. Quimby (Eds.) *Laboratory Animal Medicine* (Second Edition) (pp. 247-307). Academic Press. https://doi.org/10.1016/B978-0-12-263620-2.50013-6

30. De Vienne, D. M. (2016). Lifemap: exploring the entire tree of life. *PLOS Biology*, 14(12), e2001624. https://doi.org/10.1371/journal.pbio.2001624. See also: https://lifemap-ncbi.univ-lyon1.fr/, retrieved July 24, 2023.

31. Hansson, L. (1977). Spatial dynamics of field voles Microtus agrestis in heterogeneous landscapes. *Oikos*, 29(3), 539-544. https://doi.org/10.2307/3543592

32. Lidicker, W. Z. (2015). Genetic and spatial structuring of the California vole (Microtus californicus) through a multiannual density peak and decline. *Journal of Mammalogy*, 96(6), 1142-1151. https://doi.org/10.1093/jmammal/gyv122

33. Bronson, F. H., & De La Rosa, J. (1994). Tonic-clonic convulsions in meadow voles. *Physiology & Behavior*, 56(4), 683-685. https://doi.org/10.1016/0031-9384(94)90227-5

34. Getz, L. L., Carter, C. S., & Gavish, L. (1981). The mating system of the prairie vole, Microtus ochrogaster: Field and laboratory evidence for pair-bonding. *Behavioral Ecology and Sociobiology*, 8(3), 189-194. https://doi.org/10.1007/bf00299829

35. Gruder-Adams, S., & Getz, L. L. (1985). Comparison of the mating system and paternal behavior in Microtus ochrogaster and M. pennsylvanicus. *Journal of Mammalogy*, 66(1), 165-167. https://doi.org/10.2307/1380976

36. Hall, J. E., Seed, J. R., & Sechelski, J. B. (1985). Multiple alpha-keto aciduria in Microtus montanus chronically infected with Trypanosoma brucei gambiense. *Comparative Biochemistry and Physiology Part B*, 82(1), 73-78. https://doi.org/10.1016/0305-0491(85)90130-0

37. Dieterich, R. A., & Preston, D. J. (1979). Atherosclerosis in lemmings and voles fed a high fat, high cholesterol diet. *Atherosclerosis*, 33(2), 181-189. https://doi.org/10.1016/0021-9150(79)90115-1

38. Sasaki, M., Arai, T., Machida, Y., & Oki, Y. (1989). Diabetic syndrome induced by monosodium aspartate administration in Microtus arvalis Pallas. *The Japanese Journal of Veterinary Science*, 51(4), 669-675. https://doi.org/10.1292/jvms1939.51.669

39. Arai, T., & Oki, Y. (1983). Sōshoku-sei hatanezumi (Microtus arvalis parasu) ni okeru shokuji-sei tōnyō-byō no yūhatsu to sono hasseikijo [Induction of dietetic diabetes in Microtus arvalis Pallas and its developmental mechanism]. *Jikken Dobutsu Experimental Animals*, 32(4), 191-200. https://doi.org/10.1538/expanim1978.32.4_191

40. Kudo, H., & Oki, Y. (1984). Microtus species as new herbivorous laboratory animals: reproduction; bacterial flora and fermentation in the digestive tracts; and nutritional physiology. *Veterinary Research Communications*, 8(1), 77-91. https://doi.org/10.1007/bf02214700

41. Zima, J., Macholán, M., Míšek, I., & Sterba, O. (2008). Sex chromosome abnormalities in natural populations of the common vole (Microtus arvalis). *Hereditas*, 117(3), 203-207. https://doi.org/10.1111/j.1601-5223.1992.tb00015.x

42. Noble, S. (2017). *Microtus Arvalis common vole*. Animal Diversity Web, Museum of Zoology, University of Michigan. Retrieved July 24, 2023, https://animaldiversity.org/accounts/Microtus_arvalis/

43. van Dalum, M. J. (2022). *Evolution of seasonal adaptations in voles.* [Doctoral Dissertation, The Arctic University of Norway]. UiT Munin. https://hdl.handle.net/10037/24919

44. Frank, F. (1954). Die kausalität der nagetier-zyklen im lichte neuer populationsdynamischer-untersuchungen an deutschen microtinen (ein zwischenbericht) [The causality of rodent cycles in light of new population dynamic studies on German microtines (an interim report)], Germany, *Zeitschrift für Morphologie und Ökologie der Tiere*, 43(4), 321-356. https://doi.org/10.1007/BF00404878

45. Jokić, G., & Blažić, T. (2021). Control of common vole (Microtus arvalis) in alfalfa crops using reduced content of anticoagulants. *Agronomy*, 12(1), 53. https://doi.org/10.3390/agronomy12010053

46. Vadász, C. (1974). Seasonal changes in pituitary prolactin and growth hormone content of field voles in different reproductive states (Microtus arvalis Pall., Rodentia). *Acta biologica Academiae Scientarium Hungaricae*, 25(3), 227-229.

47. Martinet, L., & Meunier, M. (1975). Plasma and pituitary levels of LH in field voles, Microtus arvalis, reared under two different photoperiods. *Journal of Physiology (Paris)*, 70, 539-547.

48. Daan, S., & Slopsema, S. (1978). Short-term rhythms in foraging behaviour of the common vole, Microtus arvalis. *Journal of Comparative Physiology*, 127(3), 215-227. https://doi.org/10.1007/BF01350112

49. Lehmann, U., & Sommersberg, C. W. (1980). Activity patterns of the common vole, Microtus arvalis — automatic recording of behaviour in an enclosure. *Oecologia*, 47(1), 61-75. https://doi.org/10.1007/BF00541777

50. Gerkema, M. P., & Verhulst, S. (1990). Warning against an unseen predator: a functional aspect of synchronous feeding in the common vole, Microtus arvalis. *Animal Behaviour*, 40(6), 1169-1178. https://doi.org/10.1016/S0003-3472(05)80183-6

51. Gerkema, M. P., Groos, G. A., & Daan, S. (1990). Differential elimination of circadian and ultradian rhythmicity by hypothalamic lesions in the common vole, Microtus arvalis. *Journal of Biological Rhythms*, 5(2), 81-95. https://doi.org/10.1177/074873049000500201

52. Geisel, T.S. (1962). *The sleep book*. In (p.32-33) Random House. ISBN:978-0-394-80091-2

53. Gerkema, M. P., & van der Leest, F. (1991). Ongoing ultradian activity rhythms in the common vole, Microtus arvalis, during deprivations of food, water and rest. *Journal of Comparative Physiology A*, 168(5), 591-597. https://doi.org/10.1007/BF00215081

54. Gerkema, M. P., Daan, S., Wilbrink, M., Hop, M. W., & van der Leest, F. (1993). Phase control of ultradian feeding rhythms in the common vole (Microtus arvalis): the roles of light and the circadian system. *Journal of Biological Rhythms*, 8(2), 151-171. https://doi.org/10.1177/074873049300800205

55. Veen, D. R. v. d., van der Pol-Meijer, M. M. T., Jansen, K., Smeets, M., Zee, E. A. v. d., & Gerkema, M. P. (2008). Circadian rhythms of C-FOS expression in the suprachiasmatic nuclei of the common vole (Microtus arvalis). *Chronobiology International*, 25(4), 481-499. https://doi.org/10.1080/07420520802254403

56. Bourguignon, C., & Storch, K.-F. (2017). Control of rest:activity by a dopaminergic ultradian oscillator and the circadian clock. *Frontiers in Neurology*, 8, 614-614. https://doi.org/10.3389/fneur.2017.00614

57. Blum, I. D., Zhu, L., Moquin, L., Kokoeva, M. V., Gratton, A., Giros, B., & Storch, K.-F. (2014). A highly tunable dopaminergic oscillator generates ultradian rhythms of behavioral arousal. *eLife*, 3. https://doi.org/10.7554/elife.05105

58. Honma, K.-I., Honma, S., & Hiroshige, T. (1987). Activity rhythms in the circadian domain appear in suprachiasmatic nuclei lesioned rats given methamphetamine. *Physiology & Behavior*, 40(6), 767-774. https://doi.org/10.1016/0031-9384(87)90281-2

59. Honma, S., & Honma, K.-I. (1995). Phase-dependent phase shift of methamphetamine-induced circadian rhythm by haloperidol in SCN-lesioned rats. *Brain Research*, 674(2), 283-290. https://doi.org/10.1016/0006-8993(95)00027-n

60. Millard, W. J., Reppert, S. M., Sagar, S. M., & Martin, J. B. (1981). Light-dark entrainment of the growth hormone ultradian rhythm in the rat is mediated by the arcuate nucleus. *Endocrinology*, 108(6), 2394-2396. https://doi.org/10.1210/endo-108-6-2394

61. Danielson, E., & Lee, S. H. (2014). SynPAnal: software for rapid quantification of the density and intensity of protein puncta from fluorescence microscopy images of neurons. *PLoS ONE*, 9(12), e115298. https://doi.org/10.1371/journal.pone.0115298

62. Dalva, M. B., McClelland, A. C., & Kayser, M. S. (2007). Cell adhesion molecules: signalling functions at the synapse. *Nature Reviews Neuroscience*, 8(3), 206-220. https://doi.org/10.1038/nrn2075

63. M Moreno Manrique, J. F., Voit, P. R., Windsor, K. E., Karla, A. R., Rodriguez, S. R., & Beaudoin, G. M. J., 3rd. (2021). SynapseJ: an automated, synapse identification macro for ImageJ. *Front Neural Circuits*, 15, 731333. https://doi.org/10.3389/fncir.2021.731333

64. Leung, Y. Y., Yao Hui, L. L., & Kraus, V. B. (2015). Colchicine – update on mechanisms of action and therapeutic uses. *Seminars in Arthritis and Rheumatism*, 45(3), 341-350. https://doi.org/10.1016/j.semarthrit.2015.06.013

65. UniProt Knowledgebase. (n.d.). *Q9H598 · VIAAT_HUMAN*. Retrieved July 24, 2023, from: https://www.uniprot.org/uniprotkb/Q9H598/entry

66. National Library of Medicine (US), National Center for Biotechnology Information. [Last update July 9, 2023]. *GPHN gephyrin [Homo sapiens (human)]*. https://www.ncbi.nlm.nih.gov/gene/10243

67. UniProt Knowledgebase. (n.d.). *Q9NQX3 · GEPH_HUMAN*. Retrieved July 24, 2023, from: https://www.uniprot.org/uniprotkb/Q9NQX3/entry

68. UniProt Knowledgebase. (n.d.). *Q9P2U8 · VGLU2_HUMAN*. Retrieved July 24, 2023, from: https://www.uniprot.org/uniprotkb/Q9P2U8/entry

69. National Library of Medicine (US), National Center for Biotechnology Information. [Last update July 9, 2023]. *DLG4 discs large MAGUK scaffold protein 4 [Homo sapiens (human)]*. https://www.ncbi.nlm.nih.gov/gene/1742

70. UniProt Knowledgebase. (n.d.). *P78352 · DLG4_HUMAN*. Retrieved July 24, 2023, from: https://www.uniprot.org/uniprotkb/P78352/entry

71. UniProt Knowledgebase. (n.d.). *Q9UPX8 · SHAN2_HUMAN*. Retrieved July 24, 2023, from: https://www.uniprot.org/uniprotkb/Q9UPX8/entry

72. UniProt Knowledgebase. (n.d). *A6NFN3 · RFOX3_HUMAN*. Retrieved July 24, 2023, from: https://www.uniprot.org/uniprotkb/A6NFN3/entry

73. National Library of Medicine (US), National Center for Biotechnology Information. [Last update July 9, 2023]. *RBFOX3 RNA binding fox-1 homolog 3 [Homo sapiens (human)]*. https://www.ncbi.nlm.nih.gov/gene/146713

74. UniProt Knowledgebase. (n.d.). *Q9Y6V0 · PCLO_HUMAN*. Retrieved July 24, 2023, from https://www.uniprot.org/uniprotkb/Q9Y6V0/entry

75. UniProt Knowledgebase. (n.d.). *Q9UPA5 · BSN_HUMAN*. Retrieved July 24, 2023, from: https://www.uniprot.org/uniprotkb/Q9UPA5/entry

76. UniProt Knowledgebase. (n.d.). *Q86YM7 · HOME1_HUMAN*. Retrieved July 24, 2023, from: https://www.uniprot.org/uniprotkb/Q86YM7/entry

77. Gundersen, H. J. G. (1986). Stereology of arbitrary particles. *Journal of Microscopy*, 143(1), 3-45. https://doi.org/10.1111/j.1365-2818.1986.tb02764.x

78. Mouton, P. R. (2012). History of modern stereology. *IBRO History of Neuroscience*. Retrieved July 24, 2023, from https://ibro.org/wp-content/uploads/2018/07/History-of-Modern-Stereology1.pdf and https://srcbiosciences.com/history-of-stereology-by-peter

79. Wicksell, S. D. (1925). The corpuscle problem. A mathematical study of a biometric problem. *Biometrika*, 17(1-2), 84-99. https://doi.org/10.1093/biomet/17.1-2.84

80. Sterio, D. C. (1984). The unbiased estimation of number and sizes of arbitrary particles using the disector. *Journal of Microscopy,* 134(2), 127-136. https://doi.org/10.1111/j.1365-2818.1984.tb02501.x

81. Gundersen, H. J. G., Bagger, P., Bendtsen, T. F., Evans, S. M., Korbo, L., Marcussen, N., Møller, A., Nielsen, K., Nyengaard, J. R., Pakkenberg, B., Sørensen, F. B., Vesterby, A., & West, M. J. (1988). The new stereological tools: disector, fractionator, nucleator and point sampled intercepts and their use in pathological research and diagnosis. *APMIS*, 96(7-12), 857-881. https://doi.org/10.1111/j.1699-0463.1988.tb00954.x

82. MBF Biosciences. Stereological formulas, (n.d.). Williston, Vermont: Author. https://www.mbfbioscience.com/help/pdf/SIformulas.pdf

83. Franklin, K. B., & Paxinos, G. (2012). *The mouse brain in stereotaxic coordinates*. Elsevier.

84. Sun, Y., Ip, P., & Chakrabartty, A. (2017). Simple elimination of background fluorescence in formalin-fixed human brain tissue for immunofluorescence microscopy. *Journal of Visualized Experiments* (127). https://doi.org/10.3791/56188

85. Steyn, F. J., Huang, L., Ngo, S. T., Leong, J. W., Tan, H. Y., Xie, T. Y., Parlow, A. F., Veldhuis, J. D., Waters, M. J., & Chen, C. (2011). Development of a method for the determination of pulsatile growth hormone secretion in mice. *Endocrinology*, 152(8), 3165-3171. https://doi.org/10.1210/en.2011-0253

86. Thermofisher Scientific. Overview of ELISA, (n.d.). Retrieved July 24, 2023, from https://www.thermofisher.com/ca/en/home/life-science/protein-biology/protein-biology-learning-center/protein-biology-resource-library/pierce-protein-methods/overview-elisa.html

87. Aschoff, J. (1981). Freerunning and entrained circadian rhythms. *Biological Rhythms*. In (pp. 81-93). Springer US. https://doi.org/10.1007/978-1-4615-6552-9_6

88. Gray, D. A., & Woulfe, J. (2005). Lipofuscin and aging: a matter of toxic waste. *Science of Aging Knowledge Environment*, 2005(5). https://doi.org/10.1126/sageke.2005.5.re1

89. Terman, A., & Brunk, U. T. (2004). Lipofuscin. *The International Journal of Biochemistry & Cell Biology*, 36(8), 1400-1404. https://doi.org/10.1016/j.biocel.2003.08.009

90. Snyder, A. N., & Crane, J. S. [Last update May 1, 2023]. *Histology, lipofuscin*. In StatPearls [Internet]. Treasure Island (FL): StatPearls Publishing. https://pubmed.ncbi.nlm.nih.gov/30726043/

91. Schnell, S. A., Staines, W. A., & Wessendorf, M. W. (1999). Reduction of lipofuscin-like autofluorescence in fluorescently labeled tissue. *Journal of Histochemistry and Cytochemistry*, 47(6), 719-730. https://doi.org/10.1177/002215549904700601

92. Sun, Y., Yu, H., Zheng, D., Cao, Q., Wang, Y., Harris, D., & Wang, Y. (2011). Sudan black B reduces autofluorescence in murine renal tissue. *Archives of Pathology & Laboratory Medicine*, 135(10), 1335-1342. https://doi.org/10.5858/arpa.2010-0549-oa

93. Biotium (2017). Trueblack® lipofuscin autofluorescence quencher, 20X in DMF. Fremont, California: Author. Retrieved July 24, 2023, https://biotium.com/wp-content/uploads/2017/11/PI-23007.pdf

94. Rosene, D. L., Roy, N. J., & Davis, B. J. (1986). A cryoprotection method that facilitates cutting frozen sections of whole monkey brains for histological and histochemical processing without freezing artifact. *Journal of Histochemistry & Cytochemistry*, 34(10), 1301-1315. https://doi.org/10.1177/34.10.3745909

95. National Library of Medicine (US), National Center for Biotechnology Information, Datasets. *Microtus arvalis, Genome*. Retrieved July 24, 2023, from https://www.ncbi.nlm.nih.gov/data-hub/taxonomy/47230/

96. Andersen, K. (1985). Cavalieri's method of indivisibles. *Archive for History of Exact Sciences*, 31(4), 291-367. https://doi.org/10.1007/bf00348519